

行政院國家科學委員會專題研究計畫 成果報告

量子糾纏態之研究

計畫類別：個別型計畫

計畫編號：NSC94-2112-M-009-024-

執行期間：94年08月01日至95年07月31日

執行單位：國立交通大學電子物理學系(所)

計畫主持人：褚德三

計畫參與人員：陳岳男、林高進、邱裕煌、李哲明、廖英彥、唐英瓚、周瑞雯、
邱奎霖、陳光胤、吳耿榮

報告類型：精簡報告

處理方式：本計畫可公開查詢

中 華 民 國 95 年 9 月 26 日

行政院國家科學委員會補助專題研究計畫 成果報告
 期中進度報告

計畫名稱：量子糾纏態之研究(Studies on the quantum entanglement)

計畫類別： 個別型計畫 整合型計畫

計畫編號：NSC 94-2112-M-009-024-

執行期間：94 年 8 月 1 日至 95 年 7 月 31 日

計畫主持人：褚德三

共同主持人：

計畫參與人員：林高進、廖英彥、簡贖瑞、李哲明、邱奕煌、唐英瓚、
周瑞雯、陳光胤、邱奎霖、吳耿榮

成果報告類型(依經費核定清單規定繳交)： 精簡報告 完整報告

本成果報告包括以下應繳交之附件：

- 赴國外出差或研習心得報告一份
- 赴大陸地區出差或研習心得報告一份
- 出席國際學術會議心得報告及發表之論文各一份
- 國際合作研究計畫國外研究報告書一份

處理方式：除產學合作研究計畫、提升產業技術及人才培育研究計畫、
列管計畫及下列情形者外，得立即公開查詢

涉及專利或其他智慧財產權， 一年 二年後可公開查詢

執行單位：國立交通大學電子物理系

中華民國 95 年 9 月 10 日

中文摘要

在研究量子訊息與量子計算機之傳輸、儲存與讀取過程中，量子訊息之處理是很重要的工作，而處理量子訊息時，例如量子視訊傳輸、量子資據之壓縮及量子密碼之加密解密等，則均有賴於是否能以最大量子糾纏態在傳送者與接受者之間的量子通道中傳送。糾纏態的產生相當多元化，例如在微空腔中的兩個量子點系統，即可因空腔中光子熱庫的引發而產生，另外，如兩個原子系統共同分享了光子熱庫，則這兩個原子也有機會形成糾纏態。此外，由於奈米技術的快速進展，固態物理學家們更可以在 Gate-controlled 且距離甚遠的兩個量子點中，透過 Kondo 效應(RKKY 交互作用)形成遠距離電子自旋的糾纏態。有鑒於糾纏態物理成因的多樣性以及其在量子資訊科學上的應用價值，我們將從不同的物理系統出發，探討糾纏態的形成方式及其可操控性。本計畫將包涵實驗與理論部分共三個子題：

- (1) CdSe/ZnS 量子點的超輻射現象及其在空腔中糾纏態的產生與純化；
- (2) 超快雷射下轉動分子間的糾纏態；
- (3) 量子點在 Kondo 效應極限區域伴隨自旋反轉的傳輸現象。

在第 1 子題中，我們將測量極少數 CdSe/ZnS 量子點的超輻射現象，利用光學攝子及化學合成的 CdSe/ZnS 量子點，使能觀測極少數量子點的超輻射現象，並量量子點中激子衰變之衰變率及頻率遷移。我們也將發展出一套如何在空腔中產生糾纏態與如何將之純化的理論，並配合實驗。

在第 2 子題中，我們將研究超快雷射照射下轉動分子間的糾纏態如何產生的機制，並研究如何使得糾纏態達到最大糾纏。

在第 3 子題中，我們將研究量子點在伴隨有 spin flip 效應發生時的傳輸情形。

並將之延伸到多量子點結構的情形。

本計畫上述三個子題已於 2006 年 7 月 31 日結束，在全一年的計畫中共發表五三篇 PRB 文章，另有多篇在國外知名期刊(JAP, J.of Phys.B, Phys.lett., Solid State Comm., New J. of Physics, Nanotechnology...等)發表(見 2005-2006 著作出版目錄)。另外，預計完成之實驗測量陸續完成，成果亦已發表於國、內外舉辦之國際會議中，目前有數篇理論及實驗文章正投稿或再審查中。

關鍵詞：空腔量子電動力學，超輻射、量子噪訊，量子糾纏、量子隱形傳輸、量子傳輸、光助量子傳輸、自旋電流。

計畫英文摘要

We propose to study three topics that are closely related to the quantum information research and nanostructure physics. It is well known that the generation of pure and maximum entangled states is the most fundamental basis in quantum information researches. In the research of the transport of quantum information, the handling of quantum information is one of the important works. In such work, the maximum entangled state is required to transport between quantum channels. There are many ways to generate the entangled states, e.g. a double-quantum-dot system embedded inside a microcavity can be one of the favorable choices. Besides, a gate-controlled double-quantum-dots can produce remote spin entangled states via Kondo effect (RKKY interaction). To manifest this variety of entanglement generation, we thus propose different topics that can study how to generate and observe the entangled states. Actually, three topics will be simultaneously studied in three years:

(1). The superradiance phenomena of the excitons in CdSe/ZnS quantum dot and the generation and purification mechanisms of entanglement. In this topic, we will develop a simpler technique to form a few CdSe/ZnS quantum system. The quantum dots are fabricated by chemical method in some chemical solution. We proposed to employ the optical tweezers to pick up the quantum dots and locate them on some desired sites so that we may form a very few quantum dot system to observe the superradiance effect. Using this technique one might observe the inter-dot distance dependence of the decay rates and the frequency shift. Besides, a time evolution operation will be constructed and a Zeno-like measurement will be performed to establish a pure and maximum entanglement state in a double quantum-dot-like quantum well system.

(2). The orientation states of two coupled polar molecules controlled by laser pulses will be studied theoretically. The period of a series of periodically applied laser pulse will be applied. Schmidt decomposition will be used to measure the

degree of the entanglement. We will also study how to enhance the entanglement.

(3). The spin flip transport based on the Anderson model in non-equilibrium situation will be studied. The effect of the spin flip on the conductance will be studied. The feasibility of read-out the qubit formed by nuclear spin via the electric measurement of Kondo effect will be also studied.

Our original proposal has been finished. The results have been published. The total publications during 2005-2006 includes 5 papers in Phys. Rev.B, and many articles published in other journals such as : Solid state comm., J. of Applied physics, New Journal of Physics, Phys. Lett. Appl. Surf. Science and J. of Phys.B and J.of phys. D and nanotechnology,.. etc. Some experimental results have been reported in the conferences inside or outside the country and are submitting for publishing or are under reviewing now.

Keyword: Cavity Quantum electrodynamics, superradiance, quantum dot, quantum ring, quantum transport, spin current, spin-orbit interaction, nanomechanical Oscillation, quantum entanglement, teleportation, reservoir induced entanglement, shot noise, Zeno effect.

報告內容(已發表論文目錄)

Publications between 2005 and 2006

- (1). S.R Jian, T.H. Fang and D.S. Chuu, “Nanomechanical Characterizations of InGaN Thin Films”, *Applied Surface Science*. 254(8) 3033-42 (2005)..
- (2). S.R Jian, T.H. Fang and D.S. Chuu, “Mechanisms of p-GaAs(100) surface by atomic force microscope nanooxidation”, accepted by *J. of Physics D (Appl. Physics)*,xxxxxx-xxx (2005)
- (3). S.R Jian, T.H. Fang and D.S. Chuu, ‘Nanoindentation investigation of amorphous hydrogenated carbon thin films deposited by ECR-MPCVD’*Journal Of Non-Crystalline Solids* 333 (3): 291-295 (2004).
- (4). K.C.Lin and D.S. Chuu, “Spin-flip transport through an interacting quantum dot”, *Solid State Commun.* 134 , 831-835 (2005).
- (5). K.C.Lin and D.S. Chuu, ”Anderson model with spin-flip-associated tunneling” *Phys. Rev. B*72, 125314-1-11 (2005).
- (6). C.W. Chiu, Y.H. Chiu, F.L. Shyu, C.P. Chang, D.S. Chuu, M.F. Lin, “Temperature-Dependent Carrier Dynamics in Metallic Carbon Nanotubes” Accepted by *Phys. Lett.* Xxxx-xxx (2005).
- (7).K.P.Chang, S.L.Yang,D.S. Chuu, R.S.Hsiao, J.F.Chen, L.Wei, J.S.Wang and J.Y.Chi “Characterization of self-assembled InAs quantum dots with InAlAs/InGaAs Strain-reduced layers by photoluminescence spectroscopy” *J. of Appl. Phys.* 97,083511-1-083511-4 (2005).
- (8). Y.N. Chen, C.M. Li, D.S. Chuu , T. Brandes, ” Proposal for teleportation of charge qubits via superradiance”, Accepted by *New J. of Physics*,xxx xxx-xx (2005).
- (9).Jin-Yuan Hsieh, Che-Ming Li, Der-San Chuu, “Hamiltonian and measuring time for analog quantum search”, Accepted by *J. OF Phys. Soc. of Japan* 74 , 2945-48 (2005).
- (10). Y.N. Chen, D.S. Chuu, and T. Brandes, “Current noise of a quantum dot p-i-n junction in a photonic crystal”, *Phys. Rev.B* 72, 153312-1-4 (2005).
- (11). Y.Y. Liao, Y.N. Chen, C.M. Li and D.S. Chuu , ” Entangled rotational states between two coupled molecules” , Accepted by *Journal of Physics B: Atomic, Molecular & Optical Physics*, xxx, xxx-xx (2005).

- (12). Y.N. Chen, D.S. Chuu, and S.J. Cheng, “Shot noise of a quantum ring exciton in a planar microcavity”, Phys. Rev.B 72, 233301-1-4 (2005).
- (13). C.W. Chiu, F.L. Shyu, C.P. Chang, D.S. Chuu, M.F. Lin, “Coulomb scattering rates of excited carriers in moderate-gap carbon nanotubes”, Phys. Rev. B XX, xxxxx-xx (2006)
- (14). Jin-Yuan Hsieh, Che-Ming Li and Der-San Chuu. “Analytical technique for simplification of the encoder–decoder circuit for a perfect 5-qubit error correction”, New Journal of Physics 8 (2006)
- (15). Y. Y. Liao, Y. N. Chen, W. C. Chou, and D. S. Chuu, “Orientation of adsorbed dipolar molecules: A conical well model”, Phys. Rev. B 73, 115421-26 (2006)
- (16). J. T. Ku, M. C. Kuo, J. L. Shen, K. C. Chiu, T. H. Yang, G. L. Luo, C. Y. Chang, Y. C. Lin, C. P. Fu, D. S. Chuu, C. H. Chia, and W. C. Chou, “Optical characterization of ZnSe epilayers and ZnCdSe/ZnSe quantum wells grown on Ge/Ge_{0.95}Si_{0.05}/Ge_{0.9}Si_{0.1}/Si virtual substrates”, J. Appl. Phys. 99, 063506-12 (2006) ,
- (17). Y. Y. Liao, Y. N. Chen, D. S. Chuu, and T. Brandes, “Spin relaxation in a GaAs quantum dot embedded inside a suspended phonon cavity”, Phys. Rev. B 73, 085310 (2006)
- (18). Sheng-Rui Jian^a, Te-Hua Fang^b and Der-San Chuu^a, “Nanomechanical characterizations of InGaN thin films “ APPL. SURF. SCIENCE 252 (8): 3033-3042 (2006).
- (19). Y.J. Lai^a, Y.C. Lin^a, C.P. Fu^a, C.S. Yang^a, C.H. Chia^a, D.S. Chuu^a, W.K. Chen^a, M.C. Lee, W.C. Chou^a, M.C. Kuo and J.S. Wang , “Growth mode transfer of self-assembled CdSe quantum dots grown by molecular beam epitaxy “, J. of Crystal Growth 286 (2): 338-344 (2006).
- (20). W.-P.Huang¹, S.R. Jian^{2*}, C.-M.Lin³, J.Y. Hsieh⁴, D.S. Chuu² and H.H.Cheng¹
 “Localized electrochemical oxidation of *p*-GaAs(100) using an atomic force microscopy with carbon nanotube probe”, Nanotechnology 17, 3838-43 (2006).

以下列出三篇論文全文。

Anderson model with spin-flip-associated tunneling

Kao-Chin Lin and Der-San Chuu

Department of Electrophysics, National Chiao-Tung University, Hsinchu 300, Taiwan

(Received 3 March 2005; revised manuscript received 11 July 2005; published 9 September 2005)

The spin-flip-associated transport through a quantum dot based on the Anderson model in equilibrium and nonequilibrium situations is studied. It is found that electrons are scattered due to the spin-flip effect via the normal and the Kondo channels. Our results show that the conductance is suppressed due to the spin-flip effect, and the suppression due to the spin-flip scattering via the Kondo channel is stronger for temperatures below the Kondo temperature.

DOI: [10.1103/PhysRevB.72.125314](https://doi.org/10.1103/PhysRevB.72.125314)

PACS number(s): 73.23.-b, 73.63.-b, 75.25.+z

I. INTRODUCTION

Recently, much theoretical and experimental research related to electron spin has been done. Owing to the progress in nanofabrication and microelectronic techniques, devices based on the electron spin, such as spin memory,¹ spin transistor,² and electron-spin-based quantum computers,^{3,4} may be realized very soon. These devices are related to the spin-polarization orientation or spin-flip effect. Usually, the spin-flip effect occurs in scattering processes. The scattering processes may be caused by magnetic impurities, magnons, or domain walls at the interface or electrode,⁵ or may be due to interactions with phonons⁶ or the photon field.⁷ In addition to scattering processes, spin flip may occur when the electron is transported between different spin-state regions. One of the instances is that the electron is transported between the Rashba quantum dot and the ferromagnetic lead. The Rashba effect can be observed in InAs semiconductors. The eigenstate of the Rashba Hamiltonian is a superposition of the spin states $|\uparrow\rangle$ and $|\downarrow\rangle$, i.e., $|\pm\rangle = (1/\sqrt{2})(e^{i\theta/2}|\uparrow\rangle \pm e^{-i\theta/2}|\downarrow\rangle)$.⁴ It is known that the off-diagonal terms of the tunneling amplitude matrix and coupling constant are nonzero and spin-flip-associated tunneling appears in the system.⁸ A sketch of the spin-flip-associated tunneling through a quantum system is shown in Fig. 1.

The spin-flip-associated tunneling effect might cause some special behaviors in the electric properties of the material. The intradot spin-flip effect was found to shift the resonant energy ϵ_0 of the quantum dot to $\epsilon_0 \pm R$, where R is the spin-flip scattering amplitude.⁸ Sergueev *et al.*⁹ studied the spin-flip-associated tunneling through a quantum dot and described the spin-valve effect. The spin-valve effect caused by the transport between different spin states shows that the resistance depends on the direction (parallel or antiparallel) of the magnetization of two ferromagnetic metals.⁹⁻¹² Zhu and Balatsky studied the spin-flip-associated tunneling through a local nuclear spin precessing in a magnetic field to simulate the conductance oscillation observed in STM experiments.¹³ They included the off-diagonal process and concluded that the conductance of the system can be obviously modified. Guinea pointed out that elastic spin-flip effects give rise to a temperature-independent reduction of the magnetoresistance while inelastic spin-flip processes give rise to temperature-dependent non-Ohmic effects and varia-

tion of the conductance.⁵ As mentioned above, the spin-flip effect is important in the study of spin electronic devices and thus is worth exploring.

In spin-based devices such as a spin-based quantum computer, which may be operated at low temperature, the correlation between the electron in the quantum dot and the conduction electrons in the reservoir is important because the correlation will cause a peak of the density of states in the vicinity of the Fermi level for temperature $T \leq T_K$, where T_K is the Kondo temperature. The Anderson impurity model, which describes the correlation due to on-site Coulomb interaction and the direct tunneling between the conduction band and the local spin state in the magnetic impurity, is also employed to describe the quantum dot (QD) system.¹⁴ The correlation interaction causes a sharp peak in the vicinity of the Fermi level for temperatures below T_K . The electron in the impurity may tunnel out of the impurity site to occupy a “virtual state,” and then be replaced by an electron from the metal.^{15,16} This process can effectively “flip” the spin of the impurity. Schrieffer and Wolff have shown that, in the limit of strong on-site Coulomb interaction, the Anderson impurity model is equivalent to the s - d model when the impurity level ϵ_0 is well below the Fermi level and the Kondo effect is obtained in this limit.¹⁷ In the original Anderson impurity model, the electron spin does not flip during the process of tunneling between the impurity and the electron reservoir. In this work, we consider that the electron spin flips during the tunneling process, i.e., the spin-flip-associated coupling constant $\Gamma_{\alpha}^{\bar{\sigma}\sigma} = 2\pi \sum_{k,s,\alpha \in L,R} V_{k,\alpha,s}^* V_{k,\alpha,s} \bar{\sigma} \delta(\omega - \epsilon_{k\alpha s})$ where $\sigma(s)$ is the spin state of the electron in the QD (lead) and $\bar{\sigma} \neq \sigma$ is included in our study. The effects on the density of states and the conductance of the quantum dot system versus the strength of the spin-flip coupling will be discussed. Compared to the original Anderson model, the spin-flip-associated tunneling effect is expected to contribute additional self-energy which may modify the local density of state (LDOS), or the diagonal part of the spectral function $-2 \text{Im} G_{\sigma\sigma}^r$. The conductance depends strongly on the profile of the diagonal part of the spectral function $-2 \text{Im} G_{\sigma\sigma}^r$ and the off-diagonal part of the spectral function $-2 \text{Im} G_{\bar{\sigma}\sigma}^r$, which may change sign in the vicinity of the peak position of the LDOS. Therefore, the off-diagonal spectral function is expected to modify the conductance. In other words, the conductance may be modified by spin-flip-associated tunneling.

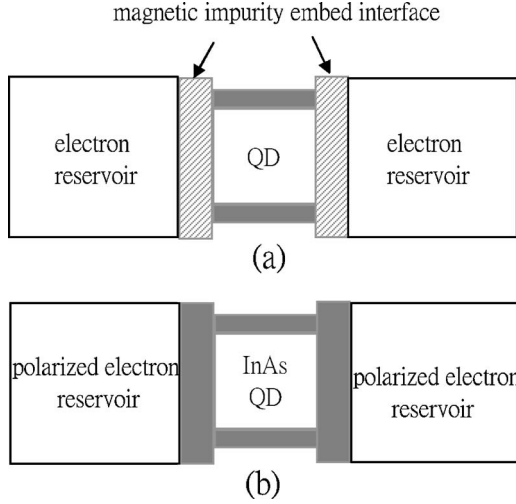


FIG. 1. The schematic plot of the system considered in this work. The spin-flip-associated tunneling is (a) originated by the impurity scattering and (b) due to the tunneling between the different spin states.

Instead of studying the mechanism of the spin-flip effect, we will study the spin-flip effect in a phenomenological way. The tunneling coupling constant will be assumed the same as that proposed in Ref. 13.

II. MODEL AND FORMALISM

The Hamiltonian of the system considered in this work can be written as

$$H_d = \sum_{\sigma} \epsilon_{\sigma} d_{\sigma}^{\dagger} d_{\sigma} + U n_{\sigma} n_{\bar{\sigma}},$$

where the self-energy $\Sigma_{\sigma\sigma}$ is caused by tunneling without an associated spin flip and the self-energy $\Sigma_{\bar{\sigma}\sigma}$ is caused by spin-flip-associated tunneling. $\Sigma_{\bar{\sigma}\sigma}$ flips spin σ to spin $\bar{\sigma}$ during the electron transport between the lead and the dot. $G_{\sigma\sigma}^0$ is the free-particle Green's function and $\tilde{G}_{\sigma\sigma}^0 = (\omega - \epsilon_{\sigma} - \Sigma_{\sigma\sigma})^{-1}$ is the Green's function of the electron in the QD with the spin state σ perturbed by the tunneling effect. The detailed derivation of Eq. (2) is shown in Appendix A.

If the intradot Coulomb interaction is included, the Kondo effect occurs when $T \leq T_K$. There are many approaches to solve the problem, such as the noncrossing-approximation

$$H_C = \sum_{\substack{k_{\alpha s} \\ \alpha \in L, R}} \epsilon_{k_{\alpha s}} c_{k_{\alpha s}}^{\dagger} c_{k_{\alpha s}},$$

$$H_T = \sum_{k_{\alpha s}, \sigma} V_{k_{\alpha s}, \sigma}^* d_{\sigma}^{\dagger} c_{k_{\alpha s}} + V_{k_{\alpha s}, \sigma} c_{k_{\alpha s}}^{\dagger} d_{\sigma} \quad (1)$$

where $d_{\sigma}^{\dagger} (d_{\sigma})$ is the creation (annihilation) operator of the electron with spin state σ in the dot, and $c_{k_{\alpha s}}^{\dagger} (c_{k_{\alpha s}})$ is the creation (annihilation) operator of an electron with momentum k and spin state s in the α lead (where $\alpha \in L, R$). Note that the spin states s and σ are not necessary in the same eigenstate, for example, the spin state σ in the QD may be the eigenstate of the Rashba state and the spin state s in the lead may be the pure spin-up or spin-down state. The energy $\epsilon_{k_{\alpha s}}$ is the single-particle energy of the conduction electron in the α lead. U is the intradot Coulomb interaction. The electron tunneling between the lead and dot can be described by the tunneling matrix $V_{k_{\alpha s}, \sigma}$. As shown in Ref. 13, the coupling constant between the QD and the lead can be expressed by $\Gamma_{\alpha}^{\bar{\sigma}\sigma} = 2\pi \sum_{k, s, \alpha \in L, R} V_{k_{\alpha s}, \bar{\sigma}}^* V_{k_{\alpha s}, \sigma} \delta(\omega - \epsilon_{k_{\alpha s}})$. The spin-flip coupling constant is set to be symmetric for the state σ ($\bar{\sigma}$) flipped into the state $\bar{\sigma}$ (σ), i.e., $\Gamma_{\alpha}^{\bar{\sigma}\sigma} = \Gamma_{\alpha}^{\sigma\bar{\sigma}} = \Gamma_{\alpha}^s$. And the normal coupling constant $\Gamma_{\alpha}^{\sigma\sigma} = 2\pi \sum_{k, s, \alpha \in L, R} V_{k_{\alpha s}, \sigma}^* V_{k_{\alpha s}, \sigma} \delta(\omega - \epsilon_{k_{\alpha s}})$ is assumed to be spin independent, i.e., $\Gamma_{\alpha}^{\sigma\sigma} = \Gamma_{\alpha}^{\bar{\sigma}\bar{\sigma}} = \Gamma_{\alpha}^n$. In this paper, we use the notation $\bar{\sigma}$ to stand for the spin being not equal to σ while σ' is equal or not equal to σ .

The Green's function \mathbf{G} corresponding to the spin-flip-associated tunneling effect of the noninteracting system can be written as

$$\begin{aligned} \begin{bmatrix} G_{\sigma\sigma} & G_{\sigma\bar{\sigma}} \\ G_{\bar{\sigma}\sigma} & G_{\bar{\sigma}\bar{\sigma}} \end{bmatrix} &= \begin{bmatrix} G_{\sigma\sigma}^0 & 0 \\ 0 & G_{\bar{\sigma}\bar{\sigma}}^0 \end{bmatrix} + \begin{bmatrix} G_{\sigma\sigma}^0 & 0 \\ 0 & G_{\bar{\sigma}\bar{\sigma}}^0 \end{bmatrix} \begin{bmatrix} \Sigma_{\sigma\sigma} & \Sigma_{\sigma\bar{\sigma}} \\ \Sigma_{\bar{\sigma}\sigma} & \Sigma_{\bar{\sigma}\bar{\sigma}} \end{bmatrix} \begin{bmatrix} G_{\sigma\sigma} & G_{\sigma\bar{\sigma}} \\ G_{\bar{\sigma}\sigma} & G_{\bar{\sigma}\bar{\sigma}} \end{bmatrix} \\ &= \begin{bmatrix} [(G_{\sigma\sigma}^0)^{-1} - \Sigma_{\sigma\sigma} - \Sigma_{\sigma\bar{\sigma}} \tilde{G}_{\bar{\sigma}\bar{\sigma}}^0 \Sigma_{\bar{\sigma}\sigma}]^{-1} & \tilde{G}_{\sigma\sigma}^0 \Sigma_{\sigma\bar{\sigma}} G_{\bar{\sigma}\bar{\sigma}} \\ \tilde{G}_{\bar{\sigma}\bar{\sigma}}^0 \Sigma_{\bar{\sigma}\sigma} G_{\sigma\sigma} & [(G_{\bar{\sigma}\bar{\sigma}}^0)^{-1} - \Sigma_{\bar{\sigma}\bar{\sigma}} - \Sigma_{\bar{\sigma}\sigma} \tilde{G}_{\sigma\sigma}^0 \Sigma_{\sigma\bar{\sigma}}]^{-1} \end{bmatrix} \quad (2) \end{aligned}$$

approach,^{18,11} the equation of motion (EOM) method,^{19–22,10} or the renormalization group method.^{12,20,23} The equation of motion method will be used to solve the Green's function of the interaction system in this work. In the processes of the EOM, the two-particle correlation function (or Green's function) arises from the two-particle on-site Coulomb interaction and needs to be decoupled. The accuracy of the EOM method depends on the decoupling scheme. One of the compact ways to decouple the two-particle correlation function to the single-particle correlation function is the decoupling scheme introduced by Lacroix for high temperature

(i.e., $T \geq T_K$). The high-temperature Lacroix decoupling approximation at low temperatures ($T < T_K$) gives only a qualitative solution and is quantitatively correct at high temperatures ($T \geq T_K$).^{9,20} The EOM and Lacroix's high-temperature decoupling scheme are popularly adopted by many authors. In this work, we will use the high-temperature Lacroix de-

coupling approximation to decouple the two-particle Green's function.

Consider the spin-flip-associated tunneling effect where the intradot particle-particle interaction is assumed to be the Coulomb interaction. By using the method of the equation of motion in the Green's function \mathbf{G} , one obtains

$$\begin{bmatrix} (\omega - \epsilon_\sigma)G_{\sigma\sigma} & (\omega - \epsilon_\sigma)G_{\sigma\bar{\sigma}} \\ (\omega - \epsilon_{\bar{\sigma}})G_{\bar{\sigma}\sigma} & (\omega - \epsilon_{\bar{\sigma}})G_{\bar{\sigma}\bar{\sigma}} \end{bmatrix} = \begin{bmatrix} 1 & 0 \\ 0 & 1 \end{bmatrix} + \begin{bmatrix} \sum T_{\sigma\sigma}^n & \sum T_{\sigma\bar{\sigma}}^n \\ \sum T_{\bar{\sigma}\sigma}^n & \sum T_{\bar{\sigma}\bar{\sigma}}^n \end{bmatrix} \begin{bmatrix} G_{\sigma\sigma} & G_{\sigma\bar{\sigma}} \\ G_{\bar{\sigma}\sigma} & G_{\bar{\sigma}\bar{\sigma}} \end{bmatrix} + U \begin{bmatrix} G_{\sigma\sigma}^{(2)} & G_{\sigma\bar{\sigma}}^{(2)} \\ G_{\bar{\sigma}\sigma}^{(2)} & G_{\bar{\sigma}\bar{\sigma}}^{(2)} \end{bmatrix} \quad (3)$$

where $G_{\sigma\sigma'} \equiv (-i)\langle T\{d_\sigma, d_{\sigma'}^\dagger\} \rangle$ and $G_{\sigma\bar{\sigma}'}^{(2)} \equiv (-i)\langle T\{d_\sigma n_{\bar{\sigma}}, d_{\sigma'}^\dagger\} \rangle$. The Green's function $G_{\sigma\sigma'}^{(2)}$ is the two-particle Green's function corresponding to particle-particle interaction (Coulomb interaction) and is related to the Kondo effect. Using the EOM in $\mathbf{G}^{(2)}$, we obtain

$$\begin{aligned} \begin{bmatrix} (\omega - \epsilon_\sigma - U)G_{\sigma\sigma}^{(2)} & (\omega - \epsilon_\sigma - U)G_{\sigma\bar{\sigma}}^{(2)} \\ (\omega - \epsilon_{\bar{\sigma}} - U)G_{\bar{\sigma}\sigma}^{(2)} & (\omega - \epsilon_{\bar{\sigma}} - U)G_{\bar{\sigma}\bar{\sigma}}^{(2)} \end{bmatrix} &= \begin{bmatrix} \langle n_{\bar{\sigma}} \rangle & 0 \\ 0 & \langle n_\sigma \rangle \end{bmatrix} + \sum_{k\alpha^s} \begin{bmatrix} V_{k\alpha^s, \sigma}^* (-i)\langle T\{c_{k\alpha^s}^\dagger d_{\bar{\sigma}}^\dagger d_\sigma, d_{\sigma'}^\dagger\} \rangle & V_{k\alpha^s, \sigma}^* (-i)\langle T\{c_{k\alpha^s}^\dagger d_{\bar{\sigma}}^\dagger d_{\bar{\sigma}}, d_{\sigma'}^\dagger\} \rangle \\ V_{k\alpha^s, \bar{\sigma}}^* (-i)\langle T\{c_{k\alpha^s}^\dagger d_\sigma^\dagger d_{\bar{\sigma}}, d_{\sigma'}^\dagger\} \rangle & V_{k\alpha^s, \bar{\sigma}}^* (-i)\langle T\{c_{k\alpha^s}^\dagger d_\sigma^\dagger d_\sigma, d_{\sigma'}^\dagger\} \rangle \end{bmatrix} \\ &+ \sum_{k\alpha^s} \begin{bmatrix} V_{k\alpha^s, \bar{\sigma}} (-i)\langle T\{c_{k\alpha^s}^\dagger d_\sigma d_{\bar{\sigma}}, d_{\sigma'}^\dagger\} \rangle & V_{k\alpha^s, \bar{\sigma}} (-i)\langle T\{c_{k\alpha^s}^\dagger d_\sigma d_\sigma, d_{\sigma'}^\dagger\} \rangle \\ V_{k\alpha^s, \sigma} (-i)\langle T\{c_{k\alpha^s}^\dagger d_{\bar{\sigma}} d_\sigma, d_{\sigma'}^\dagger\} \rangle & V_{k\alpha^s, \sigma} (-i)\langle T\{c_{k\alpha^s}^\dagger d_{\bar{\sigma}} d_{\bar{\sigma}}, d_{\sigma'}^\dagger\} \rangle \end{bmatrix} \\ &- \sum_{k\alpha^s} \begin{bmatrix} V_{k\alpha^s, \bar{\sigma}}^* (-i)\langle T\{c_{k\alpha^s}^\dagger d_\sigma d_{\bar{\sigma}}, d_{\sigma'}^\dagger\} \rangle & V_{k\alpha^s, \bar{\sigma}}^* (-i)\langle T\{c_{k\alpha^s}^\dagger d_\sigma d_\sigma, d_{\sigma'}^\dagger\} \rangle \\ V_{k\alpha^s, \sigma}^* (-i)\langle T\{c_{k\alpha^s}^\dagger d_{\bar{\sigma}} d_\sigma, d_{\sigma'}^\dagger\} \rangle & V_{k\alpha^s, \sigma}^* (-i)\langle T\{c_{k\alpha^s}^\dagger d_{\bar{\sigma}} d_{\bar{\sigma}}, d_{\sigma'}^\dagger\} \rangle \end{bmatrix}. \end{aligned} \quad (4)$$

In general there are four one-particle Green's functions ($G_{\sigma\sigma}$, $G_{\sigma\bar{\sigma}}$, $G_{\bar{\sigma}\sigma}$ and $G_{\bar{\sigma}\bar{\sigma}}$) and four two-particle Green's functions ($G_{\sigma\sigma}^{(2)}$, $G_{\sigma\bar{\sigma}}^{(2)}$, $G_{\bar{\sigma}\sigma}^{(2)}$ and $G_{\bar{\sigma}\bar{\sigma}}^{(2)}$) in our system. In contrast with Eq. (3), the equation of the Green's function $\mathbf{G}^{(2)}$ can be assumed as

$$\begin{aligned} \begin{bmatrix} (\omega - \epsilon_\sigma - U)G_{\sigma\sigma}^{(2)} & (\omega - \epsilon_\sigma - U)G_{\sigma\bar{\sigma}}^{(2)} \\ (\omega - \epsilon_{\bar{\sigma}} - U)G_{\bar{\sigma}\sigma}^{(2)} & (\omega - \epsilon_{\bar{\sigma}} - U)G_{\bar{\sigma}\bar{\sigma}}^{(2)} \end{bmatrix} &= \begin{bmatrix} \langle n_{\bar{\sigma}} \rangle & 0 \\ 0 & \langle n_\sigma \rangle \end{bmatrix} + \begin{bmatrix} X_{\sigma\sigma}^{(2)} & X_{\sigma\bar{\sigma}}^{(2)} \\ X_{\bar{\sigma}\sigma}^{(2)} & X_{\bar{\sigma}\bar{\sigma}}^{(2)} \end{bmatrix} \begin{bmatrix} G_{\sigma\sigma} & G_{\sigma\bar{\sigma}} \\ G_{\bar{\sigma}\sigma} & G_{\bar{\sigma}\bar{\sigma}} \end{bmatrix} \\ &+ \begin{bmatrix} Y_{\sigma\sigma}^{(2)} & Y_{\sigma\bar{\sigma}}^{(2)} \\ Y_{\bar{\sigma}\sigma}^{(2)} & Y_{\bar{\sigma}\bar{\sigma}}^{(2)} \end{bmatrix} \begin{bmatrix} G_{\sigma\sigma}^{(2)} & G_{\sigma\bar{\sigma}}^{(2)} \\ G_{\bar{\sigma}\sigma}^{(2)} & G_{\bar{\sigma}\bar{\sigma}}^{(2)} \end{bmatrix}. \end{aligned} \quad (5)$$

In order to simplify the problem, we consider the infinite- U limit. Under the infinite- U limit, the off-diagonal term of $\mathbf{Y}^{(2)}$ can be ignored (the detailed derivation will be given in Appendix B). Equation (5) can be rewritten as

$$\begin{aligned} \begin{bmatrix} G_{\sigma\sigma}^{(2)} & G_{\sigma\bar{\sigma}}^{(2)} \\ G_{\bar{\sigma}\sigma}^{(2)} & G_{\bar{\sigma}\bar{\sigma}}^{(2)} \end{bmatrix} &= \begin{bmatrix} g_{\sigma\sigma}^{0(2)} \langle n_{\bar{\sigma}} \rangle & 0 \\ 0 & g_{\sigma\bar{\sigma}}^{0(2)} \langle n_\sigma \rangle \end{bmatrix} \\ &+ \begin{bmatrix} g_{\sigma\sigma}^{0(2)} (X_{\sigma\sigma}^{(2)} G_{\sigma\sigma} + X_{\sigma\bar{\sigma}}^{(2)} G_{\bar{\sigma}\sigma}) & g_{\sigma\sigma}^{0(2)} (X_{\sigma\bar{\sigma}}^{(2)} G_{\bar{\sigma}\bar{\sigma}} + X_{\sigma\sigma}^{(2)} G_{\sigma\bar{\sigma}}) \\ g_{\sigma\bar{\sigma}}^{0(2)} (X_{\bar{\sigma}\sigma}^{(2)} G_{\sigma\sigma} + X_{\bar{\sigma}\bar{\sigma}}^{(2)} G_{\bar{\sigma}\sigma}) & g_{\sigma\bar{\sigma}}^{0(2)} (X_{\bar{\sigma}\bar{\sigma}}^{(2)} G_{\bar{\sigma}\bar{\sigma}} + X_{\bar{\sigma}\sigma}^{(2)} G_{\bar{\sigma}\sigma}) \end{bmatrix} \end{aligned}$$

where $g_{\sigma\sigma}^{0(2)} \equiv (\omega - \epsilon_\sigma - Y_{\sigma\sigma} - U)^{-1}$ and $g_{\sigma\bar{\sigma}}^{0(2)} \equiv (\omega - \epsilon_{\bar{\sigma}} - Y_{\bar{\sigma}\bar{\sigma}} - U)^{-1}$. Substituting $\mathbf{G}^{(2)}$ into \mathbf{G} , one obtains

$$\begin{aligned} \begin{bmatrix} (\omega - \epsilon_\sigma)G_{\sigma\sigma} & (\omega - \epsilon_\sigma)G_{\sigma\bar{\sigma}} \\ (\omega - \epsilon_{\bar{\sigma}})G_{\bar{\sigma}\sigma} & (\omega - \epsilon_{\bar{\sigma}})G_{\bar{\sigma}\bar{\sigma}} \end{bmatrix} &= \begin{bmatrix} 1 + Ug_{\sigma\sigma}^{0(2)} \langle n_{\bar{\sigma}} \rangle & 0 \\ 0 & 1 + Ug_{\sigma\bar{\sigma}}^{0(2)} \langle n_\sigma \rangle \end{bmatrix} + \begin{bmatrix} \sum T_{\sigma\sigma}^T + Ug_{\sigma\sigma}^{0(2)} X_{\sigma\sigma}^{(2)} & \sum T_{\sigma\bar{\sigma}}^T + Ug_{\sigma\sigma}^{0(2)} X_{\sigma\bar{\sigma}}^{(2)} \\ \sum T_{\bar{\sigma}\sigma}^T + Ug_{\sigma\bar{\sigma}}^{0(2)} X_{\bar{\sigma}\sigma}^{(2)} & \sum T_{\bar{\sigma}\bar{\sigma}}^T + Ug_{\sigma\bar{\sigma}}^{0(2)} X_{\bar{\sigma}\bar{\sigma}}^{(2)} \end{bmatrix} \begin{bmatrix} G_{\sigma\sigma} & G_{\sigma\bar{\sigma}} \\ G_{\bar{\sigma}\sigma} & G_{\bar{\sigma}\bar{\sigma}} \end{bmatrix} \\ &\equiv \begin{bmatrix} 1 + Ug_{\sigma\sigma}^{0(2)} \langle n_{\bar{\sigma}} \rangle & 0 \\ 0 & 1 + Ug_{\sigma\bar{\sigma}}^{0(2)} \langle n_\sigma \rangle \end{bmatrix} + \begin{bmatrix} \sum^{tot} T_{\sigma\sigma} & \sum^{tot} T_{\sigma\bar{\sigma}} \\ \sum^{tot} T_{\bar{\sigma}\sigma} & \sum^{tot} T_{\bar{\sigma}\bar{\sigma}} \end{bmatrix} \begin{bmatrix} G_{\sigma\sigma} & G_{\sigma\bar{\sigma}} \\ G_{\bar{\sigma}\sigma} & G_{\bar{\sigma}\bar{\sigma}} \end{bmatrix}. \end{aligned}$$

Under the infinite- U limit, $Ug_{\sigma\sigma}^{0(2)} \sim -1$ and $\sum^{tot} T = \sum^T - \mathbf{X}^{(2)}$. Comparing to Eq. (2) (after some algebra), one obtains

$$\begin{bmatrix} G_{\sigma\sigma} & G_{\sigma\bar{\sigma}} \\ G_{\bar{\sigma}\sigma} & G_{\bar{\sigma}\bar{\sigma}} \end{bmatrix} = \begin{bmatrix} (1 - \langle n_{\bar{\sigma}} \rangle) [(\tilde{G}_{\sigma\sigma}^0)^{-1} - \sum_{\sigma\bar{\sigma}}^{\text{tot}} \tilde{G}_{\sigma\bar{\sigma}}^0 \sum_{\bar{\sigma}\sigma}^{\text{tot}}]^{-1} & \tilde{G}_{\sigma\sigma}^0 \sum_{\sigma\bar{\sigma}}^{\text{tot}} G_{\bar{\sigma}\bar{\sigma}} \\ \tilde{G}_{\bar{\sigma}\bar{\sigma}}^0 \sum_{\bar{\sigma}\sigma}^{\text{tot}} G_{\sigma\sigma} & (1 - \langle n_{\sigma'} \rangle) [(\tilde{G}_{\bar{\sigma}\bar{\sigma}}^0)^{-1} - \sum_{\bar{\sigma}\sigma}^{\text{tot}} \tilde{G}_{\bar{\sigma}\sigma}^0 \sum_{\sigma\sigma'}^{\text{tot}}]^{-1} \end{bmatrix}. \quad (6)$$

In Eq. (6) $\tilde{G}_{\sigma\sigma}^0 \equiv (\omega - \epsilon_{\sigma} - \sum_{\sigma\sigma'}^{\text{tot}})^{-1}$ and $\tilde{G}_{\bar{\sigma}\bar{\sigma}}^0 \equiv (\omega - \epsilon_{\bar{\sigma}} - \sum_{\bar{\sigma}\bar{\sigma}'}^{\text{tot}})^{-1}$. Comparing $\tilde{G}_{\sigma\sigma}^0$ with Eq. (3) in Ref. 20,

$$G_{\sigma\sigma} = \frac{1 - \langle n_{\bar{\sigma}} \rangle}{\omega - \epsilon_{\sigma} - \sum_{0\sigma} - \sum_{1\sigma}}, \quad (7)$$

which is the Green's function corresponding to the original Anderson model. Now set $\mathbf{X}^{(2)} \equiv -\sum_{1\sigma} \tilde{\mathbf{G}}^0$ is the same as the Green's function corresponding to the original Anderson Hamiltonian except for the factor $(1 - \langle n_{\bar{\sigma}} \rangle)$. $\tilde{\mathbf{G}}^0$ can be regarded as the Green's function of the quasiparticle of the Anderson Hamiltonian without the spin-flip effect. Now, the remaining problem is to obtain $\mathbf{X}^{(2)}$ and $\mathbf{Y}^{(2)}$. The detailed derivation and results are presented in Appendix B.

The form of our result [Eq. (6)] is the same as Eq. (2) except for the self-energy $\mathbf{X}^{(2)}$ which is related to the Kondo effect. The physical picture of the Green's function [Eq. (6)] can be interpreted as follows. $\tilde{\mathbf{G}}^0$ is the Green's function corresponding to the Anderson Hamiltonian without the spin-flip effect, i.e., it is the form of the Green's function as shown in Eq. (3) of Ref. 20. $G_{\sigma\sigma}$ in Eq. (6), for example, represents the corresponding σ -state quasiparticle of the Anderson Hamiltonian, which is scattered between the σ and $\bar{\sigma}$ states and causes the self-energy $\sum_{\sigma\bar{\sigma}}^{\text{tot}} \tilde{G}_{\sigma\bar{\sigma}}^0 \sum_{\bar{\sigma}\sigma}^{\text{tot}} \sum_{\bar{\sigma}\sigma}^{\text{tot}}$ contains two terms: the self-energy $\sum_{\bar{\sigma}\sigma}^T$ corresponding to the scattering via the normal channel and the self-energy $X_{\bar{\sigma}\sigma}^{(2)}$ corresponding to the scattering via the Kondo channel. The normal-channel scattering is energy and temperature independent. Since the Kondo effect is strongly dependent on the temperature and causes a Kondo resonant peak in the vicinity of the Fermi level of the lead, the Kondo-channel scattering is strongly dependent on the temperature and dominates the scattering with energy in the vicinity of the Fermi energy of the lead.

Since the transport problem in a quantum dot system may be a nonequilibrium problem, we will employ the nonequilibrium Green's function method and the transport equation developed by Wingreen *et al.* to calculate the particle number and conductance.²⁵ To evaluate Eq. (6) numerically, one must determine the particle number $\langle n_{\sigma} \rangle$ and the expectation value $\langle d_{\sigma}^{\dagger} d_{\bar{\sigma}} \rangle$ by a self-consistent method. In order to calculate the expectation values $\langle n_{\sigma} \rangle$ and $\langle d_{\sigma}^{\dagger} d_{\bar{\sigma}} \rangle$, the corresponding lesser Green's functions $G_{\sigma\sigma}^{<}$ and $G_{\bar{\sigma}\sigma}^{<}$ must be solved first, i.e., $\langle n_{\sigma} \rangle = -i \int (d\epsilon/2\pi) G_{\sigma\sigma}^{<}$ and $\langle d_{\sigma}^{\dagger} d_{\bar{\sigma}} \rangle = -i \int (d\epsilon/2\pi) G_{\bar{\sigma}\sigma}^{<}$. In this work, we use the method proposed by Sun and Guo which is able to solve the lesser Green's function, of the interacting system exactly for the steady-state problem.²⁴ The detailed derivation processes are shown in Appendix C.

III. RESULTS AND DISCUSSION

In the following discussion, all energy scales are normalized to the normal-tunneling coupling constant $\Gamma_{\alpha}^n = 1$. The resonant energy of the quantum dot is set as $\epsilon_0 = -5$. The Fermi level of the lead E_F is set to be zero for the equilibrium situation. The temperature is normalized to the Kondo temperature T_K , which is calculated by the exact expression obtained by Haldane, $T_K \approx (D\Gamma)^{1/2} \exp[\pi(\epsilon_0 - E_F)/(2\Gamma)] \approx 0.004$,²⁶ with the half-width $D = 100$ and $\Gamma = \Gamma_L^n + \Gamma_R^n$.

Since the high temperature Lacroix decoupling approximation at low temperatures ($T < T_K$) gives only a qualitative solution and is quantitatively correct at high temperatures ($T > T_K$), we consider the situation with the temperature near the Kondo temperature, i.e., $T = 10T_K$, $1T_K$, and $0.1T_K$, and the normal limit $T = 100T_K$, for which the Kondo effect can be ignored for comparison.²⁷ The spectral function $A_{\sigma'\sigma}(\omega) = -2 \text{Im} G_{\sigma'\sigma}^r$ (or local density of states when $\sigma' = \sigma$) in the equilibrium situation is calculated in terms of the strength of spin-flip-associated tunneling, which is described by the spin-flip coupling constant Γ^s . As in the previous discussion, the quasiparticle of the Anderson Hamiltonian is scattered by the normal and the Kondo channels. The self-energy Σ^T due to normal-channel scattering is independent of the energy and the temperature; thus the electron can be scattered by the normal channel at arbitrary energy and temperature. In contrast to the normal channel, the Kondo-effect channel is energy dependent and the strength increases logarithmically in the vicinity of the Fermi level when $T \leq T_K$. Thus, the self-energy corresponding to the Kondo channel $\mathbf{X}^{(2)}$ is sensitive to temperature and energy. It can be expected that the Kondo channel dominates the scattering due to spin-flip-associated tunneling in the vicinity of the Fermi level when $T \leq T_K$. The normal-channel scattering dominates the spin-flip effect for electrons with energies far away from the Fermi level or $T > T_K$. As shown in Fig. 2, the LDOS in the region far away from the Fermi level is temperature independent. It implies that an electron with energy far away from the Fermi level is mainly scattered by the normal channel. Figure 3 shows a detailed plot of the LDOS with energy in the vicinity of the Fermi level. The spectral functions for $T = 100T_K$, i.e., the normal case, are shown in Figs. 3(a) and 3(b) (dashed lines). The spin-flip scattering via the normal channel affects the diagonal part of the spectrum function $A_{\sigma\sigma}$ (or LDOS) very slightly for the case of $T = 100T_K$ (normal limit). But the dependence of the off-diagonal spectrum function $A_{\bar{\sigma}\sigma}$ on spin-flip scattering via the classical channel is stronger than for $A_{\sigma\sigma}$. When the temperature is decreased to the order of the Kondo temperature ($T = 10T_K$ and $1T_K$ in our case), the Kondo effect becomes obvious and the Kondo resonance peak grows logarithmically. As Figs. 3(a) and 3(b) (solid line) and Figs. 3(c) and 3(d) show, it is obvious that the

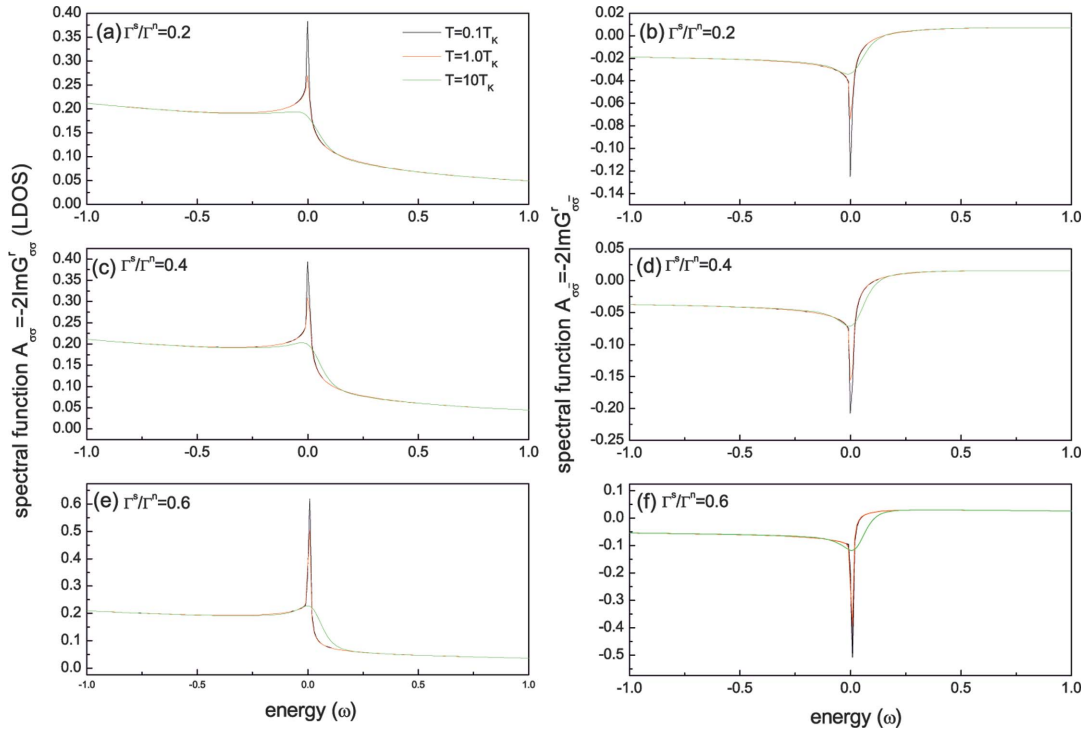


FIG. 2. (Color) The plot of spectral function as a function of ω with temperature $T=10T_K$, $1T_K$, and $T=0.1T_K$.

LDOS with energy near the Fermi level is strongly dependent on temperature when the temperature is close to the Kondo temperature. Therefore, it implies that the scattering in the region near the Fermi level is dominated by the Kondo channel. When the temperature is below the Kondo tempera-

ture ($T=0.1T_K$ in our case), the scattering via the Kondo channel is prominent. As shown in Figs. 3(e) and 3(f), there are two major effects due to the spin-flip-associated tunneling via the Kondo channel. The amplitude of the Kondo resonance peak is increased as Γ^s is increased, i.e., the

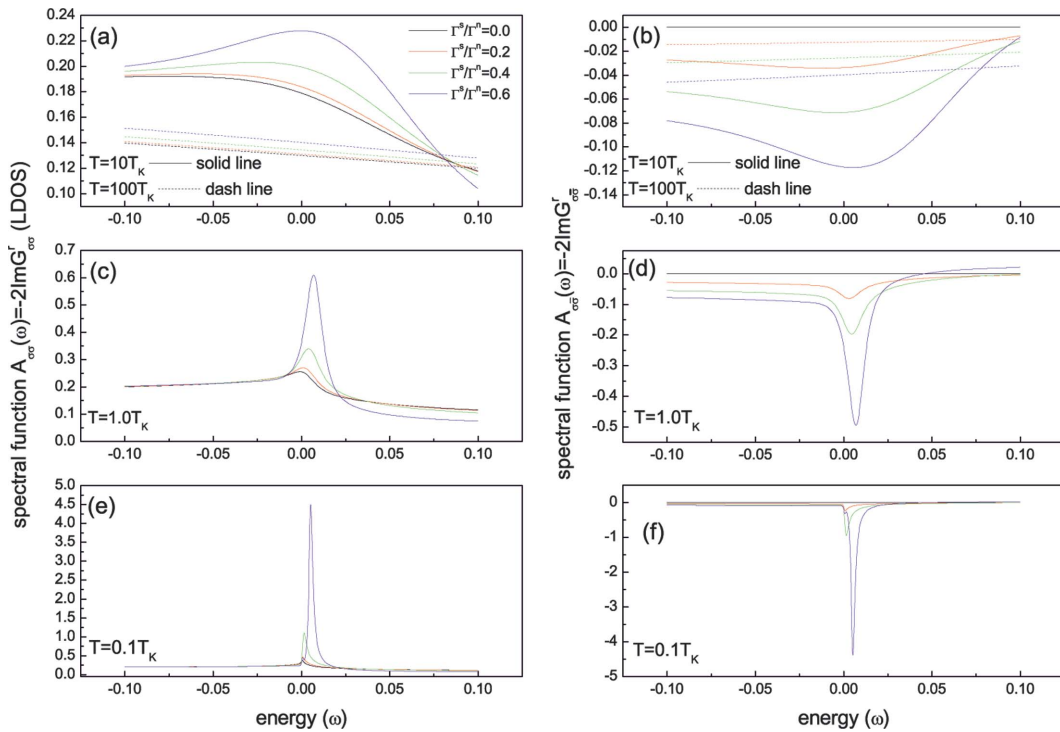


FIG. 3. (Color) The detailed plot of the spectral function in the vicinity of the Fermi level as a function of ω . $T=(a)100T_K$ and $10T_K$, (b) $1T_K$, and (c) $0.1T_K$ with various Γ^s/Γ^n .

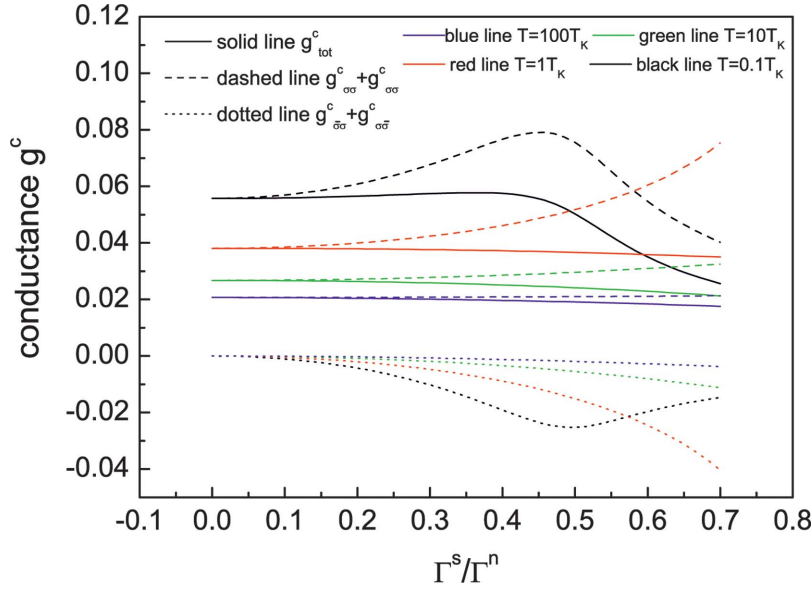


FIG. 4. (Color) The equilibrium conductance versus $\Gamma_\alpha^s/\Gamma_\alpha^n$ at various temperatures. The dashed line is the diagonal part. The dotted line is the off-diagonal part. The solid line is the total conductance. The blue line is $T=100T_K$, the green line $T=10T_K$, the red line is $T=1T_K$, and the black line is $T=0.1T_K$.

Kondo resonance peak is enhanced by the spin-flip-associated tunneling effect. In addition to the increasing of the peak height, the spin-flip tunneling also causes a blue-shift of the Kondo resonance. These effects become stronger as the temperature is decreased. Note that the enhancement and shift of the Kondo resonance peak due to spin-flip-associated tunneling will affect the conductance. Since the off-diagonal Green's function is $G_{\bar{\sigma}\sigma} = \tilde{G}_{\sigma\sigma}^0 \sum_{\bar{\sigma}\sigma} G_{\sigma\sigma}$, the profile of the off-diagonal spectral function $A_{\bar{\sigma}\sigma}$ is similar to that of the diagonal spectral function $A_{\sigma\sigma}$ but with opposite sign. It is worth noting that for the case of $T \geq T_K$, the decrease (to more negative values) of $A_{\bar{\sigma}\sigma}$ is faster than the increase of $A_{\sigma\sigma}$. This phenomenon is the main reason for suppression of the conductance for $T \geq T_K$.

The conductance g^c for the equilibrium case is calculated by Eq. (3) of Ref. 13. For the equilibrium situation, the current is contributed by the electrons with energy near the Fermi level of the leads. Thus, the equilibrium conductance reflects the properties of the Kondo resonance peak with energy in the vicinity of the Fermi level of the leads. Figure 4 shows the equilibrium conductance versus the spin-flip coupling constant Γ^s . One can find that for $\Gamma^s=0$, the total conductance g_{tot}^c is increased as the temperature is decreased, since the Kondo resonance peak is enhanced as the temperature is decreased. For the case of $T=100T_K$, the Kondo effect can be ignored and the scattering is dominated by the normal channel. As in previous discussion, the decrease of $A_{\bar{\sigma}\sigma}$ is faster than the increase of $A_{\sigma\sigma}$ as Γ^s is increased; hence the total conductance g_{tot}^c is dominated by the off-diagonal part conductance $g_{\bar{\sigma}\sigma}^c$ and decreased as Γ^s is increased. For the cases of $T=10T_K$ and $1.0T_K$ the Kondo effect appears; however, it is not obvious. One can find that $g_{\sigma\sigma}^c$ is increased slightly as Γ^s is increased for $\Gamma^s > 0.3\Gamma^n(0.1\Gamma^n)$. This phenomenon reflects the enhancement of the Kondo resonance peak due to the spin-flip effect via the Kondo channel as discussed previously. Similar to the case of $T=100T_K$, the total conductance is dominated by the off-diagonal conductance and decreased as Γ^s is increased. For the case of $T=0.1T_K$, the effect due to spin-flip scattering via the Kondo

channel becomes more prominent. The diagonal part $g_{\sigma\sigma}^c$ contains peak-enhancement and peak-shift effects due to spin-flip via the Kondo channel. For $\Gamma^s < 0.48$, the peak-enhancement effect is dominant and $g_{\sigma\sigma}^c$ increases as Γ^s is increased. For $\Gamma^s > 0.48$, the peak-shift effect is dominant and thus the peak height is shifted out of the vicinity of the Fermi level of the leads, and thus there are fewer electrons contributing to the conductance; hence $g_{\sigma\sigma}^c$ is decreased. The profile of the off-diagonal spectral function $A_{\bar{\sigma}\sigma}$ is similar to that of $A_{\sigma\sigma}$ except with the opposite sign; thus the behavior of the off-diagonal part of the conductance is similar to the diagonal part except for the sign. For $T=0.1T_K$ the total conductance is dominated by $g_{\sigma\sigma}^c$. In the region dominated by the peak-enhancement effect, i.e., $\Gamma^s < 0.48$, the total conductance is slightly increased as Γ^s is increased. In the region dominated by the peak-shift effect, the total conductance decreases as Γ^s is increased. Note that the conductance is suppressed rapidly for the case of $T=0.1T_K$ when $\Gamma^s > 0.48$. The rapid decrease of conductance is caused by the peak-shift effect due to spin-flip scattering.

For the nonequilibrium case, a quantum dot connected to two leads with different Fermi levels is studied. The Fermi levels of leads are set to be zero when the bias voltage is zero. When the bias voltage V_{bias} is applied, the Fermi levels of the leads are $E_F^R = -V_{bias}/2$ and $E_F^L = V_{bias}/2$. The nonequilibrium differential conductance is defined as $g^c = \Delta J / \Delta V_{bias}$, where the current J is calculated by the method of Ref. 25. The nonequilibrium differential conductance is shown in Fig. 5. Since the applied bias is symmetry, the conductance is symmetry for $V_{bias} > 0$ and $V_{bias} < 0$, as shown in Figs. 5(a) and 5(b). Following the same reasoning, the nonequilibrium differential conductance is decreased as Γ_s is increased for the cases of $T \geq T_K$. In the region $|V_{bias}| > 0.25$ the conductance is temperature insensitive. It implies that the nonequilibrium differential conductance for $|V_{bias}| > 0.25$ is dominated by the scattering via the normal channel, the behavior of the differential conductance is similar to the equilibrium case for $T > T_K$. Hence, for $|V_{bias}| > 0.25$, the differential conductance is decreased as Γ^s is increased. In the region with energy near the Fermi level, i.e., $|V_{bias}| < 0.25$, the Kondo

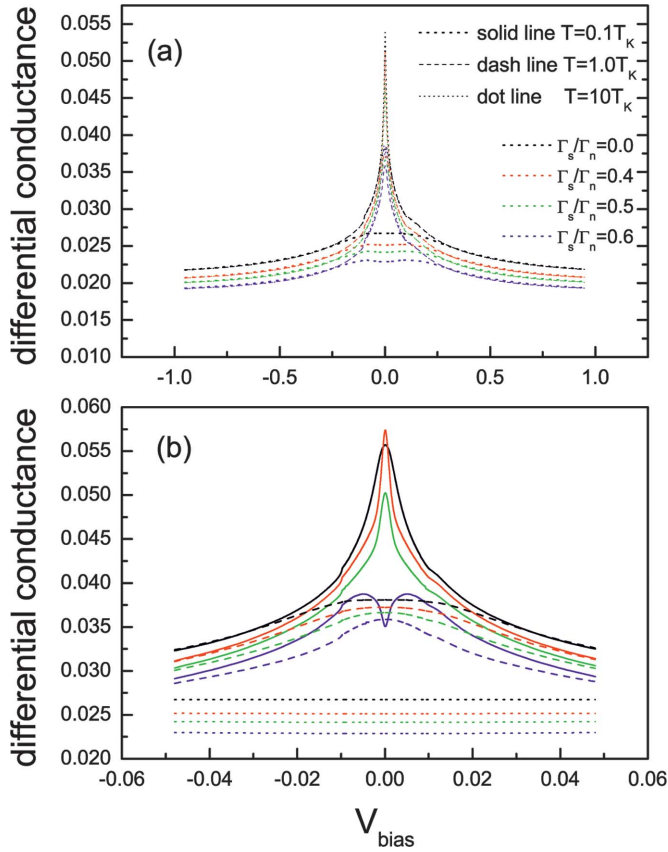


FIG. 5. (Color) (a) The differential conductance versus bias voltage with various Γ_s/Γ_n for different temperature. (b) A detailed plot of (a) with energy almost equal to zero bias voltage.

effect is more important when $T < T_k$. This is because the Kondo effect influences the LDOS only when the electron energy is near the Fermi level. The nonequilibrium differential conductance is influenced strongly by the Kondo effect when the bias voltage $|V_{bias}| \sim 0$ for $T \leq T_k$. Figure 5(b) shows a detailed plot of the nonequilibrium differential conductance with bias voltage $|V_{bias}| < 0.05$. The variation of the conductance for $|V_{bias}| \sim 0$ is similar to the case of $|V_{bias}| \gg 0$ when $T > T_k$ (the dotted line in Fig. 5) and the scattering is via the normal channel. As the temperature is decreased to $T \sim T_k$, the influence due to the Kondo effect becomes important and the Kondo resonance peak is prominent. Hence, the conductance is larger than the one for $T > T_k$. For $T = T_k$ (the dashed line in Fig. 5), the quantity of conductance suppression due to the spin-flip-associated tunneling is similar to that in the large-bias-voltage region. The suppression of conductance is due to the decrease of $g_{\sigma\bar{\sigma}}^c$ as Γ^s is increased. The prominence of the conductance reflects the prominent Kondo resonance peak of the LDOS. When $T \leq T_k$ (the solid line in Fig. 5), the influence of the peak shift of the Kondo resonance becomes important. As in the case of equilibrium, the $g_{\sigma\bar{\sigma}}^c$ is strongly suppressed by the shift of the Kondo resonance peak when Γ^s is large. As a result, the total conductance is suppressed rapidly when $\Gamma^s > 0.4$ and causes a valley when $\Gamma^s = 0.6$. Figures 6(a) and 6(b) show the spectral function for $T = 0.1T_K$ and $V_{bias} = 10^{-3}$. One can find that the LDOS within the Fermi level of the leads is increased as Γ^s

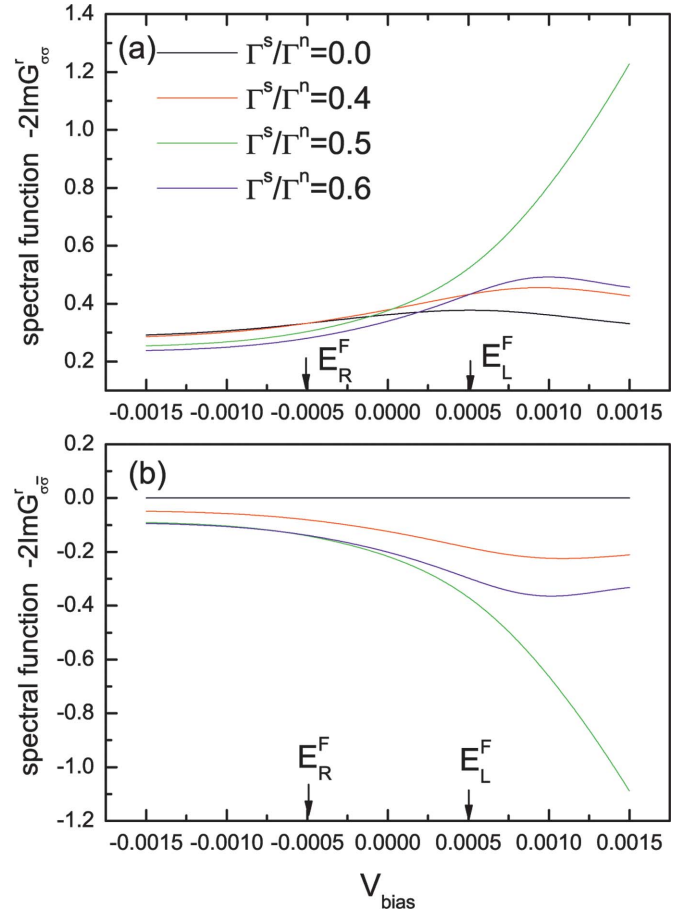


FIG. 6. (Color) (a) The nonequilibrium diagonal and (b) off-diagonal spectral functions for the case of $V_{bias} = 10^{-3}$ and $T = 0.1T_K$ with various Γ_s/Γ_n .

is increased when $\Gamma^s < 0.6$. This explains why the differential conductance is increased as Γ^s is increased when $\Gamma^s < 0.6$ and $T = 0.1T_K$ in the vicinity of $V_{bias} = 0$. For $\Gamma^s = 0.6$, the peak-shift effect shifts the peak height out of the region between the Fermi level of the leads and the total LDOS within the Fermi level of the leads is smaller than the LDOS for $\Gamma^s < 0.6$. Hence, the differential conductance appears slightly when $V_{bias} \sim 0$ for $T = 0.1T_K$ and $\Gamma^s = 0.6$. This tip of the conductance occurs when $T < T_k$ in the vicinity of the Fermi level of the leads, therefore, this phenomenon mainly originates from the scattering via the Kondo channel.

IV. SUMMARY

In summary, we study the spin-flip-associated tunneling in the Anderson model. The total effect can be interpreted as follows. As Eq. (6) shows, the quasiparticle described by the Anderson Hamiltonian is scattered via the normal and the Kondo channels. The normal channel dominates the scattering of the electrons with energy far away from the Fermi level of the lead. The electrons with energy near the Fermi level of the leads are mainly scattered by the Kondo channel when $T \leq T_k$. Note that only the infinite- U limit approximation is used in Eq. (6), i.e., Eq. (6) is a general form for the

Anderson model with spin-flip-associated tunneling in the infinite- U limit and does not relate to the decoupling method. The spin-flip-associated tunneling via the Kondo channel causes two main effects. One is the enhancement of the Kondo resonance peak; the other is the blueshift of the Kondo resonance peak. When the temperature $T=10T_K$ and $1.0T_K$, the Kondo resonance peak is obviously enhanced by spin-flip-associated tunneling effect, but the blueshift of the Kondo resonance peak is not obvious. This effect is reflected in the conductance. The enhancement of the Kondo resonant peak causes an increase of the diagonal part of the conductance $g_{\sigma\sigma}$ and decreases the off-diagonal part of the conductance $g_{\bar{\sigma}\sigma}$ (to more negative values). Since the decrease of the off-diagonal part of the conductance is stronger than the increase of the diagonal part of the conductance; as a result the total conductance is suppressed by spin-flip-associated tunneling. The conductance due to off-diagonal processes is negative and cannot be neglected. As the temperature gets lower, the blueshift of the Kondo resonance peak becomes important. When $T \leq T_k$ and the spin-flip-associated coupling constant Γ_s is large enough, the blueshift of the Kondo resonance peak will cause a strong suppression of the diagonal part of the conductance and the total conductance is suppressed rapidly. The conductance suppression due to the shift of the Kondo resonance peak is ascribed to the Kondo channel mainly, since the effect occurs as $T < T_K$. The high-

temperature Lacroix decoupling approximation is used to decouple the two-particle correlation function (or Green's function). Our result is quantitatively correct when $T > T_K$. The Kondo resonance peak is slightly enhanced and blueshifted as $T \geq T_K$. On the contrary, the Kondo resonance peak is enhanced prominently and blueshifted obviously in the case of $T=0.1T_k$. Although the decoupling approximation only gives a qualitative result for $T < T_K$, the conductance can be suppressed strongly by the spin-flip-associated tunneling effect for $T < T_K$.

ACKNOWLEDGMENT

This work is supported by the National Science Council of Taiwan under Grant No. NSC 94-2120-M-009-002.

APPENDIX A

First, we derive the general form of the Green's function for the spin-flip system. Assume that the lowest-order self-energies corresponding to the non-spin-flip transition processes $\sigma \rightarrow \sigma$ and $\bar{\sigma} \rightarrow \bar{\sigma}$ (the diagonal terms) are $\Sigma_{\sigma\sigma}$ and $\Sigma_{\bar{\sigma}\bar{\sigma}}$. And the lowest-order self-energies corresponding to the spin-flip transition processes $\bar{\sigma} \rightarrow \sigma$ and $\sigma \rightarrow \bar{\sigma}$ (the diagonal terms) are $\Sigma_{\sigma\bar{\sigma}}$ and $\Sigma_{\bar{\sigma}\sigma}$. The typical Dyson equation can be expressed as

$$\begin{aligned} \begin{bmatrix} G_{\sigma\sigma} & G_{\sigma\bar{\sigma}} \\ G_{\bar{\sigma}\sigma} & G_{\bar{\sigma}\bar{\sigma}} \end{bmatrix} &= \begin{bmatrix} G_{\sigma\sigma}^0 & 0 \\ 0 & G_{\bar{\sigma}\bar{\sigma}}^0 \end{bmatrix} + \begin{bmatrix} G_{\sigma\sigma}^0 & 0 \\ 0 & G_{\bar{\sigma}\bar{\sigma}}^0 \end{bmatrix} \begin{bmatrix} \Sigma_{\sigma\sigma} & \Sigma_{\sigma\bar{\sigma}} \\ \Sigma_{\bar{\sigma}\sigma} & \Sigma_{\bar{\sigma}\bar{\sigma}} \end{bmatrix} \begin{bmatrix} G_{\sigma\sigma} & G_{\sigma\bar{\sigma}} \\ G_{\bar{\sigma}\sigma} & G_{\bar{\sigma}\bar{\sigma}} \end{bmatrix} = \begin{bmatrix} G_{\sigma\sigma}^0 & 0 \\ 0 & G_{\bar{\sigma}\bar{\sigma}}^0 \end{bmatrix} \\ &+ \begin{bmatrix} G_{\sigma\sigma}^0 \Sigma_{\sigma\sigma} G_{\sigma\sigma} + G_{\sigma\sigma}^0 \Sigma_{\sigma\bar{\sigma}} G_{\bar{\sigma}\sigma} & G_{\sigma\sigma}^0 \Sigma_{\sigma\sigma} G_{\sigma\bar{\sigma}} + G_{\sigma\sigma}^0 \Sigma_{\sigma\bar{\sigma}} G_{\bar{\sigma}\bar{\sigma}} \\ G_{\bar{\sigma}\bar{\sigma}}^0 \Sigma_{\bar{\sigma}\sigma} G_{\sigma\sigma} + G_{\bar{\sigma}\bar{\sigma}}^0 \Sigma_{\bar{\sigma}\sigma} G_{\bar{\sigma}\sigma} & G_{\bar{\sigma}\bar{\sigma}}^0 \Sigma_{\bar{\sigma}\sigma} G_{\sigma\bar{\sigma}} + G_{\bar{\sigma}\bar{\sigma}}^0 \Sigma_{\bar{\sigma}\bar{\sigma}} G_{\bar{\sigma}\bar{\sigma}} \end{bmatrix}. \end{aligned} \quad (\text{A1})$$

The off-diagonal terms can be rewritten as $G_{\sigma\bar{\sigma}} = \tilde{G}_{\sigma\sigma}^0 \Sigma_{\sigma\bar{\sigma}} G_{\sigma\sigma}$ and $G_{\bar{\sigma}\sigma} = \tilde{G}_{\bar{\sigma}\bar{\sigma}}^0 \Sigma_{\bar{\sigma}\sigma} G_{\bar{\sigma}\bar{\sigma}}$ where $\tilde{G}_{\sigma\sigma}^0 \equiv [(G_{\sigma\sigma}^0)^{-1} - \Sigma_{\sigma\sigma}]^{-1}$ and $\tilde{G}_{\bar{\sigma}\bar{\sigma}}^0 \equiv [(G_{\bar{\sigma}\bar{\sigma}}^0)^{-1} - \Sigma_{\bar{\sigma}\bar{\sigma}}]^{-1}$. Substitute these expressions for $G_{\sigma\bar{\sigma}}$ and $G_{\bar{\sigma}\sigma}$ into the diagonal term, Eq. (8) becomes

$$\begin{bmatrix} G_{\sigma\sigma} & G_{\sigma\bar{\sigma}} \\ G_{\bar{\sigma}\sigma} & G_{\bar{\sigma}\bar{\sigma}} \end{bmatrix} = \begin{bmatrix} [(G_{\sigma\sigma}^0)^{-1} - \Sigma_{\sigma\sigma} - \Sigma_{\sigma\bar{\sigma}} \tilde{G}_{\bar{\sigma}\bar{\sigma}}^0 \Sigma_{\bar{\sigma}\sigma}]^{-1} & G_{\sigma\bar{\sigma}} = \tilde{G}_{\sigma\sigma}^0 \Sigma_{\sigma\bar{\sigma}} G_{\bar{\sigma}\bar{\sigma}} \\ \tilde{G}_{\bar{\sigma}\bar{\sigma}}^0 \Sigma_{\bar{\sigma}\sigma} G_{\sigma\sigma} & [(G_{\bar{\sigma}\bar{\sigma}}^0)^{-1} - \Sigma_{\bar{\sigma}\bar{\sigma}} - \Sigma_{\bar{\sigma}\sigma} \tilde{G}_{\sigma\sigma}^0 \Sigma_{\sigma\bar{\sigma}}]^{-1} \end{bmatrix}. \quad (\text{A2})$$

Equation (9) is the same as Eqs. (5a) and (5b) in Ref. 13 exactly.

APPENDIX B

In order to solve Eq. (4), one has to decouple the two correlation functions $\langle T\{c_{k\alpha s}^\dagger d_{\bar{\sigma}}^\dagger d_{\sigma}^\dagger\} \rangle$, $\langle T\{c_{k\alpha s}^\dagger d_{\sigma}^\dagger d_{\bar{\sigma}}^\dagger\} \rangle$, and $\langle T\{c_{k\alpha s}^\dagger d_{\sigma}^\dagger d_{\bar{\sigma}}^\dagger\} \rangle$, etc. The decoupling scheme proposed by Lacroix in the high-temperature limit

$$\begin{aligned} \langle T\{c_{k\alpha s}^\dagger(t) c_{k\beta s'}(t) d_{\bar{\sigma}}^\dagger(t), d_{\sigma}^\dagger(t')\} \rangle \\ = \delta_{k\alpha, k\beta} \delta_{s, s'} f(\epsilon_{k\alpha s}) \langle T\{d_{\bar{\sigma}}^\dagger(t), d_{\sigma}^\dagger(t')\} \rangle, \end{aligned}$$

$$\begin{aligned} \langle T\{c_{k\alpha s}^\dagger(t) c_{k\beta s'}(t) d_{\sigma}^\dagger(t), d_{\bar{\sigma}}^\dagger(t')\} \rangle \\ = \delta_{k\alpha, k\beta} \delta_{s, s'} f(\epsilon_{k\alpha s}) \langle T\{d_{\sigma}^\dagger(t), d_{\bar{\sigma}}^\dagger(t')\} \rangle, \end{aligned}$$

$$\begin{aligned} \langle T\{c_{k\alpha s}(t) c_{k\beta s'}(t) d_{\sigma}^\dagger(t), d_{\bar{\sigma}}^\dagger(t')\} \rangle \\ = \langle T\{c_{k\alpha s}(t) c_{k\beta s'}(t) d_{\bar{\sigma}}^\dagger(t), d_{\sigma}^\dagger(t')\} \rangle = 0 \end{aligned} \quad (\text{B1})$$

is used. For example, consider the term $\langle c_{k\alpha s}^\dagger d_{\bar{\sigma}}^\dagger d_{\sigma}^\dagger \rangle$ of Eq. (4). Using the EOM method, and Lacroix's high-temperature decoupling approximation, one obtains

$$\begin{aligned}
& (\omega - \epsilon_{kas} - \epsilon_\sigma + \epsilon_{\bar{\sigma}}) \langle T \{ c_{k_{\alpha s}} d_{\bar{\sigma}}^\dagger d_\sigma d_\sigma^\dagger \} \rangle \\
&= V_{k_{\alpha s}, \sigma} \langle T \{ d_\sigma d_\sigma^\dagger d_{\bar{\sigma}} d_{\bar{\sigma}}^\dagger \} \rangle + V_{k_{\alpha s}, \bar{\sigma}} \langle T \{ d_{\bar{\sigma}} d_{\bar{\sigma}}^\dagger d_\sigma d_\sigma^\dagger \} \rangle \\
&\quad - \sum_{q_{\alpha s'}} V_{q_{\alpha s'}, \bar{\sigma}} \langle T \{ c_{k_{\alpha s}} c_{q_{\alpha s'}}^\dagger d_\sigma d_\sigma^\dagger \} \rangle \\
&= - \langle d_{\bar{\sigma}}^\dagger d_\sigma \rangle V_{k_{\alpha s}, \sigma}(i) G_{\sigma\sigma} + V_{k_{\alpha s}, \bar{\sigma}}(i) (G_{\sigma\sigma} - G_{\sigma\sigma}^{(2)}) \\
&\quad - \sum_{q_{\alpha s'}} V_{q_{\alpha s'}, \bar{\sigma}} \langle c_{k_{\alpha s}} c_{q_{\alpha s'}}^\dagger \rangle (i) G_{\sigma\sigma} \delta_{k_{\alpha s}, q_{\alpha s'}}; \quad (B2)
\end{aligned}$$

thus

$$\begin{aligned}
& - \sum_{k_{\alpha s}} V_{k_{\alpha s}, \bar{\sigma}}^* (-i) \langle c_{k_{\alpha s}} d_{\bar{\sigma}}^\dagger d_\sigma d_\sigma^\dagger \rangle \\
&= \langle d_{\bar{\sigma}}^\dagger d_\sigma \rangle \sum_{k_{\alpha s}} \frac{V_{k_{\alpha s}, \bar{\sigma}}^* V_{k_{\alpha s}, \sigma}}{\omega - \epsilon_{kas} - \epsilon_\sigma + \epsilon_{\bar{\sigma}}} G_{\sigma\sigma} \\
&\quad + \sum_{k_{\alpha s}} \frac{|V_{k_{\alpha s}, \bar{\sigma}}|^2}{\omega - \epsilon_{kas} - \epsilon_\sigma + \epsilon_{\bar{\sigma}}} (G_{\sigma\sigma}^{(2)} - G_{\sigma\sigma}) \\
&\quad + \sum_{k_{\alpha s}} \frac{|V_{k_{\alpha s}, \bar{\sigma}}|^2}{\omega - \epsilon_{kas} - \epsilon_\sigma + \epsilon_{\bar{\sigma}}} [1 - f_\alpha(\epsilon_{kas})] G_{\sigma\sigma}. \quad (B3)
\end{aligned}$$

In the same way, the $\langle T \{ c_{k_{\alpha s}} d_{\bar{\sigma}}^\dagger d_\sigma d_\sigma^\dagger \} \rangle$ term of Eq. (4) is

$$\begin{aligned}
& \sum_{k_{\alpha s}} V_{k_{\alpha s}, \sigma}^* (-i) \langle T \{ c_{k_{\alpha s}} d_{\bar{\sigma}}^\dagger d_\sigma d_\sigma^\dagger \} \rangle \\
&= \sum_{k_{\alpha s}} \frac{|V_{k_{\alpha s}, \sigma}|^2}{\omega - \epsilon_{kas}} G_{\sigma\sigma}^{(2)} - \langle n_{\bar{\sigma}} \rangle \frac{V_{k_{\alpha s}, \sigma}^* V_{k_{\alpha s}, \bar{\sigma}}}{\omega - \epsilon_{kas}} G_{\bar{\sigma}\bar{\sigma}} \\
&\quad + \frac{V_{k_{\alpha s}, \sigma}^* V_{k_{\alpha s}, \bar{\sigma}}}{\omega - \epsilon_{kas}} f_\alpha(\epsilon_{kas}) G_{\bar{\sigma}\bar{\sigma}} \quad (B4)
\end{aligned}$$

and the $\langle T \{ c_{k_{\alpha s}}^\dagger d_\sigma d_{\bar{\sigma}} d_{\bar{\sigma}}^\dagger \} \rangle$ term is

$$\begin{aligned}
& \sum_{k_{\alpha s}} V_{k_{\alpha s}, \bar{\sigma}}^* (-i) \langle T \{ c_{k_{\alpha s}}^\dagger d_\sigma d_{\bar{\sigma}} d_{\bar{\sigma}}^\dagger \} \rangle \\
&= \sum_{k_{\alpha s}} - \frac{|V_{k_{\alpha s}, \sigma}|^2}{\omega + \epsilon_{kas} - \epsilon_\sigma - \epsilon_{\bar{\sigma}} - U} G_{\bar{\sigma}\bar{\sigma}}^{(2)} \\
&\quad - \frac{|V_{k_{\alpha s}, \sigma}|^2}{\omega + \epsilon_{kas} - \epsilon_\sigma - \epsilon_{\bar{\sigma}} - U} G_{\sigma\sigma}^{(2)} \\
&\quad + \sum_{k_{\alpha s}} \frac{|V_{k_{\alpha s}, \sigma}|^2}{\omega + \epsilon_{kas} - \epsilon_\sigma - \epsilon_{\bar{\sigma}} - U} f_\alpha(\epsilon_{kas}) G_{\bar{\sigma}\bar{\sigma}} \\
&\quad + \frac{V_{k_{\alpha s}, \bar{\sigma}}^* V_{k_{\alpha s}, \sigma}}{\omega + \epsilon_{kas} - \epsilon_\sigma - \epsilon_{\bar{\sigma}} - U} f_\alpha(\epsilon_{kas}) G_{\sigma\sigma}. \quad (B5)
\end{aligned}$$

Under the infinite- U limit, the Eq. (14) is zero. Compare to Eq. (5), The self-energy $Y_{\bar{\sigma}\bar{\sigma}}^{(2)}$ transfers $G_{\bar{\sigma}\bar{\sigma}}^{(2)}$ to $G_{\sigma\sigma}^{(2)}$, we can recognize that $Y_{\bar{\sigma}\bar{\sigma}}^{(2)} = \sum_{k_{\alpha s}} |V_{k_{\alpha s}, \sigma}|^2 / (\omega + \epsilon_{kas} - \epsilon_\sigma - \epsilon_{\bar{\sigma}} - U)$ and can be ignored under the infinite- U limit. Hence the Green's function $G_{\sigma\sigma}^{(2)}$ is found as

$$\begin{aligned}
& (\omega - \epsilon_\sigma - U) G_{\sigma\sigma}^{(2)}(\omega) \\
&= n_{\bar{\sigma}} + \sum_{k_{\alpha s}} \frac{|V_{k_{\alpha s}, \sigma}|^2}{\omega - \epsilon_{kas}} G_{\sigma\sigma}^{(2)} - \langle n_{\bar{\sigma}} \rangle \frac{V_{k_{\alpha s}, \sigma}^* V_{k_{\alpha s}, \bar{\sigma}}}{\omega - \epsilon_{kas}} G_{\bar{\sigma}\bar{\sigma}} \\
&\quad + \frac{V_{k_{\alpha s}, \sigma}^* V_{k_{\alpha s}, \bar{\sigma}}}{\omega - \epsilon_{kas}} f_\alpha(\epsilon_{kas}) G_{\bar{\sigma}\bar{\sigma}} + \langle d_{\bar{\sigma}}^\dagger d_\sigma \rangle \\
&\quad \sum_{k_{\alpha s}} \frac{V_{k_{\alpha s}, \bar{\sigma}}^* V_{k_{\alpha s}, \sigma}}{\omega - \epsilon_{kas} - \epsilon_\sigma + \epsilon_{\bar{\sigma}}} G_{\sigma\sigma} + \frac{|V_{k_{\alpha s}, \bar{\sigma}}|^2}{\omega - \epsilon_{kas} - \epsilon_\sigma + \epsilon_{\bar{\sigma}}} (G_{\sigma\sigma}^{(2)} \\
&\quad - G_{\sigma\sigma}) + \frac{|V_{k_{\alpha s}, \bar{\sigma}}|^2}{\omega - \epsilon_{kas} - \epsilon_\sigma + \epsilon_{\bar{\sigma}}} [1 - f_\alpha(\epsilon_{kas})] G_{\sigma\sigma} \equiv Y_{\sigma\sigma}^{(2)} G_{\sigma\sigma}^{(2)} \\
&\quad + X_{\sigma\sigma}^{(2)} G_{\sigma\sigma} + X_{\bar{\sigma}\bar{\sigma}}^{(2)} G_{\bar{\sigma}\bar{\sigma}} \quad (B6)
\end{aligned}$$

where

$$Y_{\sigma\sigma}^{(2)} \equiv \sum_{k_{\alpha s}} \frac{|V_{k_{\alpha s}, \sigma}|^2}{\omega - \epsilon_{kas}} + \frac{|V_{k_{\alpha s}, \bar{\sigma}}|^2}{\omega - \epsilon_{kas} - \epsilon_\sigma + \epsilon_{\bar{\sigma}}},$$

$$\begin{aligned}
X_{\sigma\sigma}^{(2)} &\equiv \sum_{k_{\alpha s}} \langle d_{\bar{\sigma}}^\dagger d_\sigma \rangle \frac{V_{k_{\alpha s}, \sigma}^* V_{k_{\alpha s}, \bar{\sigma}}}{\omega - \epsilon_{kas} - \epsilon_\sigma + \epsilon_{\bar{\sigma}}} \\
&\quad - \frac{|V_{k_{\alpha s}, \bar{\sigma}}|^2}{\omega - \epsilon_{kas} - \epsilon_\sigma + \epsilon_{\bar{\sigma}}} f_\alpha(\epsilon_{kas}),
\end{aligned}$$

$$\begin{aligned}
X_{\bar{\sigma}\bar{\sigma}}^{(2)} &= \sum_{k_{\alpha s}} - \langle n_{\bar{\sigma}} \rangle \frac{V_{k_{\alpha s}, \sigma}^* V_{k_{\alpha s}, \bar{\sigma}}}{\omega - \epsilon_{kas}} + \frac{V_{k_{\alpha s}, \sigma}^* V_{k_{\alpha s}, \bar{\sigma}}}{\omega - \epsilon_{kas}} f_\alpha(\epsilon_{kas}). \quad (B7)
\end{aligned}$$

APPENDIX C

In this appendix, we will show the detailed derivation of the expressions for $\langle n_\sigma \rangle$ and $\langle n_{\bar{\sigma}} \rangle$. We follow the derivation proposed by Sun and Guo. Since the system considered in this paper is in steady state, the first derivation of the expectation values of $\langle d_\sigma^\dagger d_\sigma \rangle$ and $\langle d_{\bar{\sigma}}^\dagger d_{\bar{\sigma}} \rangle$ over time is zero, i.e., $\langle i(\partial/\partial t)[d_\sigma^\dagger d_\sigma] \rangle = 0$. Using the equation of motion method, one can find the time evolution of particle number $\langle d_\sigma^\dagger d_\sigma \rangle$ as

Hence,

$$\left\langle i \frac{\partial}{\partial t} [d_\sigma^\dagger d_\sigma] \right\rangle = \sum_{kas} - V_{kas, \sigma} \langle c_{kas}^\dagger d_\sigma \rangle + V_{kas, \sigma}^* \langle d_\sigma^\dagger c_{kas} \rangle = 0 \quad (C1)$$

where $\langle c_{kas}^\dagger d_\sigma \rangle = -i \int (d\epsilon/2\pi) G_{\sigma, kas}^<(\epsilon)$ and $\langle d_\sigma^\dagger c_{kas} \rangle = -i \int (d\epsilon/2\pi) G_{kas, \sigma}^<(\epsilon)$. The lesser Green's functions $G_{\sigma, kas}^<(\epsilon)$ and $G_{kas, \sigma}^<(\epsilon)$ can be easily calculated by the Dyson expansion and Langreth theorem. In order to calculate the lesser Green's function, the contour-ordered Green's function must be found first. The contour Green's function $G_{kas, \sigma}(t, t')$ is

$$\begin{aligned}
G_{kas,\sigma}(t,t') &= -iT\langle c_{kas}(t)d_{\sigma}^{\dagger}(t') \rangle \\
&= (-i)^2 T \int d\tau [V_{kas,\sigma} \langle c_{kas}(t)c_{kas}^{\dagger}(\tau) \rangle \langle d_{\sigma} d_{\sigma}^{\dagger}(t') \rangle \\
&\quad + V_{kas,\bar{\sigma}} \langle c_{kas}(t)c_{kas}^{\dagger}(\tau) \rangle \langle d_{\bar{\sigma}} d_{\bar{\sigma}}^{\dagger}(t') \rangle] \\
&= T \int d\tau [V_{kas,\sigma} g_{kas}(t,\tau) G_{\sigma\sigma}(\tau,t') \\
&\quad + V_{kas,\bar{\sigma}} g_{kas}(t,\tau) G_{\bar{\sigma}\bar{\sigma}}(\tau,t')]. \tag{C2}
\end{aligned}$$

Then, using the Fourier transformation and Langreth theorem, the lesser Green's function $G_{kas,\sigma}^<$ is obtained:

$$\begin{aligned}
G_{kas,\sigma}^< &= V_{kas,\sigma} (g_{kas}^r G_{\sigma\sigma}^< + g_{kas}^< G_{\sigma\sigma}^a) + V_{kas,\bar{\sigma}} (g_{kas}^r G_{\bar{\sigma}\bar{\sigma}}^< \\
&\quad + g_{kas}^< G_{\bar{\sigma}\bar{\sigma}}^a). \tag{C3}
\end{aligned}$$

In the same way, the lesser Green's function $G_{\sigma,kas}^<$ is

$$\begin{aligned}
G_{\sigma,kas}^< &= V_{kas,\sigma}^* (G_{\sigma\sigma}^r g_{kas}^< + G_{\sigma\sigma}^< g_{kas}^a) + V_{kas,\bar{\sigma}}^* (G_{\bar{\sigma}\bar{\sigma}}^r g_{kas}^< \\
&\quad + G_{\bar{\sigma}\bar{\sigma}}^< g_{kas}^a). \tag{C4}
\end{aligned}$$

Substituting Eqs. (C3) and (C4) into Eq. (C1), one can obtain

$$\begin{aligned}
&\sum_{k_{\alpha s}} \int \frac{d\epsilon}{2\pi} V_{k_{\alpha s},\sigma}^* V_{k_{\alpha s},\sigma} [G_{\sigma\sigma}^r g_{k_{\alpha s}}^<(\epsilon) + G_{\sigma\sigma}^<(\epsilon) g_{k_{\alpha s}}^a(\epsilon)] \\
&\quad + V_{k_{\alpha s},\bar{\sigma}}^* V_{k_{\alpha s},\bar{\sigma}} [G_{\bar{\sigma}\bar{\sigma}}^r(\epsilon) g_{k_{\alpha s}}^< + G_{\bar{\sigma}\bar{\sigma}}^<(\epsilon) g_{k_{\alpha s}}^a] \\
&= \sum_{k_{\alpha s}} \int \frac{d\epsilon}{2\pi} V_{k_{\alpha s},\sigma}^* V_{k_{\alpha s},\sigma} (g_{k_{\alpha s}}^r G_{\sigma\sigma}^< + g_{k_{\alpha s}}^< G_{\sigma\sigma}^a) \\
&\quad + V_{k_{\alpha s},\bar{\sigma}}^* V_{k_{\alpha s},\bar{\sigma}} (g_{k_{\alpha s}}^r G_{\bar{\sigma}\bar{\sigma}}^< + g_{k_{\alpha s}}^< G_{\bar{\sigma}\bar{\sigma}}^a). \tag{C5}
\end{aligned}$$

Using the relations $\sum_{k_{\alpha s}} V_{k_{\alpha s},\sigma}^* V_{k_{\alpha s},\sigma} g_{k_{\alpha s}}^{r,a} = \sum_{\alpha} \mp i(\Gamma_n^{\alpha}/2)$, $\sum_{k_{\alpha s}} V_{k_{\alpha s},\bar{\sigma}}^* V_{k_{\alpha s},\bar{\sigma}} g_{k_{\alpha s}}^{r,a} = \sum_{\alpha} \mp i(\Gamma_s^{\alpha}/2)$, $\sum_{k_{\alpha s}} V_{k_{\alpha s},\sigma}^* V_{k_{\alpha s},\sigma} g_{k_{\alpha s}}^<$ $= i\sum_{\alpha} \Gamma_n^{\alpha} f_{\alpha}(\epsilon)$, and $\sum_{k_{\alpha s}} V_{k_{\alpha s},\bar{\sigma}}^* V_{k_{\alpha s},\bar{\sigma}} g_{k_{\alpha s}}^< = i\sum_{\alpha} \Gamma_s^{\alpha} f_{\alpha}(\epsilon)$, and after some simple algebra, one finds

$$\begin{aligned}
&(\Gamma_n^2 - \Gamma_s^2) \int \frac{d\epsilon}{2\pi} G_{\sigma\sigma}^<(\epsilon) \\
&= \Gamma_n \left(\sum_{\alpha} -i\Gamma_n^{\alpha} \int \frac{d\epsilon}{2\pi} f_{\alpha}(\epsilon) [2 \text{Im} G_{\sigma\sigma}^r(\epsilon)] \right. \\
&\quad \left. - i\Gamma_s^{\alpha} \int \frac{d\epsilon}{2\pi} f_{\alpha}(\epsilon) [2 \text{Im} G_{\bar{\sigma}\bar{\sigma}}^r(\epsilon)] \right) \\
&\quad - \Gamma_s \left(\sum_{\alpha} -i\Gamma_s^{\alpha} \int \frac{d\epsilon}{2\pi} f_{\alpha}(\epsilon) [2 \text{Im} G_{\sigma\sigma}^r(\epsilon)] \right. \\
&\quad \left. - i\Gamma_n^{\alpha} \int \frac{d\epsilon}{2\pi} f_{\alpha}(\epsilon) [2 \text{Im} G_{\bar{\sigma}\bar{\sigma}}^r(\epsilon)] \right) \tag{C6}
\end{aligned}$$

where $\Gamma_n = \sum_{\alpha} \Gamma_n^{\alpha}$ and $\Gamma_s = \sum_{\alpha} \Gamma_s^{\alpha}$. In Eq. (C6), we have used

the relation $G_{\bar{\sigma}\bar{\sigma}}^{r,a,<}(\epsilon) = G_{\sigma\sigma}^{r,a,<}(\epsilon)$ since the spin states are degenerate in the QD. In the same way for treating $\langle i(\partial/\partial t) \times [d_{\sigma}^{\dagger} d_{\sigma}] \rangle = 0$, with the condition $\langle i(\partial/\partial t) [d_{\bar{\sigma}}^{\dagger} d_{\bar{\sigma}}] \rangle = 0$, one obtains the relation

$$\begin{aligned}
&(\Gamma_n^2 - \Gamma_s^2) \int \frac{d\epsilon}{2\pi} G_{\bar{\sigma}\bar{\sigma}}^<(\epsilon) \\
&= \Gamma_n \left(\sum_{\alpha} -i\Gamma_s^{\alpha} \int \frac{d\epsilon}{2\pi} f_{\alpha}(\epsilon) [2 \text{Im} G_{\sigma\sigma}^r(\epsilon)] \right. \\
&\quad \left. - i\Gamma_n^{\alpha} \int \frac{d\epsilon}{2\pi} f_{\alpha}(\epsilon) [2 \text{Im} G_{\bar{\sigma}\bar{\sigma}}^r(\epsilon)] \right) \\
&\quad - \Gamma_s \left(\sum_{\alpha} -i\Gamma_n^{\alpha} \int \frac{d\epsilon}{2\pi} f_{\alpha}(\epsilon) [2 \text{Im} G_{\sigma\sigma}^r(\epsilon)] \right. \\
&\quad \left. - i\Gamma_s^{\alpha} \int \frac{d\epsilon}{2\pi} f_{\alpha}(\epsilon) [2 \text{Im} G_{\bar{\sigma}\bar{\sigma}}^r(\epsilon)] \right). \tag{C7}
\end{aligned}$$

Since the retarded (advanced) Green's functions have been solved, the equations for $\int (d\epsilon/2\pi) G_{\sigma\sigma}^<(\epsilon)$ and $\int (d\epsilon/2\pi) G_{\bar{\sigma}\bar{\sigma}}^<(\epsilon)$ can be solved also. The results can be checked by taking the equilibrium limit, i.e., $f_R(\epsilon) = f_L(\epsilon) = f(\epsilon)$,

$$\langle n_{\sigma} \rangle = -i \int \frac{d\epsilon}{2\pi} G_{\sigma\sigma}^<(\epsilon) = \int \frac{d\epsilon}{2\pi} f_{\alpha}(\epsilon) [-2 \text{Im} G_{\sigma\sigma}^r(\epsilon)] \tag{C8}$$

and

$$\langle d_{\sigma}^{\dagger} d_{\sigma} \rangle = -i \int \frac{d\epsilon}{2\pi} G_{\bar{\sigma}\bar{\sigma}}^<(\epsilon) = \int \frac{d\epsilon}{2\pi} f_{\alpha}(\epsilon) [-2 \text{Im} G_{\bar{\sigma}\bar{\sigma}}^r(\epsilon)]. \tag{C9}$$

Equations (C8) and (C9) show that Eqs. (C6) and (C7) obey the fluctuation-dissipation theorem at the equilibrium limit:

$$\begin{aligned}
&\Gamma_n \int \frac{d\epsilon}{2\pi} G_{\sigma\sigma}^<(\epsilon) + \Gamma_s \int \frac{d\epsilon}{2\pi} G_{\bar{\sigma}\bar{\sigma}}^<(\epsilon) \\
&= \sum_{\alpha} -\Gamma_n^{\alpha} \int \frac{d\epsilon}{2\pi} f_{\alpha}(\epsilon) [G_{\sigma\sigma}^r(\epsilon) - G_{\sigma\sigma}^a(\epsilon)] \\
&\quad - \Gamma_s^{\alpha} \int \frac{d\epsilon}{2\pi} f_{\alpha}(\epsilon) [G_{\bar{\sigma}\bar{\sigma}}^r(\epsilon) - G_{\bar{\sigma}\bar{\sigma}}^a(\epsilon)], \tag{C10}
\end{aligned}$$

$$\begin{aligned}
&\Gamma_s \int \frac{d\epsilon}{2\pi} G_{\sigma\sigma}^<(\epsilon) + \Gamma_n \int \frac{d\epsilon}{2\pi} G_{\bar{\sigma}\bar{\sigma}}^<(\epsilon) \\
&= \sum_{\alpha} -\Gamma_s^{\alpha} \int \frac{d\epsilon}{2\pi} f_{\alpha}(\epsilon) [G_{\sigma\sigma}^r(\epsilon) - G_{\sigma\sigma}^a(\epsilon)] \\
&\quad - \Gamma_n^{\alpha} \int \frac{d\epsilon}{2\pi} f_{\alpha}(\epsilon) [G_{\bar{\sigma}\bar{\sigma}}^r(\epsilon) - G_{\bar{\sigma}\bar{\sigma}}^a(\epsilon)]. \tag{C11}
\end{aligned}$$

- ¹M. Dax, *Semicond. Int.* **20**, 84 (1997).
- ²H. X. Tang, F. G. Monzon, Ron Lifshitz, M. C. Cross, and M. L. Roukes, *Phys. Rev. B* **61**, 4437 (2000); X. F. Wang, P. Vasiliopoulos and F. M. Peeters, *ibid.* **65**, 165217 (2002).
- ³B. E. Kane, *Nature (London)* **393**, 133 (1998).
- ⁴S. Bandyopadhyay, *Phys. Rev. B* **61**, 13813 (2000).
- ⁵F. Guinea, *Phys. Rev. B* **58**, 9212 (1998).
- ⁶A. V. Akimov, A. V. Scherbakov, D. R. Yakovlev, W. Ossau, L. W. Molenkamp, T. Wojtowicz, J. Kossut, S. Tatarenko, and J. Cibert, *Physica B* **316-317**, 41 (2002).
- ⁷F. T. Vasko and O. Keller, *Phys. Rev. B* **58**, 15666 (1998).
- ⁸P. Zhang, Q. K. Xue, Y. P. Wang, and X. C. Xie, *Phys. Rev. Lett.* **89**, 286803 (2002).
- ⁹N. Sergueev, Qing-feng Sun, Hong Guo, B. G. Wang, and Jian Wang, *Phys. Rev. B* **65**, 165303 (2002).
- ¹⁰J. Martinek, Y. Utsumi, H. Imamura, J. Barnas, S. Maekawa, J. Konig, and G. Schon, *Phys. Rev. Lett.* **91**, 127203 (2003).
- ¹¹Bing Dong, H. L. Cui, S. Y. Liu, and X. L. Lei, *J. Phys.: Condens. Matter* **15**, 8435 (2003).
- ¹²J. Martinek, M. Sindel, L. Borda, J. Barnas, J. Konig, G. Schon, and J. von Delft, *Phys. Rev. Lett.* **91**, 247202 (2003).
- ¹³Jian-Xin Zhu and A. V. Balatsky, *Phys. Rev. Lett.* **89**, 286802 (2002).
- ¹⁴L. I. Glazman and M. E. Raikh, *Pis'ma Zh. Eksp. Teor. Fiz.* **47**, 378 (1988) [*JETP Lett.* **47**, 452 (1988)]; Tai Kai Ng and Patrick A. Lee, *Phys. Rev. Lett.* **61**, 1768 (1988).
- ¹⁵P. W. Anderson, *Phys. Rev.* **124**, 41 (1961).
- ¹⁶L. Kouwenhoven and L. Glazman, *Phys. World* **14** (1), 33 (2001).
- ¹⁷J. R. Schrieffer and P. A. Wolff, *Phys. Rev.* **149**, 491 (1966).
- ¹⁸Ned S. Wingreen, and Yigal Meir, *Phys. Rev. B* **49**, 11040 (1994).
- ¹⁹C. Lacroix, *J. Phys. F: Met. Phys.* **11**, 2389 (1981).
- ²⁰Yigal Meir, Ned S. Wingreen, and Patrick A. Lee, *Phys. Rev. Lett.* **70**, 2601 (1993).
- ²¹Kicheon Kang and B. I. Min, *Phys. Rev. B* **52**, 10689 (1995).
- ²²H.-G. Luo, Z.-J. Ying, and S.-J. Wang, *Phys. Rev. B* **59**, 9710 (1999).
- ²³T. A. Costi, A. C. Hewson, and V. Zlatic, *J. Phys.: Condens. Matter* **6**, 2519 (1994).
- ²⁴Qing-feng Sun and Hong Guo, *Phys. Rev. B* **66**, 155308 (2002).
- ²⁵Antti-Pekka Jauho, Ned S. Wingreen, and Yigal Meir, *Phys. Rev. B* **50**, 5528 (1994).
- ²⁶F. D. M. Haldane, Ph.D. thesis, University of Cambridge, 1987; *Phys. Rev. Lett.* **40**, 416 (1978).
- ²⁷The temperature of interest in Ref. 20 is an order of 2 lower than the Kondo temperature; however, the temperature considered in our work is about one-tenth of the Kondo temperature, Therefore, our decoupling approach sounds reasonable.

Spin relaxation in a GaAs quantum dot embedded inside a suspended phonon cavity

Y. Y. Liao,¹ Y. N. Chen,¹ D. S. Chuu,^{1,*} and T. Brandes²

¹*Department of Electrophysics, National Chiao-Tung University, Hsinchu 300, Taiwan*

²*School of Physics and Astronomy, The University of Manchester, P.O. Box 88, Manchester M60 1QD, United Kingdom*

(Received 23 September 2005; revised manuscript received 27 December 2005; published 10 February 2006)

The phonon-induced spin relaxation in a two-dimensional quantum dot embedded inside a semiconductor slab is investigated theoretically. An enhanced relaxation rate is found due to the phonon van Hove singularities. Oppositely, a vanishing deformation potential may also result in a suppression of the spin relaxation rate. For larger quantum dots, the interplay between the spin orbit interaction and Zeeman levels causes the suppression of the relaxation at several points. Furthermore, a crossover from confined to bulklike systems is obtained by varying the width of the slab.

DOI: [10.1103/PhysRevB.73.085310](https://doi.org/10.1103/PhysRevB.73.085310)

PACS number(s): 73.21.La, 71.70.Ej, 63.20.Dj, 72.25.Rb

Spin properties in nanostructures have become a field of intense research ranging from spin field-effect transistor,¹ spin-polarized *p-n* junctions,² up to quantum spin computers.³ The quantum dot (QD) may be a good choice for quantum electronics due to its zero dimensionality, quantized energy levels, and long coherence times of spin states.^{6,7} For example, the spin of an electron confined to a QD can form a qubit.^{4,5} However, some scattering processes will cause the change of the spin states. One important process is related to the phonon-induced spin-flip resulting from the spin-orbit interaction. This affects the time of spin purity in the QD. In order to keep the information unchanged, a long relaxation time is required.

In general, the spin-orbit (SO) coupling, which is one of the main causes of spin relaxation, is a relevant intrinsic interaction in nonmagnetic semiconductors. It is known that there are two different types of spin-orbit coupling as QDs are fabricated within semiconductors of a zinc-blende structure. The first one is the Dresselhaus interaction, which is due to the bulk inversion asymmetry of the lattice.⁸⁻¹⁰ The second is the Rashba interaction caused by the structure inversion asymmetry.¹¹ The spin-orbit couplings mix the spin states with different orientations in the Zeeman sublevels¹²⁻¹⁵ and therefore make spin relaxation possible in the presence of the electron-phonon interaction.

Relaxation times of electron spins in a QD have been measured by electrical pump-probe experiments.¹⁶ The triplet-to-singlet transition with emission of phonons was found with corresponding spin relaxation times of about 200 μ s. Recently, the spin relaxation time in a one-electron GaAs QD was measured by a similar electrical pump-probe technique.^{17,18} As the magnetic field was applied parallel to the two-dimensional electron gas, the Zeeman splitting of QD was observed in dc transport spectroscopy. By monitoring the relaxation of the spin, the relaxation time was found to have a lower bound of 50 μ s at an in-plane field of 7.5 T.¹⁷

On the theoretical side, spin relaxation between two spin-mixed states in semiconductor QDs has been studied recently. However, to the best of our knowledge, all previous studies of spin relaxation have concentrated on QDs embedded in the bulk material,¹⁹⁻²⁴ whereas studies of spin relaxation induced by confined phonons are still lacking. In this work, we therefore consider a single QD embedded into a

free-standing structure (semiconductor slab), where the relevant characteristic is the two-dimensional phonon wave vector for the acoustic-phonon spectrum as shown in Fig. 1.²⁵⁻²⁹ Since the reduced dimension will enhance the deformation potential, we will mainly focus on the spin relaxation rate induced by the deformation potential.²⁵⁻²⁷ In this paper we describe the model with spin-orbit coupling. Energy spectra of the QD can be solved by using an exact diagonalization method. We then apply the Fermi golden rule to calculate spin relaxation rates for typical parameters. We discuss the dependence of the spin relaxation rates on the size of the QD, the phonon bath temperature, and the width of the slab.

We consider an isotropic QD with an in-plane parabolic lateral confinement potential. An external magnetic field B is applied perpendicularly to the surface of the QD as shown in Fig. 1(a). The electronic Hamiltonian of this system can be written as

$$H_e = H_0 + H_{SO}. \quad (1)$$

The first term describes the electron Hamiltonian without the spin-orbit coupling

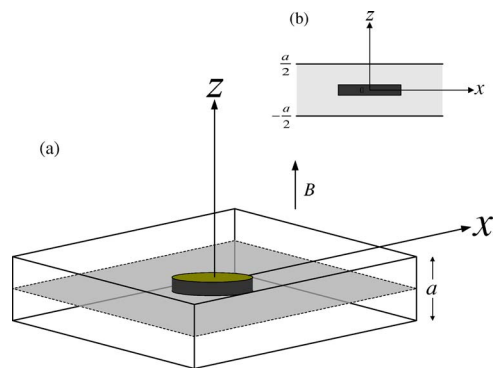


FIG. 1. (Color online) (a) Schematic view of single QD embedded in the semiconductor slab with a width of a . (b) The side view shows a QD is located at $z=0$.

$$H_0 = \frac{\mathbf{P}^2}{2m^*} + \frac{1}{2}m^*\omega_0^2r^2 + \frac{1}{2}g^*\mu_B B\sigma_z, \quad (2)$$

where $\mathbf{P} = -i\hbar\nabla + (e/c)\mathbf{A}$ is the kinetic momentum with vector potential $\mathbf{A} = (B/2)(-y, x, 0)$ confined to the 2D plane. Here m^* is the effective electron mass, e is the electron charge, c is the velocity of light, ω_0 is the characteristic confined frequency, g^* is the bulk g factor, μ_B is the Bohr magneton, and σ_z is a Pauli matrix.

The Rashba and Dresselhaus interactions ($H_{SO} = H_R + H_D$) are given by

$$H_R = \frac{\lambda_R}{\hbar}(\sigma_x P_y - \sigma_y P_x), \quad (3)$$

$$H_D = \frac{\lambda_D}{\hbar}(-\sigma_x P_x + \sigma_y P_y). \quad (4)$$

The coupling constants λ_R and λ_D determine the spin-orbit strengths, which depend on the band-structure parameters of the material. In addition, the Rashba and Dresselhaus terms are also associated to the perpendicular confinement field and the confinement width in the z direction, respectively.

For the electron Hamiltonian H_0 , the well-known Fock-Darwin states $\Psi_{n,l,\sigma}$ can be easily obtained. The corresponding electron energy levels are $E_{n,l,\sigma} = \hbar\Omega(2n + |l| + 1) + \hbar\omega_B l/2 + \sigma E_B$, where $n = (0, 1, 2, \dots)$ and $l = (0, \pm 1, \pm 2, \dots)$ are the quantum numbers. The renormalized frequency is $\Omega = \sqrt{\omega_0^2 + \omega_B^2}$, with the cyclotron frequency $\omega_B = eB/m^*$ and the characteristic confinement frequency ω_0 limited by the effective QD lateral length $l_0 = \sqrt{\hbar/m^*}\omega_0$. Here, $E_B = g\mu_B B/2$ is the Zeeman splitting energy, and $\sigma = \pm 1$ refers to the electron-spin polarization along the z axis. To solve the Schrödinger equation with ($H_e = H_0 + H_{SO}$), the (spin mixing) wave function is expressed in terms of a series of eigenfunctions $\Psi(r, \theta) = \sum c_{n,l,\sigma} \Psi_{n,l,\sigma}$ for each state l . After exactly diagonalizing the electron Hamiltonian, the corresponding eigenvalues E_l and the coefficient $c_{n,l,\sigma}$ can be obtained numerically.

Before calculating the spin relaxation rate, the confined phonon in the free-standing structure must be introduced here. Following Ref. 25, we consider an infinite film with width a (Fig. 1). For the effect of the contact with the semiconductor substrate, we neglect the distortion of the acoustic vibrations. Under this consideration, one can ensure that the in-plane wavelength can be shorter than the characteristic in-plane size of the solid slab. For simplicity, the elastic properties of the slab are isotropic. Small elastic vibrations of a solid slab can then be defined by a vector of relative displacement $\mathbf{u}(\mathbf{r}, t)$. Under the isotropic elastic continuum approximation, the displacement field \mathbf{u} obeys the equation

$$\frac{\partial^2 \mathbf{u}}{\partial t^2} = c_l^2 \nabla^2 \mathbf{u} + (c_l^2 - c_t^2) \nabla (\nabla \cdot \mathbf{u}), \quad (5)$$

where c_l and c_t are the velocities of longitudinal and transverse bulk acoustic waves. To define a system of confined modes, Eq. (5) should be complemented by the boundary conditions at the slab surface $z = \pm a/2$. Because of the con-

finement, phonons will be quantized in subbands. For each in-plane component \mathbf{q}_{\parallel} of the in-plane wave vector there are infinitely many subbands. Since two types of velocities of sound exist in the elastic medium, there are also two transversal wavevectors q_l and q_t . In the following, we consider the deformation potential only. This means there are two confined acoustic modes: dilatational waves and flexural waves contribute, but shear waves are neglected because of their vanishing interaction with the electrons for spin relaxation.

For dilatational waves, the parameters $q_{l,n}$ and $q_{t,n}$ can be determined from the Rayleigh-Lamb equation

$$\frac{\tan(q_{l,n}a/2)}{\tan(q_{t,n}a/2)} = -\frac{4q_{\parallel}q_{l,n}q_{t,n}}{(q_{\parallel}^2 - q_{t,n}^2)^2}, \quad (6)$$

with the dispersion relation

$$\omega_{n,q_{\parallel}} = c_l^2 \sqrt{q_{\parallel}^2 + q_{l,n}^2} = c_t^2 \sqrt{q_{\parallel}^2 + q_{t,n}^2}, \quad (7)$$

where $\omega_{n,q_{\parallel}}$ is the frequency of the dilatational wave in mode $(n, \mathbf{q}_{\parallel})$. For the antisymmetric flexural waves, the solutions $q_{l,n}$ and $q_{t,n}$ also can be determined by solving the equation

$$\frac{\tan(q_{l,n}a/2)}{\tan(q_{t,n}a/2)} = -\frac{4q_{\parallel}q_{l,n}q_{t,n}}{(q_{\parallel}^2 - q_{t,n}^2)^2}, \quad (8)$$

together with the dispersion relation (7).

The electron-phonon interaction through the deformation is given by $H_{ep} = E_a \text{div } \mathbf{u}$, where E_a is the deformation-potential coupling constant. The Hamiltonian can be written as

$$H_{ep} = \sum_{\substack{\mathbf{q}_{\parallel}, n \\ \lambda=d,f}} M_{\lambda}(\mathbf{q}_{\parallel}, n, z)(a_{\mathbf{q}_{\parallel}}^{\dagger} + a_{\mathbf{q}_{\parallel}}) \exp(i\mathbf{q}_{\parallel} \cdot \mathbf{r}_{\parallel}), \quad (9)$$

where \mathbf{r}_{\parallel} is the coordinate vector in the x - y plane and the functions M_d and M_f describe the intensity of the electron interactions with the dilatational and flexural waves, and are given by

$$M_d(q_{\parallel}, n, z) = F_{d,n} \sqrt{\frac{\hbar E_a^2}{2A\rho\omega_{n,q_{\parallel}}}} \left[(q_{t,n}^2 - q_{\parallel}^2)(q_{l,n}^2 + q_{\parallel}^2) \times \sin\left(\frac{aq_{t,n}}{2}\right) \cos(q_{l,n}z) \right], \quad (10)$$

$$M_f(q_{\parallel}, n, z) = F_{f,n} \sqrt{\frac{\hbar E_a^2}{2A\rho\omega_{n,q_{\parallel}}}} \left[(q_{t,n}^2 - q_{\parallel}^2)(q_{l,n}^2 + q_{\parallel}^2) \times \cos\left(\frac{aq_{t,n}}{2}\right) \sin(q_{l,n}z) \right], \quad (11)$$

where A is the area of the slab, ρ is the mass density, and $F_{d,n}(F_{f,n})$ is the normalization constants of the n th eigenmode for the dilatational (flexural) waves. Although the fluctuation of the dot (due to strain, etc.) may affect the spin-orbit and electron-phonon coupling, we, for simplicity, neglect the effect on the scattering rate in this work.

We calculate the spin relaxation rates between the two lowest (spin mixing) states from the Fermi golden rule³⁰

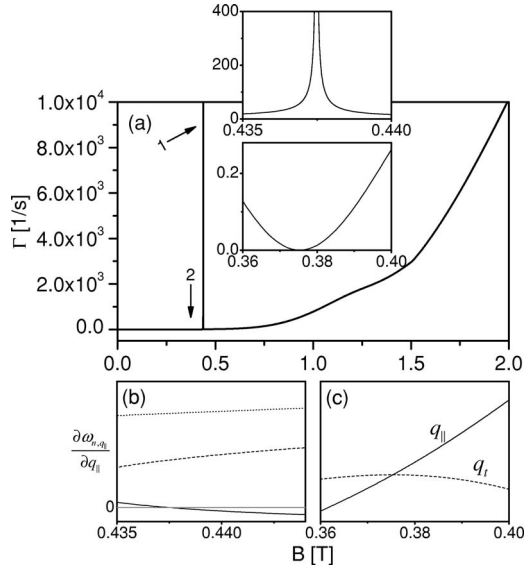


FIG. 2. (a) Spin relaxation rate as a function of magnetic field for the lateral length $l_0=30$ nm, the width $a=130$ nm, and temperature $T=100$ mK. The SO couplings λ_R and λ_D are set equal to 5×10^{-13} and 16×10^{-12} eV m, respectively. The insets further show the enlarged regions of arrow 1 (upper inset) and arrow 2 (lower inset). (b) Three phonon group velocities vs the magnetic field. (c) The values q_{\parallel} and q_t vs the magnetic field.

$$\Gamma = \frac{2\pi}{\hbar} \sum_{\substack{\mathbf{q}_{\parallel,n} \\ \lambda=d,f}} |M_{\lambda}|^2 |\langle f | e^{i\mathbf{q}_{\parallel} \cdot \mathbf{r}_{\parallel}} | i \rangle|^2 (N_{q_{\parallel}} + 1) \delta(\Delta E - \hbar\omega_{n,q_{\parallel}}), \quad (12)$$

where the energy $\Delta E (=E_i - E_f)$ is the energy difference between the first excited $|i\rangle$ and ground $|f\rangle$ states. $N_{q_{\parallel}}$ represents the Bose distribution of the phonon at temperature T . For the sake of simplicity, we consider the QD to be located at $z=0$ so that the function M_f for flexural waves plays no role.

Let us first focus on the dependence of the relaxation rates on the magnetic field B for lateral length $l_0=30$ nm. Unlike the situation in bulk system, an enhanced spin relaxation rate occurs as shown in Fig. 2(a) (arrow 1 in the upper inset). This phenomenon originates from the van Hove singularity that corresponds to a minimum in the dispersion relation $\omega_{n,q_{\parallel}}$ for finite q_{\parallel} . We further plot the phonon group velocity ($\partial\omega_{n,q_{\parallel}}/\partial q_{\parallel}$) as a function of q_{\parallel} around the van Hove singularity as shown in Fig. 2(b). There are three modes contributing to the relaxation rate. In particular, a crossover from positive to negative group velocity is observed for one mode. Because of the zero phonon group velocity, the rate behaves sharply at that magnetic field. However in a real system the van Hove singularity would be cut off or broadened because of the finite phonon lifetime. Contrary to the enhanced rate, we find a suppression of the spin relaxation rate (arrow 2) at small magnetic field (also seen in the lower inset). This comes from a vanishing divergence of the displacement field \mathbf{u} . As can be seen from Eq. (10) in detail, the deformation potential disappears at the condition of $q_{\parallel}=q_t$ [Fig. 2(c)], which causes a zero spin relaxation rate. Note that our results

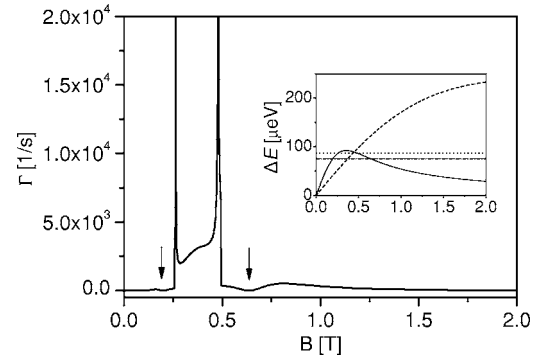


FIG. 3. Spin relaxation rate for the lateral length $l_0=60$ nm, width $a=130$ nm, and temperature $T=100$ mK. The SO couplings λ_R and λ_D are set equal to 5×10^{-13} and 16×10^{-12} eV m, respectively. Two enhanced and suppressed rates (arrow) occur. The inset shows the energy spacing ΔE vs the magnetic field B for different lateral lengths: $l_0=30$ nm (dashed line) and $l_0=60$ nm (solid line). Two horizontal lines in the inset indicate the corresponding energies for the van Hove singularity (dotted line) and the suppression of the rate (dashed-dotted line).

for the van Hove singularity and the disappearance of the deformation potential are consistent with what was found in Ref. 27. Although the phonon model in our work is the same, the dot part is different.

The relaxation rate for larger QDs exhibits a qualitatively different behavior. As shown in Fig. 3, two van Hove singularities appear when varying the magnetic field. In addition, one also finds two suppressions of the relaxation rate (arrow) near the singularities. We have analyzed the energy spacing between the two lowest states in the inset of Fig. 3. For small lateral size, the gap increases monotonically (dashed line). On the contrary, energy spacing for larger QDs shows a quite different feature. The value initially increases as B increases. However, after it reaches a maximum point, the energy spacing decreases with the increasing of the magnetic field B : although the Zeeman splitting increases with increasing magnetic field, the spin-orbit interaction, on the contrary, tends to reduce the energy spacing between the two lowest levels. When the magnetic field is large enough, the spin-orbit effect overwhelms the Zeeman term and results in a decreasing tendency. Therefore, if the magnetic field is increased high enough, the dashed line (small QD) also shows similar behavior. This agrees well with the findings in Ref. 14. From the inset, one recognizes that if the energy spacing exactly matches the specific phonon energy (dotted line), the van Hove singularity will appear. For the case of a large lateral length, there are two van Hove singularities and two suppressions of the relaxation rate (dashed-dotted line).

Figure 4 shows the specific energy spacings where rates are enhanced and suppressed as a function of the width. For the case of small widths, the enhanced rates (black mark) and suppressed rates (red mark) can be clearly distinguished, and their corresponding energy spacings are relative large. With the increasing of the width, the energy spacing between the enhanced and suppressed rates decrease monotonically. One can expect that if the width increases further, the system will approach the bulk system. This means that the van Hove

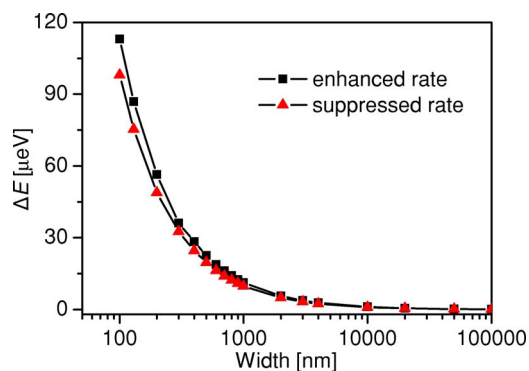


FIG. 4. (Color online) Dependence of the specific energy spacings ΔE for the enhanced (black squares) and suppressed (red triangles) rates on the width a . The lateral length of the QD is 30 nm. The Rashba constant is $\lambda_R = 5 \times 10^{-12}$ eV m and the Dresselhaus constant is $\lambda_D = 16 \times 10^{-12}$ eV m.

singularity and the suppressed rate will be inhibited and eventually disappear.

If one varies the vertical position of the dot, the rate will change due to different contributions from the dilatational and flexural waves. Accordingly, the van Hove singularities resulting from flexural waves will also be altered. For example, the ratio of dilatational to flexural wave's contribution is about 2.8:1 under the condition of $B=1$ T and vertical position $z=25$ nm. However, if ΔE also changes, the contributions from two waves will also change. This is because the parameters ($q_{\parallel}, q_{l,n}, q_{t,n}$) of dilatational and flexural waves independently satisfy the dispersion relations. On the other

hand, comparing the bulk phonons with the confined ones, the phonon-induced rates are roughly similar when varying the magnetic field. However, there are two peculiar characteristics for the confined phonons. One feature is the van Hove singularity which results from a zero group velocity such that an enhanced spin relaxation rate can occur. The second feature is a vanishing divergence of the displacement field. This will cause a suppression of spin relaxation rate, which is an advantage if considering the QD spin as a possible quantum bit candidate.

We have studied the spin relaxation rate in a GaAs quantum dot embedded in a semiconductor slab, where an enhanced rate was found due to the phonon van Hove singularity. We found that at certain magnetic fields one enters a regime with quite the opposite characteristics, where a vanishing divergence of the displacement causes a suppression of spin relaxation rates. For larger dots there are multiple singularities and suppressions in the electron-phonon rates due to the interplay between spin-orbit coupling and Zeeman interaction. We believe our results to be useful for the understanding of spin relaxation in suspended quantum dot nanostructures. Our findings also point at novel effects to be expected from future nanoscale systems where spin and mechanical degrees of freedom are combined.

This work was partially supported by the National Science Council, Taiwan under Grant Nos. NSC 94-2112-M-009-019, NSC 94-2120-M-009-002, and NSC 94-2112-M-009-024.

*Electronic address: dschuu@mail.nctu.edu.tw

¹S. Datta and B. Das, Appl. Phys. Lett. **56**, 665 (1990).

²I. Žutić, J. Fabian, and S. Das Sarma, Phys. Rev. Lett. **88**, 066603 (2002).

³D. Loss and D. P. DiVincenzo, Phys. Rev. A **57**, 120 (1998); G. Burkard, D. Loss, and D. P. DiVincenzo, Phys. Rev. B **59**, 2070 (1999).

⁴X. Hu and S. Das Sarma, Phys. Rev. A **61**, 062301 (2000).

⁵M. Friesen, P. Rugheimer, D. E. Savage, M. G. Lagally, D. W. van der Weide, R. Joynt, and M. A. Eriksson, Phys. Rev. B **67**, 121301(R) (2003).

⁶S. M. Reimann and M. Manninen, Rev. Mod. Phys. **74**, 1283 (2002).

⁷W. G. van der Wiel, S. De Franceschi, J. M. Elzerman, T. Fujisawa, S. Tarucha, and L. P. Kouwenhoven, Rev. Mod. Phys. **75**, 1 (2003).

⁸G. Dresselhaus, Phys. Rev. **100**, 580 (1955).

⁹M. I. D'yakonov and V. I. Perel', Zh. Eksp. Teor. Fiz. **60**, 1954 (1971) [Sov. Phys. JETP **38**, 1053 (1971)].

¹⁰M. I. D'yakonov and V. Yu. Kachorovskii, Fiz. Tekh. Poluprovodn. (S.-Peterburg) **20**, 178 (1986) [Sov. Phys. Semicond. **20**, 110 (1986)].

¹¹Yu. L. Bychkov and E. I. Rashba, JETP Lett. **39**, 78 (1984); J. Phys. C **17**, 6039 (1984).

¹²O. Voskoboynikov, C. P. Lee, and O. Tretyak, Phys. Rev. B **63**,

165306 (2001).

¹³C. F. Destefani, S. E. Ulloa, and G. E. Marques, Phys. Rev. B **70**, 205315 (2004).

¹⁴C. F. Destefani and S. E. Ulloa, Phys. Rev. B **71**, 161303(R) (2005).

¹⁵S. DeBald and C. Emary, Phys. Rev. Lett. **94**, 226803 (2005).

¹⁶T. Fujisawa, D. G. Austing, Y. Tokura, Y. Hirayama, and S. Tarucha, Nature (London) **419**, 278 (2002).

¹⁷R. Hanson, B. Witkamp, L. M. K. Vandersypen, L. H. Willems van Beveren, J. M. Elzerman, and L. P. Kouwenhoven, Phys. Rev. Lett. **91**, 196802 (2003).

¹⁸J. M. Elzerman, R. Hanson, L. H. Willems van Beveren, B. Witkamp, L. M. K. Vandersypen, and L. P. Kouwenhoven, Nature (London) **430**, 431 (2004).

¹⁹A. V. Khaetskii and Y. V. Nazarov, Phys. Rev. B **61**, 12639 (2000); **64**, 125316 (2001).

²⁰L. M. Woods, T. L. Reinecke, and Y. Lyanda-Geller, Phys. Rev. B **66**, 161318(R) (2002).

²¹R. de Sousa and S. Das Sarma, Phys. Rev. B **68**, 155330 (2003).

²²V. N. Golovach, A. Khaetskii, and D. Loss, Phys. Rev. Lett. **93**, 016601 (2004).

²³J. L. Cheng, M. W. Wu, and C. Lü, Phys. Rev. B **69**, 115318 (2004).

²⁴D. V. Bulaev and D. Loss, Phys. Rev. B **71**, 205324 (2005).

²⁵N. Bannov, V. Aristov, V. Mitin, and M. A. Strosio, Phys. Rev. B

- 51**, 9930 (1995); N. Bannov, V. Mitin, and M. A. Stroschio, Phys. Status Solidi B **183**, 131 (1994).
- ²⁶B. A. Glavin, V. I. Pipa, V. V. Mitin, and M. A. Stroschio, Phys. Rev. B **65**, 205315 (2002).
- ²⁷S. Debal, T. Brandes, and B. Kramer, Phys. Rev. B **66**, 041301(R) (2002).
- ²⁸E. M. Höhberger, T. Krämer, W. Wegscheider, and R. H. Blick, Appl. Phys. Lett. **82**, 4160 (2003).
- ²⁹E. M. Weig, R. H. Blick, T. Brandes, J. Kirschbaum, W. Wegscheider, M. Bichler, and J. P. Kotthaus, Phys. Rev. Lett. **92**, 046804 (2004).
- ³⁰The parameters for the GaAs QD: $m=0.067m_0$, $g^*=-0.44$, $E_a=6.7$ eV, $\rho=5.3 \times 10^3$ Kg/m³, $c_l=3.35 \times 10^3$ m/s, $c_t=5.7 \times 10^3$ m/s.

Orientation of adsorbed dipolar molecules: A conical well model

Y. Y. Liao, Y. N. Chen, W. C. Chou, and D. S. Chuu*

Department of Electrophysics, National Chiao-Tung University, Hsinchu 300, Taiwan

(Received 14 July 2005; revised manuscript received 8 December 2005; published 21 March 2006)

Orientation of single and two coupled polar molecules irradiated by a single laser pulse under a conical-well model is investigated theoretically. The orientation of a single hindered rotor shows a periodic behavior. In particular, the amplitude of the oscillation is sensitive to the degree of alternation of the laser field. Crossover from field-free to hindered rotation is observed by varying the hindering angle for different heights of conical wells. For a small hindering potential and angle, time-averaged orientation differs greatly from that for an infinite one. The orientation at a large hindering angle shows irregularlike behavior under strong dipole-dipole interaction. Entanglement induced by the dipole-dipole interaction is also calculated for the coupled-rotor system, in which the time-averaged entropy increases monotonically as the hindering angle is increased. The competition between the confinement effect and dipole interaction is found to dominate the behavior of the coupled-rotor system.

DOI: [10.1103/PhysRevB.73.115421](https://doi.org/10.1103/PhysRevB.73.115421)

PACS number(s): 73.20.Hb, 33.20.Sn, 33.80.-b

Controlling the orientation of molecules has wide applications from stereodynamics to surface catalysis, molecular focusing, and nanoscale design.¹ The molecular alignment is responsible for the anisotropic polarizability induced by the nonresonant laser pulses. For adiabatic regime, the crucial characteristic is that the duration of the laser pulse is longer than the rotational period. The pendular states can be created adiabatically, and the molecular axis is aligned parallel to the direction of the field polarization. As the laser pulse is switched off, the molecule will go back to its initial condition and no longer be observed again.^{2,3} If the duration of the laser pulse is shorter than the rotational period, the alignment occurs periodically in time, i.e., the nonadiabatic regime.^{4,5} On the other hand, a field-free orientation can be generated by a femtosecond laser pulse.^{6,7} The dipole molecule will tend to orient by applying a highly asymmetrical pulse. It is found that a pronounced orientation can still persist after switching off of the pulse.

In addition to the rotation of a free rotor, the rotational motion of molecules adsorbed on a solid surface has attracted increasing interest. To understand the rotational behavior of adsorbed molecules, one can apply the UV laser beam along the surface direction to desorb the molecules. The rotational states can be determined by the quadrupole, which is a measure of the rotational alignment.⁸⁻¹⁰ On the theoretical side, an infinite-conical-well model has been proposed. It was found that the adsorbed molecule is only allowed to rotate within the well region.¹¹ In our earlier works, we have generalized the infinite-well model to a more realistic case of finite-conical well.^{12,13} It was found that there exists the avoided crossing between two adjacent rotational energies when varying the strength of the external field. Our theoretical calculation of the quadrupole moment based on the finite-conical-well model is in agreement with the experimental data.¹⁴

Recently, great attention has been focused on the coupled-rotor system since peculiar behaviors may occur in the presence of dipole-dipole interaction.¹⁵⁻¹⁷ For example, recent neutron scattering experiments on certain Hofmann clathrates have reported the temperature-dependent behavior of

the linewidths.¹⁸ A line broadening mechanism based on rotor-rotor coupling was proposed for the explanation of the widths.¹⁹ With the advances of nanotechnology, one can now investigate the quantum rotors which are mounted on the surfaces.^{20,21} From the laser spectroscopy, two individual fluorescent molecules separated by several nanometers can be resolved on the surface.²² The coherent interactions between the dipole moments associated with their optical transitions are found in the quantum optical measurements. The strong dipole-dipole coupling produces entangled subradiant and superradiant states in the two-molecule-system under laser radiation.

Even though the orientation of the free molecule is well studied, investigations on the rotation of the adsorbed molecule confined the surface potential are still lacking.²³ In the complex surface system, the adsorbed molecules are no longer isolated. Several studies have shown that interesting phenomena can occur due to the existence of dipole-dipole interaction. Besides, although the entangled behavior of two coupled rotors was also investigated recently, these works are limited in the model of kicked tops.^{24,25} However, the dynamical entanglement via the rotations of the adsorbed molecules remains mostly unexplored. In particular, a molecular system evolves from a nonentangled case to an entangled one. According to our previous study,¹⁷ it is found that the orientations of the coupled rotors relate closely to the entropy. This means that the orientations of the coupled rotors somehow reflect the entropy of the system and thus relates to the measurement of the entanglement. Since the measurement of the entanglement is one of the fundamental important issues in quantum information research, therefore, the study of the entanglement and its measurement is one of the interested problems. Moreover, from the experimental point of view, it is not clear how to keep two free rotors with a fixed distance. Therefore, this makes it more interesting to consider a more realistic system and discuss the corresponding entanglement dynamics.

In this paper, we first investigate the rotational motions of a polar diatomic molecule confined by a hindering conical well. After applying a single strong laser pulse, the hindered

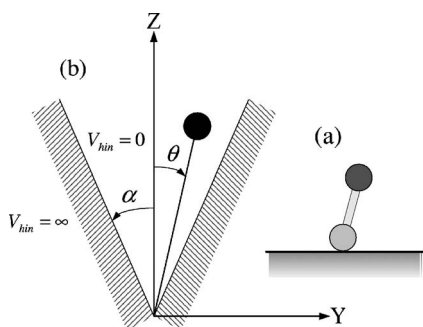


FIG. 1. (a) Schematic view of a single hindered rotor adsorbed on the surface. (b) The corresponding infinite-conical-well model.

rotor shows a periodic behavior. Different signatures between the finite-conical-well and infinite-conical-well model on orientations are pointed out. Besides, the amplitudes of the oscillations are varied by applying different widths of the pulse. Furthermore, we also consider two coupled identical polar molecules adsorbed on the surface with the dipole-dipole interaction and a simultaneously ultrashort laser pulse shined upon them. It is found that both the entanglement (the von Neumann entropy) and orientation show interesting behaviors.

Consider now a dipolar molecule (e.g., NaI) adsorbed on the surface. The rotation of the molecule is confined by the surface potential as shown in Fig. 1. An off-resonant laser field polarized in the z direction interacts with the hindered rotor. Because the laser frequency is much lower than the frequencies of the lowest vibrational and electronic transition, only the rotational excitations can occur in our model. The excitations can be viewed as two photon transitions between two different rotational states through a high intermediate virtual state.⁵ The Hamiltonian without the field-molecule interaction can be written as

$$H_0 = BJ^2 + V_{hin}(\theta, \phi), \quad (1)$$

where B and J^2 are the rotational constant and angular momentum. V_{hin} denotes the surface potential and confines the rotation of adsorbed molecule. For simplicity, the infinite-conical-well model $V_{hin}(\theta, \phi)$ is considered here. According to the previous studies, its dependence on ϕ is weaker than that on θ .^{26–28} We reasonably assume that the surface potential is independent of ϕ . Therefore, in the vertical adsorbed configuration, the surface potential can be written as¹¹

$$V_{hin}(\theta) = \begin{cases} 0, & 0 \leq \theta \leq \alpha \\ \infty, & \alpha < \theta \leq \pi \end{cases}, \quad (2)$$

where α is the hindering angle of the conical well.

The Hamiltonian concerning the field-molecule interaction can be written as

$$H_d = -\mu E(t) \cos \theta, \quad (3)$$

$$H_{ind} = -\frac{1}{2} E^2(t) [(\alpha_{\parallel} - \alpha_{\perp}) \cos^2 \theta + \alpha_{\perp}]. \quad (4)$$

The first term H_d describes a permanent dipole moment μ coupling with an external field, and θ is the angle

between the molecular axis and the field. In this work we choose a Gaussian pulse for our calculation, i.e., $E(t) = E_0 e^{-(t-t_0)^2/\sigma^2} \cos(2\pi\nu t)$, where E_0 is the field strength and ν is the laser frequency. The pulse is centered at the time t_0 , and σ is the pulse duration. The second term H_{ind} is a higher order interaction, in which the external field couples with the induced molecular polarization. The component of the polarizability $\alpha_{\parallel}(\alpha_{\perp})$ is parallel (perpendicular) to the molecular axis. According to our parameters, the field-dipole-moment interaction H_d is much greater than that of the field-induced-dipole-moment interaction H_{ind} in our model. This is because the strength of electric field used here is insufficient to enhance the higher order term. Actually the interaction H_{ind} can play an important role in the case of high strength of electric field.⁵ Therefore, the term (H_{ind}) can be neglected reasonably based on our parameters.

Before solving the time-dependent Schrödinger equation ($H_0 + H_d$), the eigenfunctions of the system [$H_0 = BJ^2 + V_{hin}(\theta)$] must be introduced first. Following Ref. 11, the eigenfunctions can be written as

$$\psi_{lm}(\theta, \phi) = \begin{cases} A_{lm} P_{\nu_{lm}}^{lm}(\cos \theta) \frac{\exp(im\phi)}{\sqrt{2\pi}}, & 0 \leq \theta \leq \alpha \\ 0, & \alpha < \theta \leq \pi \end{cases}, \quad (5)$$

where A_{lm} is the normalization constant and $P_{\nu_{lm}}^{lm}$ is the associated Legendre function of arbitrary order with the corresponding quantum number (l, m). In the above equations, the molecular rotational energy can be expressed as

$$\epsilon_{lm} = \nu_{lm}(\nu_{lm} + 1)B. \quad (6)$$

In order to determine ν_{lm} , one has to match the boundary condition

$$P_{\nu_{lm}}^{lm}(\cos \alpha) = 0. \quad (7)$$

To solve the time-dependent Schrödinger equation, the wave function is expressed in terms of a series of eigenfunctions

$$\Psi(t) = \sum_l c_{lm}(t) \psi_{lm}(\theta, \phi), \quad (8)$$

where $c_{lm}(t)$ is the time-dependent coefficient. The coefficient $c_{lm}(t)$ can be obtained from the different equations

$$i\hbar \dot{c}_{lm}(t) = c_{lm}(t) \epsilon_{lm} + \sum_{l'm'} c_{l'm'}(t) \langle \psi_{lm} | H_d | \psi_{l'm'} \rangle. \quad (9)$$

After determining the coefficients $c_{lm}(t)$, the orientation $\langle \cos \theta \rangle$ can be carried out immediately. We choose NaI as our model molecule, whose dipole moment $\mu = 9.2$ D and rotational constant $B = 0.12$ cm⁻¹. For simplicity (zero-temperature case), the rotor is assumed in the ground state initially, i.e., $c_{00}(t=0) = 1$. The field strength is 3×10^7 V/m and the laser frequency is about 9×10^{11} s⁻¹. The duration and center of the pulse are set equal to 279 and 1200 fs. The main feature is that the ratio in magnitude of the positive and negative peak value of this pulse is 5:1. Unless specified, the parameters of laser field are fixed throughout the paper.

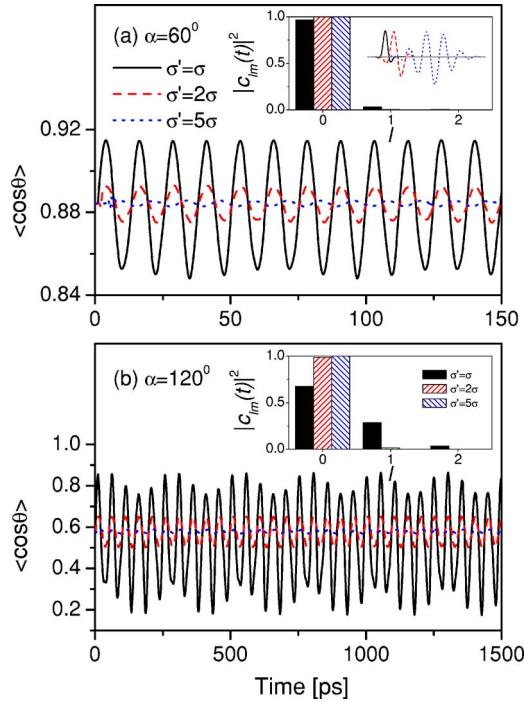


FIG. 2. (Color online) The orientation $\langle \cos \theta \rangle$ as a function of time for different hindering angle α and pulse duration σ' . The insets show the corresponding populations of the states ($l, m=0$) for (a) $\alpha=60^\circ$ and (b) $\alpha=120^\circ$, respectively. The corresponding laser fields are shown in the upper inset.

Figure 2 illustrates the orientation $\langle \cos \theta \rangle$ as a function of time for different hindering angles and pulse durations. In both cases, the orientations display periodiclike behavior. For the pulse duration ($\sigma' = \sigma$), the orientation of small hindering angle ($\alpha=60^\circ$) shows a relative large value but with small oscillatory amplitude, while for $\alpha=120^\circ$ a large oscillatory amplitude with multifrequency (insets of Fig. 2) is obtained. Obviously, such a difference comes from the quantum confinement effect. We further apply the laser pulses with different widths by tuning the duration and center. If the pulse duration increases, the amplitudes of the oscillations decrease and the orientations approach the initial value as shown in the insets. The reason is that the mean orientation is suppressed by the alternations of the electromagnetic field, i.e., the cancellation of negative and positive orientations.

To see more clearly the effect of the hindering potential, let us now consider the finite potential model

$$V_{hin}(\theta) = \begin{cases} 0, & 0 \leq \theta \leq \alpha \\ V_0, & \alpha < \theta \leq \pi \end{cases} \quad (10)$$

where V_0 is the height of well. Following Refs. 12–14, the rotational energy and eigenfunctions can be determined by matching appropriate boundary condition. Figure 3 shows the time-averaged orientation as a function of time for different hindering potentials. For infinite potential ($V_0=\infty$), the time-averaged orientation decreases monotonically from 1 to 0 as the hindering angle is increased. However, if the well is finite, the time-averaged orientation has a maximum point at certain angle. This means if the open angle α decreases fur-

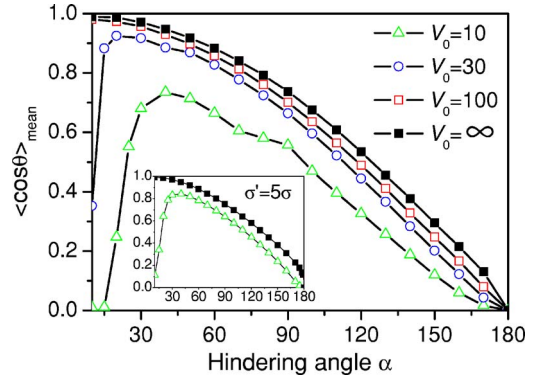


FIG. 3. (Color online) The mean orientation $\langle \cos \theta \rangle_{\text{mean}}$ as a function of hindering angle for fixed pulse duration ($\sigma' = \sigma$) and different conical-well potentials $V_0 = 10, 30, 100$. The inset shows the mean orientation $\langle \cos \theta \rangle_{\text{mean}}$ in the case of $V_0 = 10$ and ∞ by applying a pulse of $\sigma' = 5\sigma$. The potential V_0 is in units of the rotational constant B .

ther, the contribution from the penetrated wave function overwhelms the impenetrable one, rendering the decreasing of the time-averaged orientation. We also compare the case of $\sigma' = \sigma$ with that of $\sigma' = 5\sigma$ (inset of Fig. 3). It is found that, for larger duration $\sigma' = 5\sigma$, although the oscillatory amplitude is smaller (Fig. 2), the value of time-averaged orientation is larger comparing to the case of $\sigma' = \sigma$.

As we mentioned above, the spatial resolution of two individual molecules hindered on a surface in tens of nanometers is now possible.^{20–22} We further consider that two identical dipolar molecules (separated by a distance of R , R is in an order of magnitude of 10^{-8} m) confined by the hindering wells. The molecules are assumed to interact with each other via dipole-dipole interaction only. A polarized laser pulse is applied to interact with both molecules. The Hamiltonian of the coupled system can be written as

$$H_c = \sum_{j=1,2} H_{0,j} + U_{dip} + H_I, \quad (11)$$

where $H_{0,j}$ is the Hamiltonian of single hindered rotor without the laser-dipole interaction. The dipole interaction between two dipole moments μ_1 and μ_2 is

$$\begin{aligned} U_{dip} &= [\vec{\mu}_1 \cdot \vec{\mu}_2 - 3(\vec{\mu}_1 \cdot \hat{e}_R)(\vec{\mu}_2 \cdot \hat{e}_R)]/R^3 \\ &= \mu_1 \mu_2 (\sin \theta_1 \cos \phi_1 \sin \theta_2 \cos \phi_2 + \cos \theta_1 \cos \theta_2 \\ &\quad - 2 \sin \theta_1 \sin \phi_1 \sin \theta_2 \sin \phi_2)/R^3, \end{aligned} \quad (12)$$

where $\hat{e}_R (= \vec{R}/R)$ is assumed to be in the y direction, and (θ_1, ϕ_1) and (θ_2, ϕ_2) are the coordinates of first and second molecule, respectively. For simplicity, we assume the dipole moments of two molecules are identical, i.e., $\mu_1 = \mu_2 = \mu$. One might argue that the higher order terms may also contribute to the results. According to previous study,¹⁵ the next higher order term is about the order of r^3/R^4 with bond length r . If one compares the dipole-dipole interaction, $[O(r^2/R^3)]$, with the next higher order effect [the bond length $r = 2.7 \text{ \AA}$ (Ref. 29) and separation $R = 15 \text{ nm}$], it is found that the contribution from the next higher-order term is only 2%

of the dipole-dipole interaction. Therefore, it is reasonable to include only the dipole interaction in our model. The field-molecule coupling H_I can then be expressed as

$$H_I = -\mu E(t) \cos \theta_1 \cos(\omega t) - \mu E(t) \cos \theta_2 \cos(\omega t), \quad (13)$$

where θ_1 and θ_2 are the angles between dipole moments and laser field. In the above equations, the time-dependent Schrödinger equation can be solved by expanding the wave function in terms of a series of eigenfunctions

$$|\Psi_c\rangle = \sum_{l_1 m_1 l_2 m_2} c_{l_1 m_1 l_2 m_2}(t) \psi_{l_1 m_1}(\theta_1, \phi_1) \psi_{l_2 m_2}(\theta_2, \phi_2), \quad (14)$$

where (θ_1, ϕ_1) and (θ_2, ϕ_2) are the coordinates for two molecules. $c_{l_1 m_1 l_2 m_2}(t)$ are the time-dependent coefficients corresponding to the quantum numbers $(l_1, m_1; l_2, m_2)$, and can be determined by solving Schrödinger equations numerically. The initial state is set as $|\psi_{00}\psi_{00}\rangle$ [$c_{0000}(t=0)=1$].

In addition to the orientation, one can also analyze the entanglement induced by the dipole interaction. The wave function of the coupled molecules can be expressed as a pure bipartite system [a compact form of Eq. (14)]: $|\Psi_c\rangle = \sum_{l_1 m_1 l_2 m_2} c_{l_1 m_1 l_2 m_2}(t) |\psi_{l_1 m_1}\rangle |\psi_{l_2 m_2}\rangle$. The reduced density operator for the first molecule is defined as

$$\rho_{\text{mol } 1} = \text{Tr}_{\text{mol } 2} |\Psi_c\rangle \langle \Psi_c|. \quad (15)$$

To obtain the entanglement of entropy, the bases of molecule 1 is transformed to make the reduced density matrix $\rho_{\text{mol } 1}$ to be diagonal. The entangled state can be represented by a biorthogonal expression with positive real coefficients λ_{lm} . The degree of entanglement for the coupled molecules can be measured by von Neumann entropy^{30,31}

$$\text{Entropy} = - \sum_{lm} \lambda_{lm} \log_n \lambda_{lm}. \quad (16)$$

Figure 4 shows the entropy and orientation evolves with time for fixed angle $\alpha=120^\circ$ and interdistance $R=1.5 \times 10^{-8}$ m. Because of the presence of the laser pulse, contributions to the energy exchange between two molecules come from many excited states, resulting in an irregularlike behavior of the entropy shown in Fig. 4(a). Further analysis of the dynamics gives the fact that the entropy grows monotonically from zero to a certain finite value. This is because the laser pulse dominates at the initial stage. The strength of the laser pulse is much larger than that of the dipole-dipole interaction. In addition, the duration is much shorter than the characteristic time of the dipole interaction. After the laser pulse, populations to the (rotational) excited states are formed (inset). The nonlinear dipole interaction then initiates the exchange process between the states until certain ‘‘dynamical equilibrium’’ is reached. One can conclude that the nonlinear variations of populations confirm the feature shown in the inset. Moreover, the orientations of the coupled molecules are also displayed in Fig. 4(b). Compared to the single molecule case, the irregular behavior is certainly from the nonlinear dipole interaction.

Figure 5 shows the time-averaged entropy for different hindering angles. As the hindering angle increases, the time-

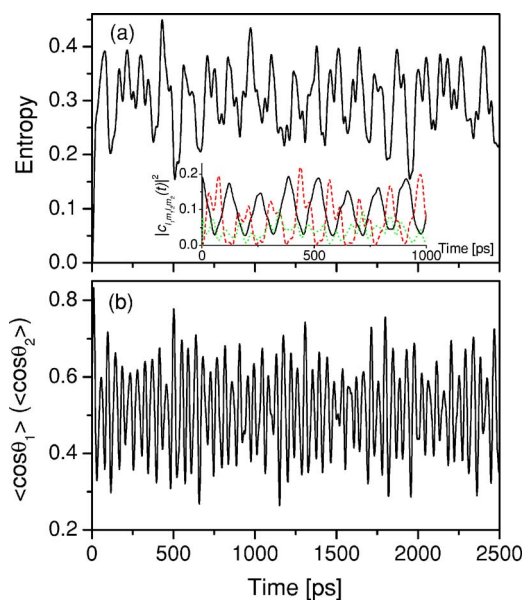


FIG. 4. (Color online) The entropy (a) and orientations $\langle \cos \theta_1 \rangle$ ($\langle \cos \theta_2 \rangle$) (b) in an infinite conical well for a fixed angle $\alpha=120^\circ$ and interdistance $R=1.5 \times 10^{-8}$ m. The inset shows the populations $|c_{l_1 m_1 l_2 m_2}(t)|^2$ irregularly oscillate with time, corresponding to the quantum number $(l_1, m_1; l_2, m_2) = (1, 0; 0, 0)$ (black solid curve), $(1, 1; 0, 0)$ (red dashed curve), and $(1, 0; 1, 0)$ (green dotted curve), respectively. Although we only focus on several excited states here, the populations of most states similarly remain irregular behavior.

averaged entropy increases monotonically. This is because for larger angles more excited states can be obtained under the same strength of the laser pulse, resulting in larger entropy. Note that the magnitude of orientation is high as the hindering angle is set equal to 30° (inset of Fig. 5). This again verifies that the narrow potential restricts the motion of the hindered rotor. In this case, the dipole interaction is suppressed, causing the regularlike behavior of the orientation. On the contrary, more excitations are populated such that the orientation oscillates with irregularity at $\alpha=150^\circ$.

A few remarks about the experimental verifications of our model should be addressed here. According to our previous

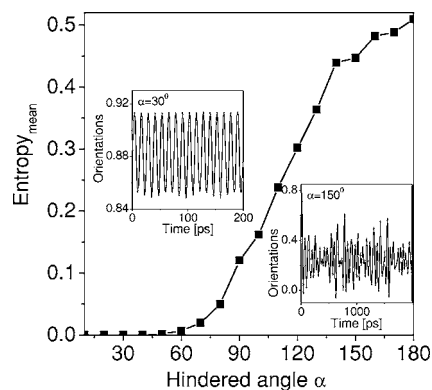


FIG. 5. The time-averaged entropy as a function of the hindered angle in the infinite conical well. The insets show the orientations of two molecules for hindered angles $\alpha=30^\circ$ and $\alpha=150^\circ$, respectively. The intermolecule separation is $R=1.5 \times 10^{-8}$ m.

study¹⁷ and this work, it is found that the orientations of the coupled rotors relate closely to the entropy. This indicates that the orientations of the coupled rotors somehow reflect the entropy of the system. For the measurement of orientation many experiments have been performed. For example, the Coulomb explosion of the molecules using intense femtosecond probe laser pulses and a time-of-flight mass spectrometer.³²⁻³⁴ The degree of orientation is determined by the measurement of fragment ions. Under proper arrangements, the orientation of hindered rotors can also be measured by similar technologies. This may provide some indication of the entanglement.

In summary, we have studied the dynamics of the adsorbed polar molecules under the irradiation of a single laser pulse. It is found that the orientation of a single hindered

rotor shows a periodic behavior. In particular, the amplitude of oscillation is sensitive to the degree of alternation of the laser field. On the other hand, the orientation of the coupled rotors shows irregular behavior because of the dipole-dipole interaction. Comparisons between the infinite-well and finite-well models are made, and the differences are both shown explicitly in the orientations and entanglement of entropy. These findings contribute to the essential physics of coupled rotors and may be useful in the field of surface science.

This work is supported partially by the National Science Council, Taiwan under Grants Nos. NSC 94-2112-M-009-024, NSC 94-2120-M-009-002, and NSC 94-2112-M-009-019.

*Corresponding author. Electronic address: dschuu@mail.nctu.edu.tw

- ¹H. Stapelfeldt and T. Seideman, *Rev. Mod. Phys.* **75**, 543 (2003).
- ²B. Friedrich and D. Herschbach, *Phys. Rev. Lett.* **74**, 4623 (1995).
- ³L. Cai, J. Marango, and B. Friedrich, *Phys. Rev. Lett.* **86**, 775 (2001).
- ⁴J. Ortigoso, M. Rodriguez, M. Gupta, and B. Friedrich, *J. Chem. Phys.* **110**, 3870 (1999).
- ⁵M. Machholm, *J. Chem. Phys.* **115**, 10724 (2001).
- ⁶M. Machholm and N. E. Henriksen, *Phys. Rev. Lett.* **87**, 193001 (2001).
- ⁷C. M. Dion, A. B. Haj-Yedder, E. Cancès, C. Le Bris, A. Keller, and O. Atabek, *Phys. Rev. A* **65**, 063408 (2002).
- ⁸I. Beauport, K. Al-Shamery, and H.-J. Freund, *Chem. Phys. Lett.* **256**, 641 (1996).
- ⁹S. Thiel, M. Pykavy, T. Klüner, H.-J. Freund, R. Kosloff, and V. Staemmler, *Phys. Rev. Lett.* **87**, 077601 (2001).
- ¹⁰S. Thiel, M. Pykavy, T. Klüner, H.-J. Freund, R. Kosloff, and V. Staemmler, *J. Chem. Phys.* **116**, 762 (2002).
- ¹¹J. W. Gadzuk, U. Landman, E. J. Kuster, C. L. Cleveland, and R. N. Barnett, *Phys. Rev. Lett.* **49**, 426 (1982).
- ¹²Y. T. Shih, D. S. Chuu, and W. N. Mei, *Phys. Rev. B* **51**, 14626 (1995).
- ¹³Y. T. Shih, D. S. Chuu, and W. N. Mei, *Phys. Rev. B* **54**, 10938 (1996).
- ¹⁴Y. T. Shih, Y. Y. Liao, and D. S. Chuu, *Phys. Rev. B* **68**, 075402 (2003).
- ¹⁵H. Shima and T. Nakayama, *Phys. Rev. B* **69**, 035202 (2004).
- ¹⁶H. Shima and T. Nakayama, *Phys. Rev. A* **70**, 013401 (2004).
- ¹⁷Y. Y. Liao, Y. N. Chen, and D. S. Chuu, *Chem. Phys. Lett.* **398**,

418 (2004).

- ¹⁸O. Rogalsky, P. Vorderwisch, A. Huller, and S. Hautecler, *J. Chem. Phys.* **116**, 1063 (2002).
- ¹⁹A. Würger, *Phys. Rev. Lett.* **88**, 063002 (2002).
- ²⁰S. Yasutomi, T. Morita, Y. Imanishi, and S. Kimura, *Science* **304**, 1944 (2004).
- ²¹W. Ho, *J. Chem. Phys.* **117**, 11033 (2002).
- ²²C. Hettich, C. Schmitt, J. Zitzmann, S. Kuhn, I. Gerhardt, and V. Sandoghdar, *Science* **298**, 385 (2002).
- ²³Y. Y. Liao, Y. N. Chen, and D. S. Chuu, *Phys. Rev. B* **70**, 233410 (2004).
- ²⁴P. A. Miller and S. Sarkar, *Phys. Rev. E* **60**, 1542 (1999).
- ²⁵H. Fujisaki, T. Miyadera, and A. Tanaka, *Phys. Rev. E* **67**, 066201 (2003).
- ²⁶R. P. Pan, R. D. Eters, K. Kobashi, and V. Chandrasekharan, *J. Chem. Phys.* **77**, 1035 (1982).
- ²⁷J. W. Riehl and C. J. Fisher, *J. Chem. Phys.* **59**, 4336 (1973).
- ²⁸V. M. Allen and P. D. Pacey, *Surf. Sci.* **177**, 36 (1986).
- ²⁹See, for instance, *Handbook of Chemistry and Physics*, 84th ed., edited by D. R. Lide (The Chemical Rubber Company, Boca Raton, 2003).
- ³⁰C. H. Bennett, H. J. Bernstein, S. Popescu, and B. Schumacher, *Phys. Rev. A* **53**, 2046 (1996).
- ³¹S. Parker, S. Bose, and M. B. Plenio, *Phys. Rev. A* **61**, 032305 (2000).
- ³²H. Sakai, S. Minemoto, H. Nanjo, H. Tanji, and T. Suzuki, *Phys. Rev. Lett.* **90**, 083001 (2003).
- ³³S. Minemoto, H. Nanjo, H. Tanji, T. Suzuki, and H. Sakai, *J. Chem. Phys.* **118**, 4052 (2003).
- ³⁴H. Sakai, S. Minemoto, H. Nanjo, H. Tanji, and T. Suzuki, *Eur. Phys. J. D* **26**, 33 (2003).

Current noise of a quantum dot $p-i-n$ junction in a photonic crystal

Y. N. Chen,¹ D. S. Chuu,¹ and T. Brandes²

¹*Department of Electrophysics, National Chiao-Tung University, Hsinchu 300, Taiwan*

²*School of Physics and Astronomy, The University of Manchester, P.O. Box 88, Manchester, M60 1QD, United Kingdom*

(Received 18 August 2005; published 26 October 2005)

The shot-noise spectrum of a quantum dot $p-i-n$ junction embedded inside a three-dimensional photonic crystal is investigated. Radiative decay properties of quantum dot excitons can be obtained from the observation of the current noise. The characteristic of the photonic band gap is revealed in the current noise with discontinuous behavior. Applications of such a device in entanglement generation and emission of single photons are pointed out, and may be achieved with current technologies.

DOI: [10.1103/PhysRevB.72.153312](https://doi.org/10.1103/PhysRevB.72.153312)

PACS number(s): 73.63.-b, 73.50.Td, 71.35.-y, 42.70.Qs

Since Yablonovitch proposed the idea of photonic crystals (PCs),¹ optical properties in periodic dielectric structures have been investigated intensively.² Great attention has been focused on these materials not only because of their potential applications in optical devices, but also because of their ability to drastically alter the nature of the propagation of light from a fundamental perspective.³ Among these, modification of spontaneous emission is of particular interest. Historically, the idea of controlling the spontaneous emission rate was proposed by Purcell,⁴ and enhanced and inhibited spontaneous emission rates for atomic systems were intensively investigated in the 1980s (Ref. 5) by using atoms passed through a cavity. In semiconductor systems, the electron-hole pair is naturally a candidate to examine spontaneous emission, where modifications of the spontaneous emission rates of quantum dot (QD) (Ref. 6) or quantum wire (QW) (Ref. 7) excitons inside the microcavities have been observed experimentally.

Recently, the interest in measurements of shot noise in quantum transport has risen owing to the possibility of extracting valuable information not available in conventional dc transport experiments.⁸ With the advances of fabrication technologies, it is now possible to embed QDs inside a $p-i-n$ structure,⁹ such that the electron and hole can be injected separately from opposite sides. This allows one to examine the exciton dynamics in a QD via electrical currents.¹⁰ On the other hand, it is also possible to embed semiconductor QDs in PCs,¹¹ where modified spontaneous emission of QD excitons is observed over large frequency bandwidths.

In this work, we present nonequilibrium calculations for the quantum noise properties of quantum dot excitons inside photonic crystals. We obtain the current noise of QD excitons via the MacDonald formula,¹² and find that it reveals many of the characteristics of the photonic band gap (PBG). Possible applications of such a device to the generation of entangled states and the emission of single photons are also pointed out.

Model. We assume that a QD $p-i-n$ junction is embedded in a three-dimensional PC. A possible structure is shown in Fig. 1. Both the hole and electron reservoirs are assumed to be in thermal equilibrium. For the physical phenomena we are interested in, the Fermi level of the $p(n)$ -side hole (electron) is slightly lower (higher) than the hole (electron) sub-

band in the dot. After a hole is injected into the hole subband in the QD, the n -side electron can tunnel into the exciton level because of the Coulomb interaction between the electron and hole. Thus, we may introduce the three dot states: $|0\rangle=|0,h\rangle$, $|\uparrow\rangle=|e,h\rangle$, and $|\downarrow\rangle=|0,0\rangle$, where $|0,h\rangle$ means there is one hole in the QD, $|e,h\rangle$ is the exciton state, and $|0,0\rangle$ represents the ground state with no hole and electron in the QD. One might argue that one cannot neglect the state $|e,0\rangle$ for real devices since the tunable variable is the applied voltage. This can be resolved by fabricating a thicker barrier on the electron side so that there is little chance for an electron to tunnel in advance.¹³ Moreover, the charged exciton and biexcitons states are also neglected in our calculations, which means a low injection limit is required.¹⁴

Derivation of Master equation. We define the dot-operators $\hat{n}_\uparrow \equiv |\uparrow\rangle\langle\uparrow|$, $\hat{n}_\downarrow \equiv |\downarrow\rangle\langle\downarrow|$, $\hat{p} \equiv |\uparrow\rangle\langle\downarrow|$, $\hat{s}_\uparrow \equiv |0\rangle\langle\uparrow|$, \hat{s}_\downarrow

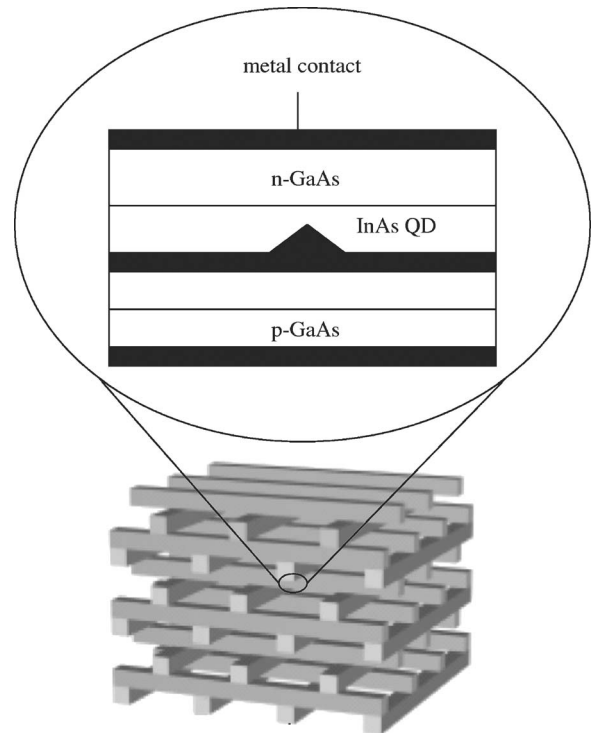


FIG. 1. Illustration of a QD inside a $p-i-n$ junction surrounded by a three-dimensional PC.

$\equiv |0\rangle\langle\downarrow|$. The total Hamiltonian H of the system consists of three parts: H_0 [dot, photon bath H_p , and the electron (hole) reservoirs H_{res}], H_T (dot-photon coupling), and the dot-reservoir coupling H_V

$$H = H_0 + H_T + H_V,$$

$$H_0 = \varepsilon_\uparrow \hat{n}_\uparrow + \varepsilon_\downarrow \hat{n}_\downarrow + H_p + H_{\text{res}},$$

$$H_T = \sum_k D_k b_k^\dagger \hat{p} + D_k^* b_k \hat{p}^\dagger = \hat{p} X + \hat{p}^\dagger X^\dagger,$$

$$H_p = \sum_k \omega_k b_k^\dagger b_k$$

$$H_V = \sum_{\mathbf{q}} (V_{\mathbf{q}} c_{\mathbf{q}}^\dagger \hat{s}_\uparrow + W_{\mathbf{q}} d_{\mathbf{q}}^\dagger \hat{s}_\downarrow + \text{c.c.}),$$

$$H_{\text{res}} = \sum_{\mathbf{q}} \varepsilon_{\mathbf{q}}^\uparrow c_{\mathbf{q}}^\dagger c_{\mathbf{q}} + \sum_{\mathbf{q}} \varepsilon_{\mathbf{q}}^\downarrow d_{\mathbf{q}}^\dagger d_{\mathbf{q}}. \quad (1)$$

In the above equation, $D_k = i\hbar \boldsymbol{\epsilon} \cdot \boldsymbol{\mu} \sqrt{\omega_k / (2\varepsilon_0 \hbar V)}$ is the dipole coupling strength with $\boldsymbol{\epsilon}$ and $\boldsymbol{\mu}$ being the polarization vector of the photon and the dipole moment of the exciton, respectively. b_k is the photon operator, $X = \sum_k D_k b_k^\dagger$, and $c_{\mathbf{q}}$ and $d_{\mathbf{q}}$ denote the electron operators in the left and right reservoirs, respectively.

The couplings to the electron and hole reservoirs are given by the standard tunnel Hamiltonian H_V , where $V_{\mathbf{q}}$ and $W_{\mathbf{q}}$ couple the channels \mathbf{q} of the electron and hole reservoirs. If the couplings to the electron and the hole reservoirs are weak, it is reasonable to assume that the standard Born-Markov approximation with respect to these couplings is valid. In this case, one can derive a master equation from the exact time evolution of the system. The equations of motion can be expressed as (cf. Ref. 15)

$$\begin{aligned} \frac{\partial}{\partial t} \langle \hat{n}_\uparrow \rangle_t &= - \int dt' [C(t-t') + C^*(t-t')] \langle \hat{n}_\uparrow \rangle_{t'} \\ &+ \Gamma_L [1 - \langle \hat{n}_\uparrow \rangle_t - \langle \hat{n}_\downarrow \rangle_t], \end{aligned} \quad (2)$$

$$\frac{\partial}{\partial t} \langle \hat{n}_\downarrow \rangle_t = \int dt' [C(t-t') + C^*(t-t')] \langle \hat{n}_\uparrow \rangle_{t'} - \Gamma_R \langle \hat{n}_\downarrow \rangle_t,$$

$$\frac{\partial}{\partial t} \langle \hat{p} \rangle_t = - \frac{1}{2} \int dt' [C(t-t') + C^*(t-t')] \langle \hat{p} \rangle_{t'} - \frac{\Gamma_R}{2} \langle \hat{p} \rangle_t,$$

where $\Gamma_L = 2\pi \sum_{\mathbf{q}} V_{\mathbf{q}}^2 \delta(\varepsilon_\uparrow - \varepsilon_{\mathbf{q}}^\uparrow)$, $\Gamma_R = 2\pi \sum_{\mathbf{q}} W_{\mathbf{q}}^2 \delta(\varepsilon_\downarrow - \varepsilon_{\mathbf{q}}^\downarrow)$, and $\varepsilon = \hbar \omega_0 = \varepsilon_\uparrow - \varepsilon_\downarrow$ is the energy gap of the QD exciton. Here, $C(t-t') \equiv \langle X_t X_{t'}^\dagger \rangle_0$ is the photon correlation function, and depends on the time interval only. We can now define the Laplace transformation for real z

$$C_\varepsilon(z) \equiv \int_0^\infty dt e^{-zt} e^{i\varepsilon t} C(t)$$

$$n_\uparrow(z) \equiv \int_0^\infty dt e^{-zt} \langle \hat{n}_\uparrow \rangle_t \quad \text{etc.}, \quad z > 0 \quad (3)$$

and transform the whole equations of motion into z space

$$n_\uparrow(z) = - [C_\varepsilon(z) + C_\varepsilon^*(z)] n_\uparrow(z)/z + \frac{\Gamma_L}{z} [1/z - n_\uparrow(z) - n_\downarrow(z)],$$

$$n_\downarrow(z) = [C_\varepsilon(z) + C_\varepsilon^*(z)] n_\downarrow(z)/z - \frac{\Gamma_R}{z} n_\downarrow(z),$$

$$p(z) = - \frac{1}{2} [C_\varepsilon(z) + C_\varepsilon^*(z)] p(z)/z - \frac{\Gamma_R}{2z} p(z). \quad (4)$$

These equations can then be solved algebraically, and the tunnel current from the hole- or electron-side barrier

$$\hat{I}_R = -e \Gamma_R \langle \hat{n}_\downarrow \rangle_t, \quad \hat{I}_L = -e \Gamma_L [1 - \langle \hat{n}_\uparrow \rangle_t - \langle \hat{n}_\downarrow \rangle_t] \quad (5)$$

can in principle be obtained by performing the inverse Laplace transformation on Eqs. (4). Depending on the complexity of the correlation function $C(t-t')$ in the time domain, this can be a formidable task which can however be avoided if one directly seeks the quantum noise:

Shot noise spectrum. In a quantum conductor in nonequilibrium, electronic current noise originates from the dynamical fluctuations of the current around its average. To study correlations between carriers, we relate the exciton dynamics with the hole reservoir operators by introducing the degree of freedom n as the number of holes that have tunneled through the hole-side barrier¹⁶ and write

$$\dot{n}_0^{(n)}(t) = -\Gamma_L n_0^{(n)}(t) + \Gamma_R n_\downarrow^{(n-1)}(t),$$

$$\dot{n}_\uparrow^{(n)}(t) + \dot{n}_\downarrow^{(n)}(t) = (\Gamma_L - \Gamma_R) n_0^{(n)}(t). \quad (6)$$

Equations (6) allow us to calculate the particle current and the noise spectrum from $P_n(t) = n_0^{(n)}(t) + n_\uparrow^{(n)}(t) + n_\downarrow^{(n)}(t)$ which gives the total probability of finding n electrons in the collector by time t . In particular, the noise spectrum S_{I_R} can be calculated via the MacDonald formula^{12,17}

$$S_{I_R}(\omega) = 2\omega e^2 \int_0^\infty dt \sin(\omega t) \frac{d}{dt} [\langle n^2(t) \rangle - (t\langle I \rangle)^2], \quad (7)$$

where $(d/dt)\langle n^2(t) \rangle = \sum_n n^2 \dot{P}_n(t)$. Solving Eqs. (4) and (6), we obtain

$$S_{I_R}(\omega) = 2eI \{1 + \Gamma_R [\hat{n}_\downarrow(z = -i\omega) + \hat{n}_\downarrow(z = i\omega)]\}. \quad (8)$$

In the zero-frequency limit, Eq. (6) reduces to

$$S_{I_R}(\omega = 0) = 2eI \left\{ 1 + 2\Gamma_R \frac{d}{dz} [z \hat{n}_\downarrow(z)]_{z=0} \right\}. \quad (9)$$

As can be seen, there is no need to evaluate the correlation function $C(t-t')$ in the time domain such that all one has to do is to solve Eq. (4) in z space.

Results and discussions. The above derivation shows that the noise spectrum of the QD excitons depends strongly on

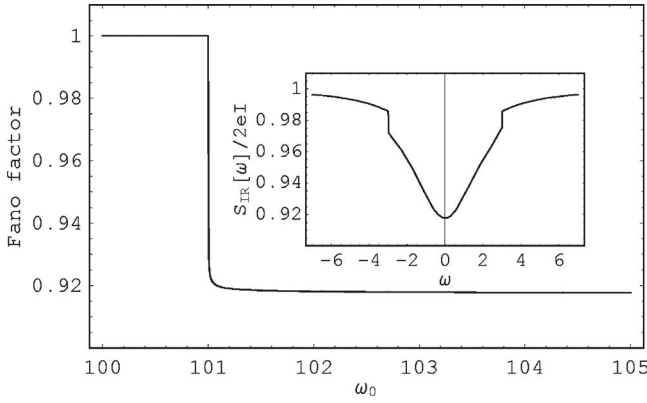


FIG. 2. Current noise (Fano factor) of QD excitons in a one-band PC as a function of the exciton band gap ω_0 . The PBG frequency ω_c is set equal to 101β . The inset shows frequency-dependent noise, in which ω_0 is fixed to 104β .

$C_\varepsilon(z)$. Let us now turn our attention to the spontaneous emission of a QD exciton in a three-dimensional PC, where the vacuum dispersion relation is strongly modified: An anisotropic band-gap structure is formed on the surface of the first Brillouin zone in the reciprocal lattice space. In general, the band edge is associated with a finite collection of symmetrically placed points \mathbf{k}_0^i leading to a three-dimensional band structure.³ In our study, the transition energy of the QD exciton is assumed to be near the band edge ω_c . The dispersion relation for those wave vectors \mathbf{k} whose directions are near one of the \mathbf{k}_0^i can be expressed approximately by $\omega_{\mathbf{k}} = \omega_c + A|\mathbf{k} - \mathbf{k}_0^i|^2$, where A is a model dependent constant.¹⁸ Thus, the correlation function $C_\varepsilon(z) = \sum_{\mathbf{k}} |gD_{\mathbf{k}}|^2 / [z + i(\omega_{\mathbf{k}} - \omega_0)]$ can be calculated around the directions of each \mathbf{k}_0^i separately, and is given by

$$C_\varepsilon(z) = \frac{-i\omega_0^2\beta^{3/2}}{\sqrt{\omega_c + \sqrt{-iz - (\omega_0 - \omega_c)}}}, \quad (10)$$

with $\beta^{3/2} = d^2 \sum_i \sin^2 \theta_i / 8\pi\epsilon_0 \hbar A^{3/2}$.¹⁹ Here, $\hbar\omega_0$ is the transition energy of the QD exciton, d is the magnitude of the dipole moment, and θ_i is the angle between the dipole vector of the exciton and the i th \mathbf{k}_0^i .

The shot-noise spectrum of QD excitons inside a PC is displayed in Fig. 2, where the tunneling rates Γ_L and Γ_R are assumed to be equal to 0.1β and β , respectively. We see that the Fano factor [$F \equiv S_{I_R}(\omega=0)/2e\langle I \rangle$] displays a discontinuity as the exciton transition frequency is tuned across the PBG frequency ($\omega_c = 101\beta$). It also reflects the fact that below the band edge frequency ω_c , spontaneous emission of the QD exciton is inhibited. To observe this experimentally, a dc electric field (or magnetic field) could be applied in order to vary the band-gap energy of the QD exciton. Another way to examine the PBG frequency is to measure the frequency-dependent noise as shown in the inset of Fig. 2, where the exciton band gap is set equal to 104β . As can be seen, discontinuities also appear as ω is equal to the *detuned* frequency between PBG and QD exciton.

When the atomic resonant transition frequency is very close to the edge of the band and the band gap is relatively

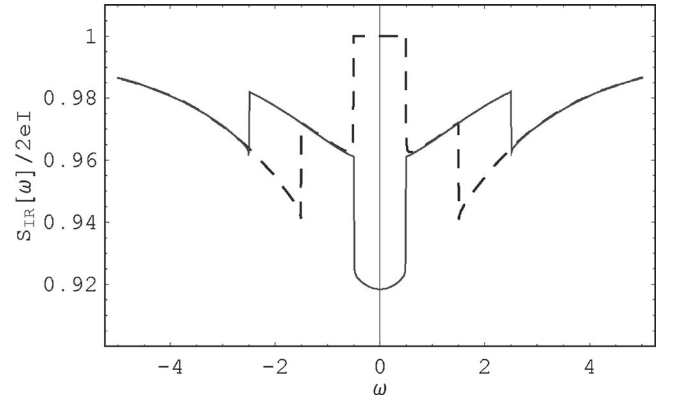


FIG. 3. Shot-noise spectrum of QD excitons in a two-band PC with ω_{c_1} and ω_{c_2} set equal to 101β and 99β , respectively. To demonstrate the ability of extracting information from the PC, the exciton band gap ω_0 in gray and dashed curves is chosen as above ω_{c_2} ($\omega_0 = 101.5\beta$) and between the two band edge frequencies ($\omega_0 = 100.5\beta$), respectively.

large, the above one-band model is a good approximation. If the band gap is narrow, one must consider both upper and lower bands. For a three-dimensional anisotropic PC with point-group symmetry, the dispersion relation near two band edges can be approximated as

$$\omega_{\mathbf{k}} = \begin{cases} \omega_{c_1} + C_1|\mathbf{k} - \mathbf{k}_{10}^i| & (\omega_{\mathbf{k}} > \omega_{c_1}), \\ \omega_{c_2} - C_2|\mathbf{k} - \mathbf{k}_{20}^j| & (\omega_{\mathbf{k}} < \omega_{c_2}). \end{cases} \quad (11)$$

Here, \mathbf{k}_{10}^i and \mathbf{k}_{20}^j are two finite collections of symmetry related points, which are associated with the upper and lower band edges,²⁰ and C_1 and C_2 are model-dependent constants. Following the derivation for the one-band PC, the correlation function can now be written as

$$C_\varepsilon(z) = \sum_{n=1}^2 \frac{(-1)^n i \omega_0^2 \beta_n^{3/2}}{\sqrt{\omega_{c_n} + \sqrt{(-1)^n [iz + (\omega_0 - \omega_{c_n})]}}}, \quad (12)$$

where $\beta_n^{3/2} = d^2 \sum_i \sin^2 \theta_i^{(n)} / 8\pi\epsilon_0 \hbar C_n^{3/2}$ with the corresponding collections of angles $\theta_i^{(n)}$, $n = 1, 2$.

Figure 3 illustrates the frequency-dependent noise of QD excitons embedded inside a two-band PC. The two-band edge frequencies ω_{c_1} and ω_{c_2} are set equal to 101β and 99β , respectively. There are three regimes for the choices of the exciton band gap: $\omega_0 > \omega_{c_1}$, $\omega_0 < \omega_{c_2}$, and $\omega_{c_1} > \omega_0 > \omega_{c_2}$. When ω_0 is tuned above the upper band-edge ω_{c_1} (or below the lower band-edge ω_{c_2}), the QD exciton is allowed to decay, such that the shot noise spectrum (gray curve) is suppressed in the range of $|\omega| < |\omega_0 - \omega_{c_1}|$. On the other hand, however, if ω_0 is between the two band edges, spontaneous emission is inhibited. As shown by the dashed curve, the current noise in the central region is increased with its value equal to unity. Similar to the one-band PC, the curves of the shot noise spectrum reveal two discontinuities at $|\omega| = |\omega_0 - \omega_{c_1}|$ or $|\omega_0 - \omega_{c_2}|$, demonstrating the possibility to extract information from a PC by the current noise.

A few remarks about the application of the QDs inside a PC should be mentioned here. As is known, controlling the

propagation of light (waveguide) is one of the optoelectronic applications of PCs.²¹ By controlling the exciton band-gap ω_0 across the PBG frequency with appropriate tunneling rates of the electron and hole, one may achieve the emission of a single photon at predetermined times and directions (waveguides),²² which are important for the field of quantum information technology. Furthermore, it has been demonstrated recently that a precise spatial and spectral overlap between a single self-assembled quantum dot and a photonic crystal membrane nanocavity can be implemented by a deterministic approach.²³ One of the immediate applications is the coupling of two QDs to a single common cavity mode.²⁴ Therefore, if two QD p - i - n junctions can also be incorporated inside a PC (and on the way of light propagation), the cavitylike effect may be used to create an entangled state

between two QD excitons with remote separation.¹³ The obvious advantages then would be a suppression of decoherence of the entangled state by the PBG, and the observation of the enhanced shot noise could serve in order to identify the entangled state.¹⁰

In summary, we have derived the nonequilibrium current noise of QD excitons incorporated in a p - i - n junction surrounded by a one-band or two-band PC. We found that characteristic features of the PBG can be obtained from the shot noise spectrum. Generalizations to other types of PCs are expected to be relatively straightforward, which makes QD p - i - n junctions good detectors of quantum noise.²⁵

This work is supported partially by the National Science Council of Taiwan under Grant Nos. NSC 94-2112-M-009-019 and NSC 94-2120-M-009-002.

¹E. Yablonovitch, Phys. Rev. Lett. **58**, 2059 (1987).

²S. Sakoda, *Optical Properties of Photonic Crystals* (Springer, New York, 2001).

³S. John, Phys. Rev. Lett. **58**, 2486 (1987).

⁴E. M. Purcell, Phys. Rev. **69**, 681 (1946).

⁵P. Goy, J. M. Raimond, M. Gross, and S. Haroche, Phys. Rev. Lett. **50**, 1903 (1983); G. Gabrielse and H. Dehmelt, *ibid.* **55**, 67 (1985); R. G. Hulet, E. S. Hilfer, and D. Kleppner, *ibid.* **55**, 2137 (1985); D. J. Heinzen, J. J. Childs, J. E. Thomas, and M. S. Feld, *ibid.* **58**, 1320 (1987).

⁶M. Bayer, F. Weidner, A. Larionov, A. McDonald, A. Forchel, and T. L. Reinecke, Phys. Rev. Lett. **86**, 3168 (2001); G. S. Solomon, M. Pelton, and Y. Yamamoto, *ibid.* **86**, 3903 (2001).

⁷C. Constantin, E. Martinet, D. Y. Oberli, E. Kapon, B. Gayral, and J. M. Gerard, Phys. Rev. B **66**, 165306 (2002).

⁸C. W. J. Beenakker, Rev. Mod. Phys. **69**, 731 (1997); Y. M. Blanter and M. Buttiker, Phys. Rep. **336**, 1 (2000).

⁹G. Kießlich, A. Wacker, E. Schöll, S. A. Vitusevich, A. E. Belyaev, S. V. Danylyuk, A. Förster, N. Klein, and M. Henini, Phys. Rev. B **68**, 125331 (2003).

¹⁰Y. N. Chen, T. Brandes, C. M. Li, and D. S. Chuu, Phys. Rev. B **69**, 245323 (2004).

¹¹P. Lodahl, A. Floris van Driel, Ivan S. Nikolaev, Arie Irman, Karin Overgaag, Daniël Vanmaekelbergh, and Willem L. Vos, Nature (London) **430**, 654 (2004); T. Yoshie, A. Scherer, J. Hendrickson, G. Khitrova, H. M. Gibbs, G. Rupper, C. Ell, O. B. Shchekin, and D. G. Deppe, *ibid.* **432**, 200 (2004).

¹²D. K. C. MacDonald, Rep. Prog. Phys. **12**, 56 (1948).

¹³Y. N. Chen, D. S. Chuu, and T. Brandes, Phys. Rev. Lett. **90**, 166802 (2003).

¹⁴Z. Yuan, B. E. Kardynal, R. M. Stevenson, A. J. Shields, C. J. Lobo, K. Cooper, N. S. Beattie, D. A. Ritchie, and M. Pepper, Science **295**, 102 (2002).

¹⁵T. Brandes and B. Kramer, Phys. Rev. Lett. **83**, 3021 (1999); Y. N. Chen and D. S. Chuu, Phys. Rev. B **66**, 165316 (2002).

¹⁶Actually, the total current noise should be expressed in terms of the spectra of particle currents and the charge noise spectrum: $S_I(\omega) = aS_{I_L}(\omega) + bS_{I_R}(\omega) - ab\omega^2 S_Q(\omega)$, where a and b are capacitance coefficient ($a+b=1$) of the junctions. Since we have assumed a highly asymmetric setup ($a \ll b$), it is plausible to consider the hole-side spectra $S_{I_R}(\omega)$ only.

¹⁷R. Aguado and T. Brandes, Phys. Rev. Lett. **92**, 206601 (2004).

¹⁸In fact, A is dependent on the structures of the photonic crystals. For a simple three-dimensional periodic dielectric, A can be approximated as $A \approx \omega_c / (\mathbf{k}_0^i)^2$, where $\mathbf{k}_0^i = \pi/L$ with L being the lattice constant of the photonic crystal (Ref. 18). In order not to lose the generality, we let A being a constant, such that β becomes the unit for the numerical calculations.

¹⁹S. John and T. Quang, Phys. Rev. A **50**, 1764 (1994); S. Y. Zhu, Y. Yang, H. Chen, H. Zheng, and M. S. Zubairy, Phys. Rev. Lett. **84**, 2136 (2000); N. Vats, S. John, and K. Busch, Phys. Rev. A **65**, 043808 (2002).

²⁰Y. Yang, M. Fleischhauer, and S. Y. Zhu, Phys. Rev. A **68**, 043805 (2003).

²¹E. Chow, S. Y. Lin, S. G. Johnson, P. R. Villeneuve, J. D. Joannopoulos, J. R. Wendt, G. A. Vawter, W. Zubrzycki, H. Hou, and A. Alleman, Nature (London) **407**, 983 (2000).

²²E. Lidorikis, M. L. Povinelli, S. G. Johnson, and J. D. Joannopoulos, Phys. Rev. Lett. **91**, 023902 (2003).

²³A. Badolato, K. Hennessy, M. Atatüre, J. Dreiser, E. Hu, P. M. Petroff, and A. Imamoglu, Science **308**, 1158 (2005).

²⁴A. Imamoglu, D. D. Awschalom, G. Burkard, D. P. DiVincenzo, D. Loss, M. Sherwin, and A. Small, Phys. Rev. Lett. **83**, 4204 (1999).

²⁵R. Aguado and L. P. Kouwenhoven, Phys. Rev. Lett. **84**, 1986 (2000).

Shot noise of quantum ring excitons in a planar microcavity

Y. N. Chen, D. S. Chuu, and S. J. Cheng

Department of Electrophysics, National Chiao-Tung University, Hsinchu 300, Taiwan

(Received 25 July 2005; revised manuscript received 5 September 2005; published 1 December 2005)

Shot noise of quantum ring (QR) excitons in a p-i-n junction surrounded by a microcavity is investigated theoretically. Some radiative decay properties of a QR exciton in a microcavity can be obtained from the observation of the current noise, which also gives extra information about one of the tunnel barriers. A different noise feature between the quantum dot (QD) and QR is pointed out, and may be observed in a suitably designed experiment.

 DOI: [10.1103/PhysRevB.72.233301](https://doi.org/10.1103/PhysRevB.72.233301)

PACS number(s): 71.35.-y, 73.63.-b, 73.50.Td, 42.50.Pq

Since Purcell proposed the idea of controlling the spontaneous emission rate by using a cavity,¹ the enhanced and inhibited SE rate for the atomic system was intensively investigated in the 1980s² by using atoms passed through a cavity. In semiconductor systems, the electron-hole pair is naturally a candidate to examine the spontaneous emission. Modifications of the SE rates of the quantum dot (QD),³ quantum wire,⁴ or quantum well⁵ excitons inside the microcavities have been observed experimentally.

Interest in measurements of shot noise spectrum has risen owing to the possibility of extracting valuable information not available in conventional dc transport experiments.⁶ With the advances of fabrication technologies, it is now possible to embed the QDs inside a p-i-n structure⁷ such that the electron and hole can be injected separately from opposite sides. This allows one to examine the exciton dynamics in a QD via electrical currents.⁸ On the other hand, it is now possible to fabricate the ring-shaped dots of InAs in GaAs with a circumference of several hundred nanometers.⁹ Optical detection of the Aharonov-Bohm effect on an exciton in a single quantum ring (QR) was also reported.¹⁰

Based on the rapid progress of nanotechnologies, it is not hard to imagine that the QR can be incorporated in a p-i-n junction surrounded by the microcavity. Examinations of the dynamics of the QR excitons by the electrical currents can be realized. We thus present in this work the nonequilibrium calculations of such a device. Current noise of QR excitons in a planar microcavity is obtained via the MacDonald formula¹¹ and is found to reveal some characteristics of the restricted environment, i.e., the density of states of the confined photons.

The model. Consider now a QR embedded in a p-i-n junction as shown in Fig. 1. Both the hole and electron reservoirs are assumed to be in thermal equilibrium. For the physical phenomena we are interested in, the Fermi level of the $p(n)$ -side hole (electron) is slightly lower (higher) than the hole (electron) subband in the dot. After a hole is injected into the hole subband in the QR, the n -side electron can tunnel into the exciton level because of the Coulomb interaction between the electron and hole. Thus, we may introduce the three ring states; $|0\rangle=|0,h\rangle$, $|\uparrow\rangle=|e,h\rangle$, and $|\downarrow\rangle=|0,0\rangle$, where $|0,h\rangle$ means there is one hole in the QR, $|e,h\rangle$ is the exciton state, and $|0,0\rangle$ represents the ground state with no hole and electron in the QR. One might argue

that one cannot neglect the state $|e,0\rangle$ for real device since the tunable variable is the applied voltage. This can be resolved by fabricating a thicker barrier on the electron side so that there is little chance for an electron to tunnel in advance. Moreover, the charged exciton and biexcitons states are also neglected in our calculations. This means a low injection limit is required in the experiment.⁷

Derivation of a master equation. We can now define the ring-operators $\hat{n}_\uparrow \equiv |\uparrow\rangle\langle\uparrow|$, $\hat{n}_\downarrow \equiv |\downarrow\rangle\langle\downarrow|$, $\hat{p} \equiv |\uparrow\rangle\langle\downarrow|$, $\hat{s}_\uparrow \equiv |0\rangle\langle\uparrow|$, $\hat{s}_\downarrow \equiv |0\rangle\langle\downarrow|$. The total Hamiltonian H of the system consists of three parts; H_0 [ring, photon bath H_p , and the electron (hole) reservoirs H_{res}], H_T (ring-photon coupling), and the ring-reservoir coupling H_V

$$H = H_0 + H_T + H_V,$$

$$H_0 = \varepsilon_\uparrow \hat{n}_\uparrow + \varepsilon_\downarrow \hat{n}_\downarrow + H_p + H_{res},$$

$$H_T = \sum_k (D_k \hat{b}_k^\dagger \hat{p} + D_k^* \hat{p} \hat{b}_k) = \hat{p} X + \hat{p}^\dagger X^\dagger,$$

$$H_p = \sum_k \omega_k \hat{b}_k^\dagger \hat{b}_k,$$

$$H_V = \sum_{\mathbf{q}} (V_{\mathbf{q}} \hat{c}_{\mathbf{q}}^\dagger \hat{s}_\uparrow + W_{\mathbf{q}} \hat{d}_{\mathbf{q}}^\dagger \hat{s}_\downarrow + \text{c.c.}),$$

$$H_{res} = \sum_{\mathbf{q}} \varepsilon_{\mathbf{q}} \hat{c}_{\mathbf{q}}^\dagger \hat{c}_{\mathbf{q}} + \sum_{\mathbf{q}} \varepsilon_{\mathbf{q}} \hat{d}_{\mathbf{q}}^\dagger \hat{d}_{\mathbf{q}}. \quad (1)$$

In the above equation, b_k is the photon operator, D_k is the dipole coupling strength, $X = \sum_k D_k \hat{b}_k^\dagger$, and $c_{\mathbf{q}}$ and $d_{\mathbf{q}}$ denote the electron operators in the left and right reservoirs, respectively. The couplings to the electron and hole reservoirs are given by the standard tunnel Hamiltonian H_V , where $V_{\mathbf{q}}$ and $W_{\mathbf{q}}$ couple the channels \mathbf{q} of the electron and the hole reservoirs. If the couplings to the electron and the hole reservoirs are weak, then it is reasonable to assume that the standard Born-Markov approximation with respect to these couplings is valid. In this case, one can derive a master equation from the exact time evolution of the system. The equations of motion can be expressed as (cf. Ref. 12)

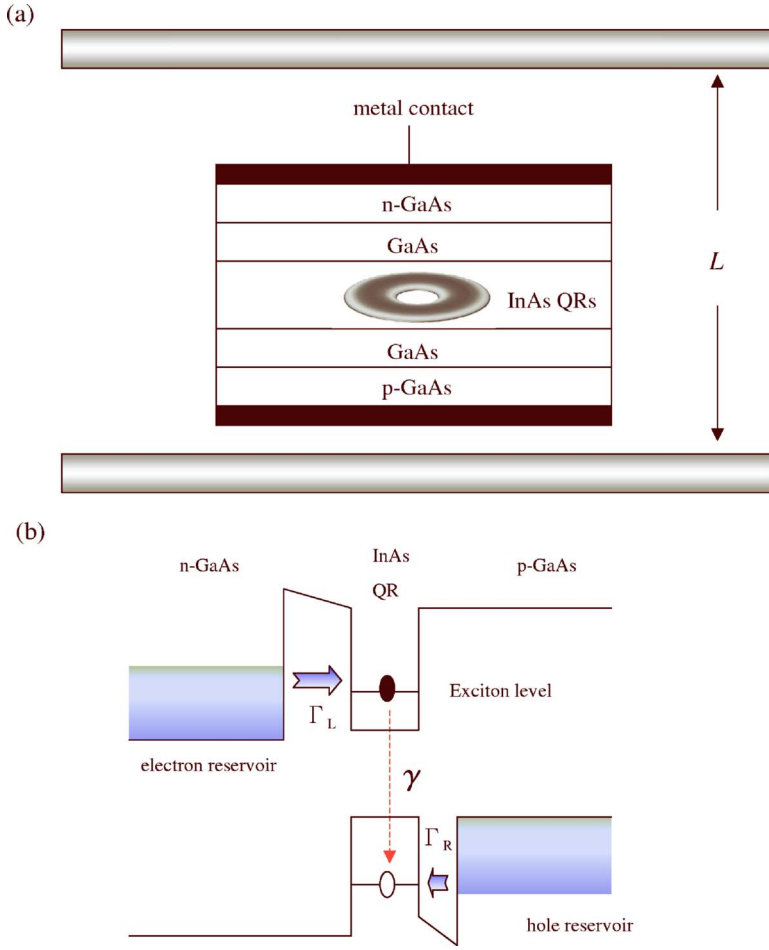


FIG. 1. (Color online) (a) Schematic description of a QR inside a p-i-n junction surrounded by a planar microcavity with length L . (b) Energy-band diagram of a QR in the p-i-n junction.

$$\begin{aligned}
 \frac{\partial}{\partial t} \langle \hat{n}_{\uparrow} \rangle_t &= - \int dt' [C(t-t') + C^*(t-t')] \langle \hat{n}_{\uparrow} \rangle_{t'} \\
 &\quad + \Gamma_L [1 - \langle \hat{n}_{\uparrow} \rangle_t - \langle \hat{n}_{\downarrow} \rangle_t], \\
 \frac{\partial}{\partial t} \langle \hat{n}_{\downarrow} \rangle_t &= \int dt' [C(t-t') + C^*(t-t')] \langle \hat{n}_{\uparrow} \rangle_{t'} - \Gamma_R \langle \hat{n}_{\downarrow} \rangle_t, \\
 \frac{\partial}{\partial t} \langle \hat{p} \rangle_t &= - \frac{1}{2} \int dt' [C(t-t') + C^*(t-t')] \langle \hat{p} \rangle_{t'} - \frac{\Gamma_R}{2} \langle \hat{p} \rangle_t,
 \end{aligned} \tag{2}$$

where $\Gamma_L = 2\pi \sum_{\mathbf{q}} V_{\mathbf{q}}^2 \delta(\varepsilon_{\uparrow} - \varepsilon_{\mathbf{q}}^{\uparrow})$, $\Gamma_R = 2\pi \sum_{\mathbf{q}} W_{\mathbf{q}}^2 \delta(\varepsilon_{\downarrow} - \varepsilon_{\mathbf{q}}^{\downarrow})$, and $\varepsilon = \varepsilon_{\uparrow} - \varepsilon_{\downarrow}$ is the energy gap of the QR exciton. Here, $C(t-t') \equiv \langle X_t X_{t'}^{\dagger} \rangle_0$ is the photon correlation function, and depends on the time interval only. We can now define the Laplace transformation for real z ,

$$\begin{aligned}
 C_{\varepsilon}(z) &\equiv \int_0^{\infty} dt e^{-zt} e^{i\varepsilon t} C(t), \\
 n_{\uparrow}(z) &\equiv \int_0^{\infty} dt e^{-zt} \langle \hat{n}_{\uparrow} \rangle_t \text{ etc.}, \quad z > 0,
 \end{aligned} \tag{3}$$

and transform the whole equations of motion into z space,

$$\begin{aligned}
 n_{\uparrow}(z) &= - [C_{\varepsilon}(z) + C_{\varepsilon}^*(z)] n_{\uparrow}(z) / z + \frac{\Gamma_L}{z} [1/z - n_{\uparrow}(z) - n_{\downarrow}(z)], \\
 n_{\downarrow}(z) &= [C_{\varepsilon}(z) + C_{\varepsilon}^*(z)] n_{\downarrow}(z) / z - \frac{\Gamma_R}{z} n_{\downarrow}(z), \\
 p(z) &= - \frac{1}{2} [C_{\varepsilon}(z) + C_{\varepsilon}^*(z)] p(z) / z - \frac{\Gamma_R}{2z} p(z).
 \end{aligned} \tag{4}$$

These equations can then be solved algebraically, and the tunnel current from the hole- or electron-side barrier

$$\hat{I}_R = -e \Gamma_R \langle \hat{n}_{\downarrow} \rangle_t, \quad \hat{I}_L = -e \Gamma_L [1 - \langle \hat{n}_{\uparrow} \rangle_t - \langle \hat{n}_{\downarrow} \rangle_t] \tag{5}$$

can then be obtained by performing the inverse Laplace transformation on Eqs. (4).

Shot noise spectrum. In a quantum conductor in nonequilibrium, electronic current noise originates from the dynamical fluctuations of the current being away from its average. To study correlations between carriers, we relate the exciton dynamics with the hole reservoir operators by introducing the degree of freedom n as the number of holes that have tunneled through the hole-side barrier¹³ and write

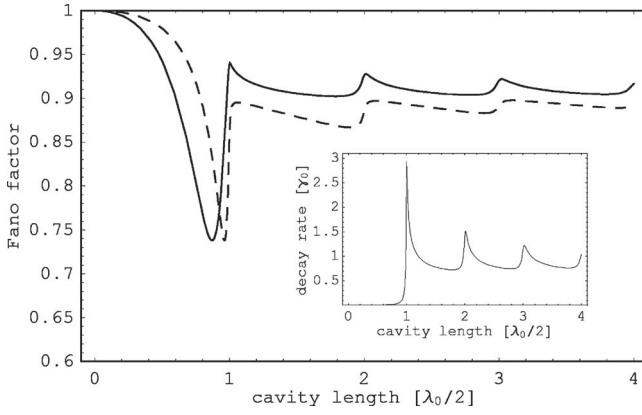


FIG. 2. Fano factor as a function of cavity length L . The vertical and horizontal units are $[S_{I_R}(0)]/(2eI)$ and $\lambda_0/2$, respectively. The inset shows the radiative decay rate of a QR exciton in a planar microcavity.

$$\begin{aligned} \dot{n}_0^{(n)}(t) &= -\Gamma_L n_0^{(n)}(t) + \Gamma_R n_{\downarrow}^{(n-1)}(t), \\ \dot{n}_{\uparrow}^{(n)}(t) + \dot{n}_{\downarrow}^{(n)}(t) &= (\Gamma_L - \Gamma_R) n_0^{(n)}(t). \end{aligned} \quad (6)$$

Equation (6) allows us to calculate the particle current and the noise spectrum from $P_n(t) = n_0^{(n)}(t) + n_{\uparrow}^{(n)}(t) + n_{\downarrow}^{(n)}(t)$ which gives the total probability of finding n electrons in the collector by time t . In particular, the noise spectrum S_{I_R} can be calculated via the MacDonald formula.¹⁴ In the zero-frequency limit, the Fano factor can be written as

$$F \equiv \frac{S_{I_R}(\omega=0)}{2e\langle I \rangle} = 1 - \frac{A(z)\Gamma_L\Gamma_R[A(z) + 2(\Gamma_L + \Gamma_R)]}{\{A(z)\Gamma_R + \Gamma_L[A(z) + 2\Gamma_R]\}^2} \Big|_{z=0}, \quad (7)$$

where $A(z) \equiv C_e(z) + C_e^*(z)$.

Results and Discussions. From Eq. (7), one knows that the noise spectrum of the QR excitons depends strongly on $C_e(z)$, which reduces to the radiative decay rate γ in the Markovian limit. The exciton decay rate γ in a microcavity can be obtained easily from the perturbation theory and is given by

$$\begin{aligned} \gamma &= \frac{e^2 \hbar \rho}{m^2 c d} \int |H_0^{(1)}| \\ &\times \langle (q' \rho)^2 q' \left(\sum_{k'_z} \frac{\delta(\varepsilon - c\sqrt{q'^2 + k'_z{}^2})}{\sqrt{k'_z{}^2 + q'^2}} |\epsilon_{q'k'_z\lambda} \cdot \chi|^2 \right) dq', \end{aligned} \quad (8)$$

where ρ is the ring radius, d is the lattice spacing, $H_0^{(1)}$ is the Hankel function, $\epsilon_{q'k'_z}$ is the polarization of the photon, and χ is the dipole moment of the QR exciton.¹⁵ The summation of the integer modes in the k'_z direction is determined from the boundary conditions of the planar microcavity.

The radiative decay rate γ of a QR exciton inside a planar microcavity is numerically displayed in the inset of Fig. 2. The tunneling rates, Γ_L and Γ_R , are assumed to be equal to $0.1\gamma_0$ and γ_0 , where γ_0 ($\sim 1/1$ ns) is the decay rate of a QR

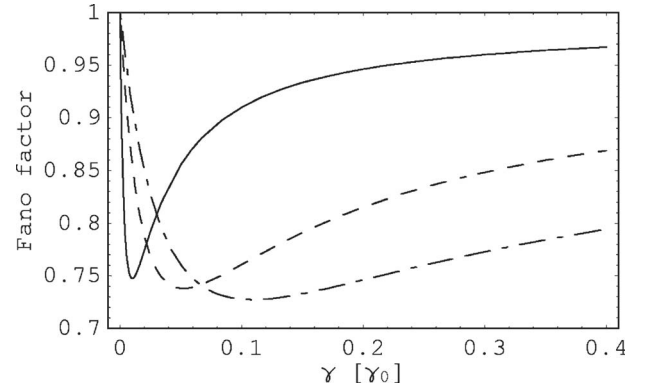


FIG. 3. Fano factor as a function of the decay rate for different electron-side tunneling rate $\Gamma_L = 0.01\gamma_0$ (solid line), $0.05\gamma_0$ (dashed line), and $0.1\gamma_0$ (dashed-dotted line). The hole-side tunneling rate is fixed ($\Gamma_R = \gamma_0$).

exciton in free space. Also, the planar microcavity is assumed to have a Lorentzian broadening at each resonant mode (with broadening width equal to 1% of each resonant mode).¹⁶ As the cavity length is shorter than one half the wavelength of the emitted photon ($L < \lambda_0/2$), the decay rate is inhibited because of the cut-off frequency of the cavity. When the cavity length exceeds some multiple wavelength, it opens up another decay channel for the quantum ring exciton and turns out that there is an abrupt enhancement on the decay rate. Such a singular behavior also happens in the decay of one dimensional quantum wire polaritons inside a microcavity.¹⁶ This is because the ring geometry preserves the angular momentum of the exciton, rendering the formation of exciton-polariton in the direction of circumference. This kind of behavior can also be found in the calculations of a Fano factor as demonstrated by the solid line in Fig. 2. Comparing to the zero-frequency noise of the QD excitons (dashed line), the Fano factor of the QR excitons shows the “cusp” feature at each resonant mode.

Another interesting point is that below the lowest resonant mode ($L = \lambda_0/2$), both the solid and dashed curves have a dip in the Fano factor. It is not seen from the radiative decay rate. To answer this, we have plotted Eq. (7) in Fig. 3 as a function of the decay rate γ . Keeping Γ_R unchanged, the solid, dashed, and dashed-dotted lines correspond to the electron-side tunneling rate $\Gamma_L = 0.01\gamma_0$, $0.5\gamma_0$, and $0.1\gamma_0$, respectively. As can be seen, the Fano factor has a minimum point at $\gamma = \Gamma_L \Gamma_R (\Gamma_L + \Gamma_R) / (\Gamma_L^2 + \Gamma_R^2)$. Comparing this with the inset of Fig. 2, one immediately knows that when the cavity length is increased to $\lambda_0/2$, the abruptly increased decay rate will cross the minimum point and result in a dip in Fig. 2. Furthermore, in the limit of $\Gamma_R \gg \Gamma_L$, the minimum point can be approximated as $\gamma \approx \Gamma_L$. This means by observing the dip in the Fano factor of Fig. 2, the magnitude of the electron-side tunneling rate Γ_L can be obtained.

To further understand the difference between the QD and QR excitons, Fig. 4 illustrates the shot noise as a function of energy gap ε . In plotting the figure, a perfect planar microcavity is assumed for convenience. As can be seen, the shot noise of the QD excitons shows the plateau feature (solid line) with the increasing of ε , while it is a zigzag behavior

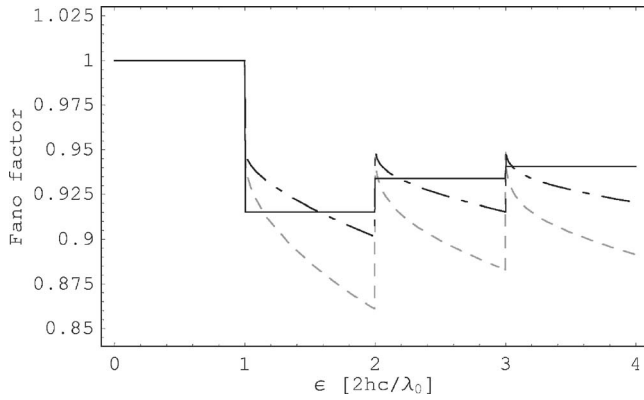


FIG. 4. Fano factor of QD (solid line) and QR (gray dashed line) excitons as a function of energy gap ε . The vertical and horizontal units are $[S_{I_R}(0)]/(2eI)$ and $2hc/\lambda_0$, respectively. The dashed-dotted line represents that if the free-space decay rate of the QR exciton is enhanced by a factor of $2(\gamma_0 \rightarrow 2\gamma_0)$, the shot noise is also enhanced.

(gray-dashed and dashed-dotted lines) for the QR excitons. This is because the decay rate of the QD exciton in a microcavity is given by¹⁶

$$\gamma_{dot} \propto \sum_{n_c} \frac{e^2 \hbar}{m^2 c^2 L} \theta[(\varepsilon/\hbar c)^2 - (\pi n_c / L)^2] |\epsilon_{q'k'_z} \cdot \chi|^2, \quad (9)$$

where θ is the step function, and the summation is over the positive integers. Therefore, when the energy gap ε is tuned above some resonant mode of the cavity, the decay rate is a constant before the next decay channel is opened. On the other hand, however, one knows that the decay rate for the QR exciton is not a constant between two resonant modes. This explains why the decay property for QR exciton is different from that for the QD exciton under the same photonic environment, and the difference may be distinguished by the shot noise measurements. From the experimental point of

view, different dependences on ε are easier to be realized since it is almost impossible to vary the cavity length once the sample is prepared. A possible way to observe the mentioned effects is to vary ε around the discontinuous points and measure the corresponding current noise.

A few remarks about the ring radius should be mentioned here. One should note that we do not give the specific value of the ring radius in our model. Instead, a phenomenological value about the free space decay rate γ_0 is used. The magnitudes of the tunnel rates are set relative to it. In general, the changing of radius will certainly affect the shot noise. For example, because of the exciton-polariton (super radiant) effect in the direction of circumference, an increasing of ring radius will enhance the decay rate. In addition, the dipole moment of the QR exciton χ is also altered because of the varying of the wave function. All these can contribute to the variations of the decay rate and shot noise. In our previous study,¹⁵ we have shown that the decay rate is a monotonic increasing function on radius ρ if the exciton is coherent in the quantum ring, i.e., free of scattering from impurities or imperfect boundaries. The dashed-dotted line in Fig. 4 shows the result for *doubled* free-space decay rate, i.e., $\gamma_0 \rightarrow 2\gamma_0$. Although the noise is increased, the zigzag feature remains unchanged.

In conclusion, we have derived in this work the nonequilibrium current noise of QR excitons incorporated in a p-i-n junction surrounded by a planar microcavity. Some radiative decay properties of the one-dimensional QR exciton can be obtained from the observation of shot noise spectrum, which also shows extra information about the electron-side tunneling rate. Different noise features between the QD and QR are pointed out, and deserve to be tested with present technologies.

This work is supported partially by the National Science Council, Taiwan under Grant Nos. NSC 94-2112-M-009-019 and NSC 94-2120-M-009-002.

¹E. M. Purcell, Phys. Rev. **69**, 681 (1946).

²P. Goy *et al.*, Phys. Rev. Lett. **50**, 1903 (1983); G. Gabrielse and H. Dehmelt, *ibid.* **55**, 67 (1985); R. G. Hulet *et al.*, *ibid.* **55**, 2137 (1985); D. J. Heinzen *et al.*, *ibid.* **58**, 1320 (1987).

³J. M. Gerard *et al.*, Phys. Rev. Lett. **81**, 1110 (1998); M. Bayer *et al.*, *ibid.* **86**, 3168 (2001); G. S. Solomon *et al.*, *ibid.* **86**, 3903 (2001).

⁴C. Constantin *et al.*, Phys. Rev. B **66**, 165306 (2002).

⁵G. Bjork *et al.*, Phys. Rev. A **44**, 669 (1991); K. Tanaka *et al.*, Phys. Rev. Lett. **74**, 3380 (1995).

⁶C. W. J. Beenakker, Rev. Mod. Phys. **69**, 731 (1997); Y. M. Blanter and M. Buttiker, Phys. Rep. **336**, 1 (2000).

⁷Z. Yuan *et al.*, Science **295**, 102 (2002); G. Kießlich *et al.*, Phys. Rev. B **68**, 125331 (2003).

⁸Y. N. Chen *et al.*, Phys. Rev. B **69**, 245323 (2004).

⁹R. J. Warburton *et al.*, Nature (London) **405**, 926 (2000).

¹⁰M. Bayer *et al.*, Phys. Rev. Lett. **90**, 186801 (2003).

¹¹D. K. C. MacDonald, Rep. Prog. Phys. **12**, 56 (1948).

¹²T. Brandes and B. Kramer, Phys. Rev. Lett. **83**, 3021 (1999); Y. N. Chen *et al.*, *ibid.* **90**, 166802 (2003).

¹³Actually, the total current noise should be expressed in terms of the spectra of particle currents and the charge noise spectrum: $S_I(\omega) = aS_{I_L}(\omega) + bS_{I_R}(\omega) - ab\omega^2 S_Q(\omega)$, where a and b are capacitance coefficient ($a+b=1$) of the junctions. Since we have assumed a highly asymmetric set up ($a \ll b$), it is plausible to consider the hole-side spectra $S_{I_R}(\omega)$ only.

¹⁴R. Aguado and T. Brandes, Phys. Rev. Lett. **92**, 206601 (2004).

¹⁵Y. N. Chen and D. S. Chuu, Solid State Commun. **130**, 491 (2004).

¹⁶Y. N. Chen *et al.*, Phys. Rev. B **64**, 125307 (2001).

Studies on the electronic and vibrational states of colloidal CdSe/ZnS quantum dots under high pressures

C. T. Yuan¹, Q. L. Chiu¹, Y. N. Chen^{1,2}, W. C. Chou^{1*}, C.M. Lin³, W. H. Chang⁴, H. S. Lin⁵, R. C. Ruaan⁵, and D. S. Chuu¹

¹Department of Electrophysics, National Chiao Tung University, HsinChu 30010, Taiwan

²National Center for Theoretical Sciences, National Cheng Kung University, Tainan 701, Taiwan

³Department of Applied Science, National Hsinchu University of Education, HsinChu 300, Taiwan

⁴Department of Biomedical Engineering, Chung Yuan Christian University, ChungLi 32023, Taiwan

⁵Department of Chemical and Materials Engineering, National Central University, ChungLi 32001, Taiwan

Abstract

The electronic and vibrational states of colloidal core/shell CdSe/ZnS quantum dots are studied at room temperatures by using high pressure optical measurements. Pressure dependent quadratic lattice behavior can be observed clearly from photoluminescence (PL) and Raman spectra up to ~7 GPa. This quadratic relationship is consistent with theoretical prediction. The average pressure coefficients for PL and Raman measurements, as well as Gruneisen parameter are 32 meV/GPa, 4.2 cm⁻¹ and 0.11, respectively.

*Corresponding author's e-mail: wuchingchou@mail.nctu.edu.tw

I. INTRODUCTION

Colloidal quantum dots (QDs), or semiconductor nanocrystals have attracted much attention for potential applications in biological labels [1~2]. Due to strong confinements in all spatial directions, the emission colors can be tuned to cover whole visible range by changing the size instead of chemical composition [3]. On the other hand, high pressure technique is another approach to vary the electronic levels of crystalline materials. Incorporation colloidal QDs under high pressure environment can provide valuable information to study the electronic and vibrational states of nanometer size materials. Previous reports have demonstrated that colloidal QDs exhibit distinct properties from bulk materials. For example, structural transformation of CdSe bulks from wurtzite to rock salt occurred at the pressure of ~3 GPa [4]. In contrast to bulk CdSe, the structures of nanocrystals are stable more than 5 GPa [5~6]. For both of bulk materials and nanocrystals, the variations of the lattice are all linearly dependent on the applied pressures. However, from the theoretical predictions [7], the lattice behavior under high pressure should follow quadratic relationship since the bulk modulus is a function of pressures. Surprisingly, this quadratic behavior was not observed explicitly in previous reports [4~6]. One possible reason is that the limitation of phase transformation occurred before entering quadratic regime. To confirm this, it is necessary to delay the transformation pressure of samples.

To observe this quadratic behavior, the colloidal CdSe QDs with ZnS thin capping layers were investigated under high pressure with de-ionized water as the pressure transmit medium. PL and Raman scattering measurements have been performed under various pressures up to 6~7 GPa at room temperatures. Quadratic relationship between lattice properties and applied pressures are observed explicitly from both PL and Raman scattering. The average pressure coefficients for PL and Raman measurements, as well as Gruneisen parameter are found to be 32 meV/GPa , 4.2

cm⁻¹ and 0.11, respectively.

II. EXPERIMENT

For room temperature PL measurements, the incident beam from Ti:sapphire laser were guided through the doubly BBO crystals as the excitation sources. The emitted light was dispersed by a spectrometer and detected by a liquid nitrogen-cooled charge coupled devices. Raman spectra were recorded by collecting scattering line in backscattering configuration. Incident beam from an argon ion laser with 514.5 nm wavelength was focused on a sample through a microscope objective. Notch filter was utilized to reject the unnecessary incident laser line. Hydrostatic high pressure surroundings were created within a 0.2 mm hole at the center of steel gaskets embedded by two diamond cells. Colloidal CdSe/ZnS QDs were dissolved into de-ionized water, which is used as a pressure transmit medium under relative high pressure [8]. The applied high pressures were determined by monitoring the Raman shift of the ruby R1 line. Colloidal CdSe/ZnS QDs were wet chemical synthesized by conventional methods [9] and transferred into water pressure medium by replacing original hydrophobic trioctylphosphine oxide (TOPO) with Mercaptopropionic acid (MPA) hydrophilic surface ligands.

III. RESULTS AND DISCUSSIONS

Selected pressure dependent fluorescence spectra are shown in Figure 1 and the corresponding high pressure values are marked in the figure. The main peaks are attributed to band edge emission of the QDs. The typical blue shift with different amount can be observed with increasing pressures below ~7 GPa, subsequently, the fluorescence disappeared abruptly above the pressure. Figure 2 is a plot of the fluorescence peaks as a function of applied hydrostatic pressures. Obviously, quadratic relationship can be observed, that is, the slope decreases with increasing pressure. It implied that the pressure coefficient is not a

constant, but depends on the pressures. The equation $E(P) = E_0 + \alpha P + \beta P^2$ can be used to fit the overall experimental data. Here, α and β are average pressure coefficients, and E_0 is the energy gap at ambient pressure. The fitting parameters for E_0 , α , β are 623 nm, 32 meV/GPa, and -0.001 meV/GPa², respectively. To compare with previous reports [4~6], we divided the overall data into two parts, relative low and high pressure regimes. The threshold pressure is assigned to 3 GPa due to dramatic change of the slope. This threshold is just close to transition pressure of CdSe bulk. The linear function $E(P) = E_0 + \alpha P$ can be used to fit two regimes. The pressure coefficients are 39 and 25 meV/GPa for low and high pressure regimes. The former is close to bulk value [10]. On the contrary, the latter resembles the value of nano-crystals [5].

According to above findings, actually, there is a nonlinear factor that influences the relationship between fluorescence peaks and applied pressures. This effect can be explicitly observed in relative high pressure regime. We thus consider Murnaghan equations which describes the relation between applied pressures and lattice constants, $P = \frac{B}{dB/dP} \left[\left(\frac{a_0}{a_0 + \Delta a} \right)^{3\left(\frac{dB}{dP}\right)} - 1 \right]$, where B is the bulk modulus, a_0 is lattice constant under atmospheric pressure, Δa is the decrement of the lattice constant, which is usually small, induced by the applied pressures.

One can then obtain

$$P \left(\frac{\Delta a}{a_0} \right) = \frac{B}{dB/dP} \left[\left(\frac{1}{1 + \frac{\Delta a}{a_0}} \right)^{3\left(\frac{dB}{dP}\right)} - 1 \right] = -3B \left(\frac{\Delta a}{a_0} \right) + 3 \left(\frac{dB}{dP} \right) \left[3 \left(\frac{dB}{dP} \right) - 1 \right] \left(\frac{\Delta a}{a_0} \right)^2 + \dots$$

high order terms of $\left(\frac{\Delta a}{a_0} \right)$. If we choose $\frac{dB}{dP} \sim 1$ [11],

the equation can be approximated to the form of

$$-3B \left(\frac{\Delta a}{a_0} \right) + 6B \left(\frac{\Delta a}{a_0} \right)^2 + \text{high order terms of } \left(\frac{\Delta a}{a_0} \right).$$

If the external applied pressure is high enough, the second order term cannot be neglected. Hence, the relationship between the fluorescence peaks and applied pressures exhibit quadratic behavior due to additional second order term. From the viewpoint of volume change under applied pressures, bulk modulus is not a constant and increases with increasing pressures. It implies that colloidal QDs are getting harder to be compressed in relative high pressure regime. Hence, the pressure coefficients are getting smaller.

One might argue that why we are able to observe relative high pressure regime compared to previous reports [4~6]. It may be ascribed to two reasons: First, the structures of the colloidal CdSe QDs with ZnS capped layer are more stable. Second, previous studies have shown that the transformation pressure of CdS nano-crystals can be increased by using de-ionized water instead of using the conventional methanol and ethanol solution [8] as the pressure medium. In the case of core/shell CdSe/ZnS QDs in water, fluorescence can be observed up to 6~7 GPa. This higher phase transformation pressure is possibly the main reason to exhibit the quadratic relationship.

For QDs under high pressures, the blue shift of PL is not only caused by the lattice contraction but also by the enhanced quantum confinement. For quantum confinement effect, the changes in electronic energy under applied pressure are given by $\Delta E = \frac{\hbar^2 \pi^2}{2\mu R^2} \left(\frac{1}{f} - 1 \right)$ [12], where f is the volume compressive ratio due to pressures and R is the radius of the QDs. By employing the typical parameters of CdSe QDs with 4 nm in radius and set f to be about 0.8, the change of the electron energy induced by the increasing of quantum confinement due to the applied pressure up to the phase transformation is still much small. This implies the blue shift of fluorescence

caused by the quantum confinement effect can be neglected.

Raman scattering measurement is a very sensitive and powerful tool to probe the lattice property of crystalline structures. To study the lattice quadratic behavior thoroughly, Raman spectra were also recorded at the same time. Figure 3 shows the Raman spectrum of colloidal CdSe/ZnS QDs under the pressure of 1.43 GPa at room temperatures. From left to right, three peaks can be observed, and are assigned as longitudinal optical (LO) phonon of CdSe core, LO phonon of ZnS shell, and 2-LO phonon of CdSe, respectively. Figure 4 shows pressure dependent Raman spectra of colloidal CdSe/ZnS QDs under various high pressures. With the increasing of pressure, all phonon peak shift to higher frequency up to 7 GPa. Above this pressure, these CdSe related Raman peaks disappear abruptly. Combining PL with Raman scattering, it is appropriate to conclude that the structures transformation occurs at this pressure. Figure 5 (a), (b) show the Raman peak shifts of the LO phonon and 2 LO phonon of CdSe QDs as a function of applied pressures. Both curves are all in quadratic behavior. The solid line is a quadratic fit by equation of $\omega(P) = \omega_0 + \alpha P + \beta P^2$

to all experimental data. The average pressure coefficient for Raman shift is $4.23 \text{ cm}^{-1}/\text{GPa}$, which is consistent with previous results of bare CdSe colloidal QDs [6]. This is a clear evidence for hydrostatic pressures applied to the colloidal QD core even over-coated with a ZnS thin layer. We can observe also that there are two pressure regimes with different slope divided at the pressure of 3 GPa. From the pressure dependent Raman spectra, the Gruneisen parameter can be derived by the equations of $\gamma = \frac{B_0}{\omega_0} \frac{d\omega}{dP}$, where B_0 is the bulk modulus equal to 53 GPa for CdSe bulk [13]. One then obtains $\gamma = 0.11$, and the LO phonon frequency at ambient pressure is 216 cm^{-1} , which is larger than the bulk value of

213 cm^{-1} . The increased value is due to additional compressive stress resulted from the over-coated ZnS [14]. Previous work has reported that QDs over-coated with ZnS are able to increase the Raman shift with a value of 2 cm^{-1} .

IV. CONCLUSION

We have studied the electronic and vibrational states of colloidal core/shell CdSe/ZnS QDs at room temperatures with high pressure optical measurements. Pressure dependent quadratic lattice behavior can be observed explicitly from the PL and Raman spectras up to ~ 7 GPa. This quadratic relationship is consistent with the theoretical prediction. The average pressure coefficients for PL and Raman measurements, as well as Gruneisen parameter are obtained to be 32 meV/GPa , 4.2 cm^{-1} and 0.11 , respectively.

ACKNOWLEDGEMENTS

This work was supported by MOE-ATU and the National Science Council under the grant numbers of NSC 94-2112-M-009 -024, NSC 95-2112-M-009 -047 and 94-2120-M-033-001.

REFERENCES

- [1] M. Jr Bruchez, M. Moronne, P. Gin, S. Weiss, and A. P. Alivisatos, *Science* **281**, 2013 (1998).
- [2] W. C. W. Chan and S. M. Nie, *Science* **281**, 2016 (1998).
- [3] X. Michalet, F. F. Pinaud, L. A. Bentolila, J. M. Tsay, S. Doose, J. J. Li, G. Sundaresan, A. M. Wu, S. S. and Gambhir, S. Weiss, *Science* **307**, 538 (2005).
- [4] W. Shan, W. Walukiewicz, J. W. Ager, K. M. Yu, and J. Wu, *Appl. Phys. Lett.* **84**, 67 (2003).
- [5] J. Li, G. H. Li, J. B. Xia, J. B. Zhang, Y. Lin and X. R. Xiao, *J. Phys. Condens. Matter* **13**, 2033 (2001).
- [6] A. P. Alivisatos, T. D. Harris, L. E. Brus, and A. Jayaraman, *J. Chem. Phys.* **89**, 5979 (1988).
- [7] S. H. Wei and A. Zunger, *Phys. Rev. B* **60**, 5404 (1999).

[8] X. S. Zhao, J. Schroeder, P.D. Persans and T. Bilodeau,
Phys. Rev. B **43**, 12580 (1991).

FIGURE CAPTIONS

[9] M. A. Hines and P. G. Sionnest, J. Phys. Chem. **100**, 468, (1996).
Figure 1: Pressure dependent fluorescence spectra of colloidal CdSe/ZnS QDs at room temperature.

[10] A. L. Edwards and H. G. Drickamer, Phys. Rev. **122**, 1149 (1961).
Figure 2: Fluorescence peak energy as a function of applied pressures.

[11] S. H. Tolbert, A. B. Herhold, C. S. Johnson, and A. P. Alivisatos, Phys. Rev. Lett. **76**, 4384 (1996).
Figure 3: Raman spectrum of colloidal CdSe/ZnS QDs at 1.43 GPa at room temperature.

[12] M. R. Silvestri and J. Schroeder, J. Phys. Condens. Matter **7**, 8519 (1995).
Figure 4: Pressure dependent Raman spectra of colloidal CdSe/ZnS QDs at room temperature.

[13] S. H. Wei, and A. Zunger, Phys. Rev. B **60**, 5404 (1999).
Figure 5: Raman peak shifts of (a) LO and (b) 2 LO phonon

[14] R. W. Meulenberg, Phys. Rev. B **70**, 235311 (2004).
as a function of applied pressure.

Figure 1

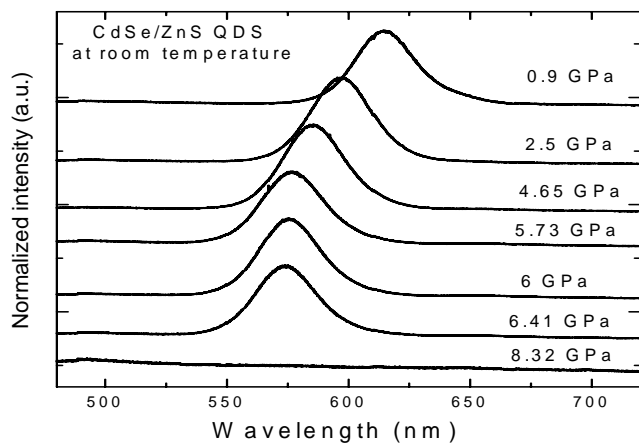


Figure 2

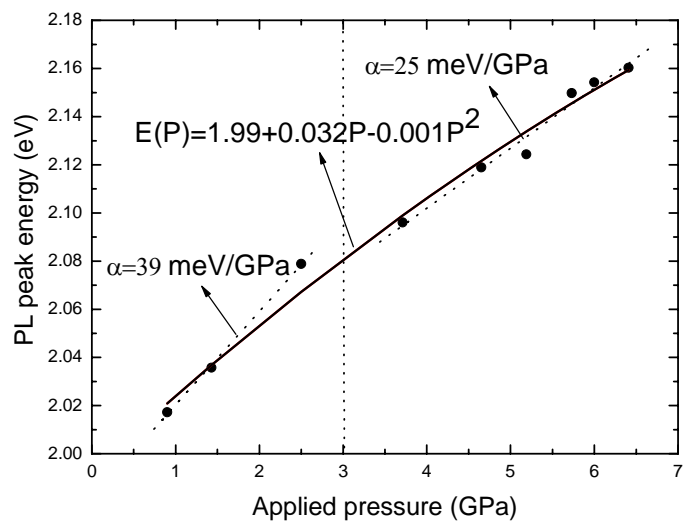


Figure 3

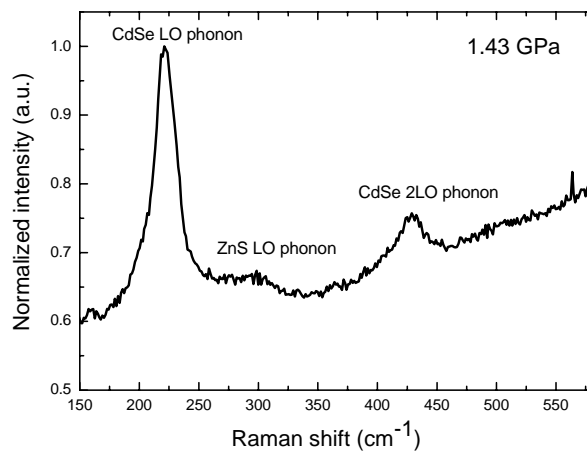


Figure 4

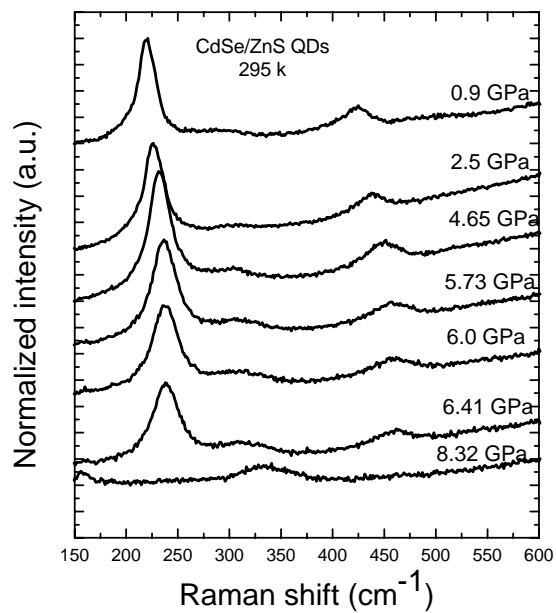
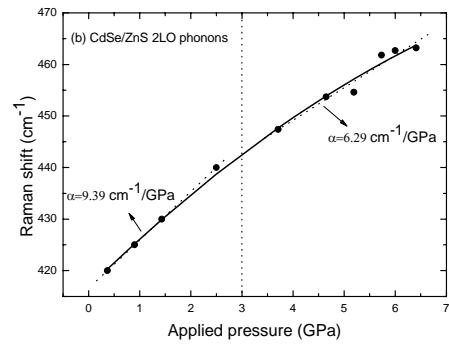
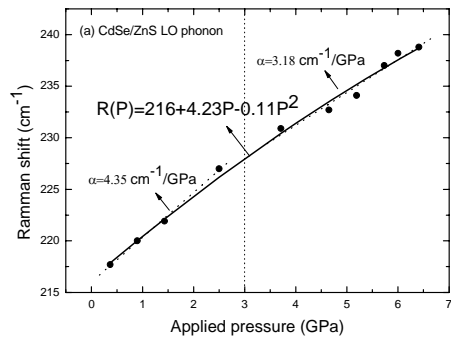


Figure 5 (a)(b)



Studies on fluorescence enhancement for CdSe quantum dots with surface modifications by means of single molecule detection technique

C. T. Yuan¹, R.W.Chou¹, Y. N. Chen^{1,2}, W. C. Chou¹ and D. S. Chuu¹

¹Department of Electrophysics, National Chiao Tung University, HsinChu 30010, Taiwan

²National Center for Theoretical Sciences, National Cheng Kung University, Tainan 701, Taiwan

ABSTRACT

Fluorescence enhancement for colloidal CdSe quantum dots (QDs) modified by capped layers has been studied by means of single molecule detection technique. It is found that modification of the ZnS capped layer does not increase the on-time fraction but can enhance the quantum yields (QYs) of on-time duration. With the attachment of additional hexanediamine (HDA) surface ligands, both on-time fraction and QYs can be enhanced up to 2 and 13 fold for colloidal CdSe/ZnS QDs. In this case, the fluorescence decay profile exhibits close to single exponential behavior with longer lifetimes.

1 Electronic address: dschuu@nctu.edu.tw

Manuscript submitted for publishing

INTRODUCTION

From the macroscopic point of view, ensemble colloidal CdSe quantum dots (QDs) are attractive fluorophores for potential applications in biological labels due to excellent fluorescence properties, such as brightness, higher photo-stability, and tunable emission spectra [1,2]. Consequently, single colloidal QDs are expected to be one of the suitable candidates for single molecular probes [3]. However, ensemble measurements merely reflect the average properties of an inhomogeneous sample. Deep studies of fluorescence properties at single QD level are necessary. With the development of single-molecule detection technique, some interesting phenomena, which are missing in the ensemble-averaged experiments, of single QDs have been discovered, such as fluorescence intermittency (blinking) and lifetime fluctuation [4,5]. This blinking behavior (fluorescence switches between on and off states under continuous excitation) is a fatal problem for practical applications. It causes fluorescence to become complex and not directly correlated with ensemble measurements. For example, QYs are not consistent between ensemble and individual QDs. In Ref [6], they proposed QY of individual QD is the same for all bright QDs, and ensemble QYs can be determined by the ratio of bright QDs to total ones. The surfaces of colloidal QDs play an important role in determining fluorescence properties due to large surface to volume ratio. It has been demonstrated that CdSe fluorescence properties are sensitive to surface of QDs, even overcoated with a thick ZnS shell [7,8]. Attaching organic or inorganic capped layers is a popular method to enhance the ensemble fluorescence [9,10]. However, the mechanism is not explicit known, especially, from single QD viewpoint, how much of the enhancement is due to the increasing of on-time duration and how much is due to enhancement of QYs within the on-time or both. Therefore, studies on fluorescence enhancement from single QD viewpoint can facilitate to directly understand and improve the fluorescence properties of colloidal QDs.

In this work, fluorescence enhancement for colloidal CdSe QDs modified by organic and inorganic capped layer are studied by means of single molecule detection technique. It is found that the conventional ZnS capped layer does not increase the on-time fraction, however, it can enhance QYs of on-time duration. Attaching additional HDA surface ligands, both on-time fraction and QYs can be enhanced up to 2 and 13 fold for colloidal CdSe/ZnS QDs. In this case, the fluorescence decay profiles exhibit close to single exponential behavior with longer lifetimes.

EXPERIMENTAL DETAILS

For single-isolated QD measurements, dilute colloidal solution of nano-molar concentration was dispersed onto a clean cover slide by spin coating.[11] In this case, the mean separation between two individual QDs is larger than 1 micron and can be detected by far field optical microscopy. Fluorescence measurements were performed based on a laser scanning confocal microscope equipped with a piezo-scanner with nanometer spatial resolution. The excitation pulses at the wavelength of 405 nm, 10 MHz repetition rate were focused to a nearly diffraction limited spot by an oil-immersion objective with 1.4 N.A. Fluorescence was collected by the same objective and guided to a single photon avalanche photon diodes after passing a 50 micron confocal pinhole. Then, fluorescence and relative synchronized laser reference fed into very fast electronics system (Time harp 200, PicoQuant) to process time-correlated analysis.

Time-tagged, time-resolved (TTTR) measurements by using Timeharp 200 (Picoquant GmbH) are performed on each single QD. TTTR measurements are distinct from conventional time-correlated single photon counting techniques. For TTTR acquisition modes, both start-stop time (time between laser pulses and single photon emission) and absolute arrival time (from the experimental start to single photon emission) can be recorded simultaneously [12]. The fluorescence decay profiles can be constructed by histogramming start-stop time for many cycles by time-resolved modes. The transient fluorescence trace can be formed by integrating all photons in a given bin time (1 milliseconds) by time-tagged modes. From this time trace, we can construct on-off time and burst sizes histogram to statistical analysis.

As for the ensemble fluorescence measurements, the concentrated solution sample was directly excited by a tungsten lamp filtered by a monochromator. Fluorescence was dispersed by a spectrometer and guided to a photo-multiplied tube.

RESULTS AND DISCUSSIONS

Figure 1 shows the ensemble fluorescence spectra for colloidal CdSe QDs with original TOPO ligands, high band gap materials (ZnS), and ZnS/HDA surface from the same batch. The red shift of the peak position can be observed for both ZnS and ZnS/HDA coated QDs due to exciton wavefunction extended into ZnS layers [13]. Upon attaching additional surface layers, ensemble fluorescence can be increased. The enhanced factors are 3.13, and 8.3

for ZnS, and ZnS/HDA mixture capped QDs. This ensemble enhancement by introducing capped layer is generally assigned to passivate surface states of QDs [10,14].

To clarify the fluorescence enhancement, we utilized single molecule detection technique to monitor the fluorescence properties of single-isolated QDs from the same batch. Figure 2 shows a $3 \times 3 \mu\text{m}^2$ fluorescence image for colloidal CdSe/ZnS QDs obtained by laser scanning confocal microscope. Some streaky patterns with diffraction limited spots of ~ 300 nm can be observed and are attributed to fluorescence intermittency [4]. This is a criterion to identify the single-isolated colloidal QDs. In order to monitor individual QDs, the laser spot can be moved to specific QD position to record transient fluorescence. Figure 3 displays the fluorescence time traces with time window of 10 seconds for original TOPO (a), ZnS (b), and ZnS/HDA (c) capped QDs. For single QDs measurements, to avoid dots to dots heterogeneity, more than 10 individual QDs for the same species can be measured and the bin time for taking every data is 1 millisecond. From fluorescence time traces, blinking phenomena can be observed clearly, especially for ZnS and ZnS/HDA mixture capped QD. This is a hallmark and evidence of the detection of a single-isolated QD [4]. The reasons for the dark periods are usually attributed to the formation of the charged QDs due to Auger ionization [15]. When a charged QD absorbs a photon and generates an exciton, it becomes a three particles system. In this case, the energy transfer from exciton to third particle is faster (\sim ps) than radiative recombination process (\sim ns) [16]. For this duration, the QD does not fluoresce, even absorbs the excitation photons. Only after the neutralization of the charged QD, it starts to emit photon. To obtain quantitative and meaningful parameters, the general approach is to define an intensity threshold from time trace to distinguish between on and off states.[17] Then, we can define on (off) duration time, which all photons are above (below) the threshold, and construct an on (off) time distribution histogram from overall experimental data.

For single QD measurements, the fluorescence enhancement factors are 2.76, and 6.8 for ZnS and ZnS/HDA mixture capped QDs compared with bare QDs by summing up the total number of emitted photons above the predefined threshold. The values are near to the results of ensemble measurements. It indicated that ensemble fluorescence enhancement by introducing surface modification is mainly due to the increasing fluorescence of individual QDs instead of total numbers of bright ones. Figure 4 shows a histogram of on-time duration plotted by log-log scale for TOPO (a), ZnS (b), ZnS/HDA (c) capped QDs. The distribution of on-time duration

exhibits a universal power-law behavior [18]. The mean on-time duration calculated by averaging arithmetically are 1.69, 3.81, and 8.37 ms, respectively. We discovered that the mean on-time duration can be increased 2.3, 5 fold for ZnS and ZnS/HDA coated QDs. However, the corresponding off-time also increased (not shown). This result can be explained by the ionization blinking model [15]. ZnS capped layer can block electron ejected (returned) between QDs and surrounding matrix. Hence, the enhanced on-time accompanied with the increasing of the off-time by introducing the ZnS high band gap materials. For comparison, the ratio of the on-time to total on-off time needs to be deduced. The on-time fractions are 0.16 and 0.15 for bare and ZnS capped QDs. It implies that the on-time fraction can not be increased by ZnS capped layer. Therefore, the fluorescence enhancement of individual QDs with ZnS layer is not originated from increasing on-time fraction. Interestingly, the on-time fraction can be enhanced up to 2.1 fold by adding HDA surface ligands.

To study this enhancement explicitly, we need to concern not only the on-time fraction, but also the emitted photon number within the on-time duration. From fluorescence time traces of Figure 1, the intensity fluctuated within on-time for individual QDs and varied with QDs capped by different surface modifications. Figure 5 shows the histogram of the burst sizes for TOPO (a), ZnS (b), and ZnS/HDA (c) coated QDs. The burst sizes are defined as the total photon number above the threshold for a given on-time duration. From burst sizes histogram, we can obtain total emitted photon number from a specific QD by integrating column area and get mean burst sizes by arithmetic average. It can tell us how many emitted photons within mean on-time duration. The mean burst sizes are 5.6, 38.6, and 523.5 counts, respectively. It indicates that ZnS capped layer can enhance the burst sizes (fluorescence intensity) within on-time duration instead of increasing on-time fraction. However, for ZnS/HDA capped QDs, both QYs and burst sizes can be increased. As mentioned before, this enhancement is usually assigned to passivate trap states by introducing surface modification from ensemble measurements.

To confirm the above statements, we also performed the time-resolved fluorescence measurements to monitor the photoexcited carrier dynamics of single QDs at the same time. Figure 6 shows the fluorescence decay curves for bare TOPO (a), ZnS (b), ZnS/HDA (c) capped QDs. The decay lifetime is correlated to the fluorescence intensity, for which strong intensity possesses longer lifetime. The decay curve, which is more close to single exponential behavior with longest lifetime, can be

observed for ZnS/HAD capped QDs. The measured decay rates are the summation of radiative and nonradiative decay rates. In general, radiative processes are not sensitive to surface modification and only nonradiative decay can be modified. In this case, nonradiative processes can be suppressed due to passivate trap states by introducing surface modification and increase the observed lifetime. Here, we used the stretched exponential function

$$I(t) = I_0 \exp\left(-\left(\frac{t}{\tau}\right)^\beta\right)$$

to fit our experimental data. Where τ is fluorescence lifetime of single QDs, $0 < \beta \leq 1$, representing the distribution of decay rates. For $\beta = 1$, fluorescence decay curve exhibits perfect single exponential decay behavior [19], which means radiative processes dominate. For ZnS/HDA capped QDs, it possesses the longest lifetime and largest β due to a better degree of passivation compared with bare and only ZnS capped QDs. It implies that the QYs for individual QDs can be actually enhanced by introducing surface modification. From statistical analysis of the experimental data, we suggest that the main function of ZnS capped layer can block electron to reject and return from QDs into surrounding matrix. Both on-time and off-time are increased but the total on-time fraction are the same for ZnS coated QDs compared with bare QDs. The enhancement of fluorescence intensity of single QDs with ZnS capped layer is originated from the increasing burst sizes of on-time due to passivate the surface states of single QDs. Additional HDA surface molecule not only increases the on-time fraction but also increases the burst sizes.

CONCLUSION

Fluorescence enhancement for colloidal CdSe QDs modified by capped layer has been studied by means of single molecule detection technique. Conventional ZnS capped layer does not increase the on-time fraction but can enhance QYs within on-time duration. Attaching additional HDA surface ligands, both on-time fraction and QYs can be enhanced up to 2 and 13 fold for colloidal CdSe/ZnS QDs. In this case, the fluorescence decay profiles are close to single exponential behavior with longer lifetimes.

REFERENCES

- [1] M. J. Bruchez, M. Moronne, P. Gin, S. Weiss, and A. P. Alivisatos, *Science* **281**, 2013 (1998).
- [2] W. C. W. Chan and S. M. Nie, *Science* **281**, 2016 (1998).
- [3] C. Y. Zhang, H. C. Yeh, M. T. Kuroki, and T. H. Wang, *Nature*, **4**, 826 (2005).
- [4] M. Nirmal, B. O. Dabbousi, M. G. Bawendi, J. J. Macklin, J. K. Trautman, T. D. Harris, L. E. Brus, *Nature*, **383**, 802 (1996).
- [5] G. Schlegel, J. Bohnenberger, I. Potapova, and A. Mews, *Phys. Rev. Lett.* **88**, 137401 (2002).
- [6] J. Yao, D. R. Larson, H. D. Vishwasrao, W. R. Zipfel, and W. W. Webb, *PNAS*, **102**, 14284 (2005).
- [7] G. Kalyuzhny and R. W. Murray, *J. Phys. Chem. B*, **109**, 7012 (2005).
- [8] F. Koberling, A. Mews, and T. Basché, *Adv. Mater.*, **13**, 672 (2001).
- [9] D. V. Talapin, A. L. Rogach, A. Kornowski, M. Haase, and H. Weller, *Nano Lett.*, **1**, 207 (2001).
- [10] M. A. Hines, and P. J. Guyot-Sionnest, *J. Phys. Chem.*, **100**, 468 (1996).
- [11] S. A. Empedocles, R. Neuhauser, K. Shimizu, and M. G. Bawendi, *Adv. Mater.* **11**, 1243 (1999).
- [12] A. Benda, M. Hof, M. Wahl, M. Patting, R. Erdmann, and P. Kapusta, *Review of Scientific Instruments*, **76**, 033106 (2005).
- [13] B. O. Dabbousi, J. R. Viejo, F. V. Mikulec, J. R. Heine, H. Mattoussi, R. Ober, K. F. Jensen, and M. G. Bawendi, *J. Phys. Chem. B*, **101**, 9463 (1997).
- [14] S. N. Sharma, Z. S. Pillai, and P.V.Kamat, *J. Phys. Chem. B*, **107**, 10088 (2003).
- [15] A. L. Efros, and M. Rosen, *Phys. Rev. Lett.* **78**, 1110 (1996).
- [16] V. I. Klimov, A. A. Mikhailovsky, D. W. McBranch, C. A. Leatherdale, M. G. Bawendi, *Science*, **287**, 1011 (2000).
- [17] M. Kuno, D. P. Fromm, H. F. Hamann, A. Gallagher, and D. J. Nesbitt, *J. Chem. Phys.* **115**, 1028 (2001).
- [18] M. Kuno, D. P. Fromm, H. F. Hamann, A. Gallagher, and D. J. Nesbitt, *Journal of Chemical Physics*, **112**, 3117 (2000).
- [19] G. Schlegel, J. Bohnenberger, I. Potapova, and A. Mews, *Phys. Rev. Lett.* **88**, 137401 (2002).

Figure 1 The ensemble fluorescence spectra for colloidal CdSe QDs with original TOPO ligands, high band gap materials (ZnS), and ZnS/HDA surface from the same batch.

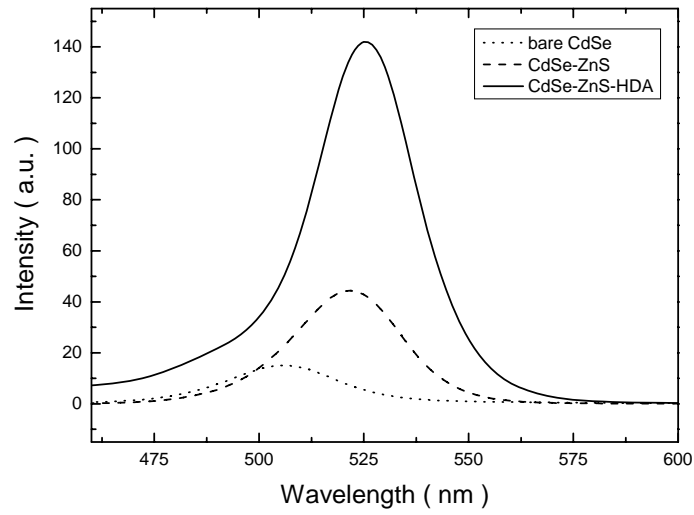


Figure 2 A $3 \times 3 \mu m^2$ fluorescence image for colloidal CdSe/ZnS QDs obtained by laser scanning confocal microscope.

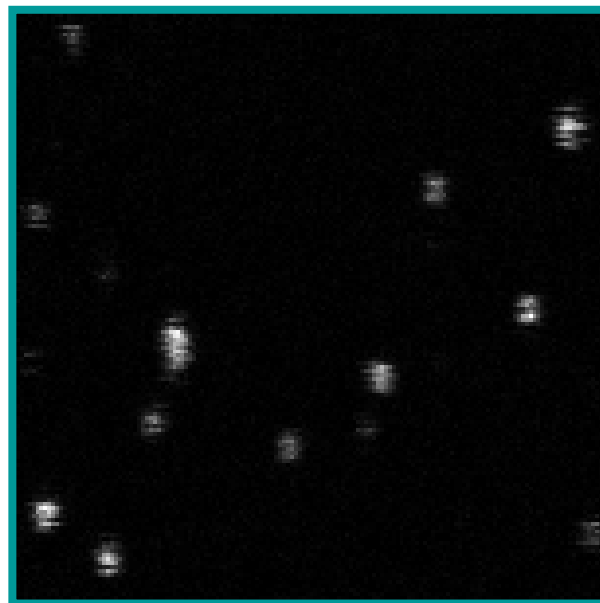


Figure 3. (a) The fluorescence time traces with time window of 10 seconds for original TOPO capped QDs.

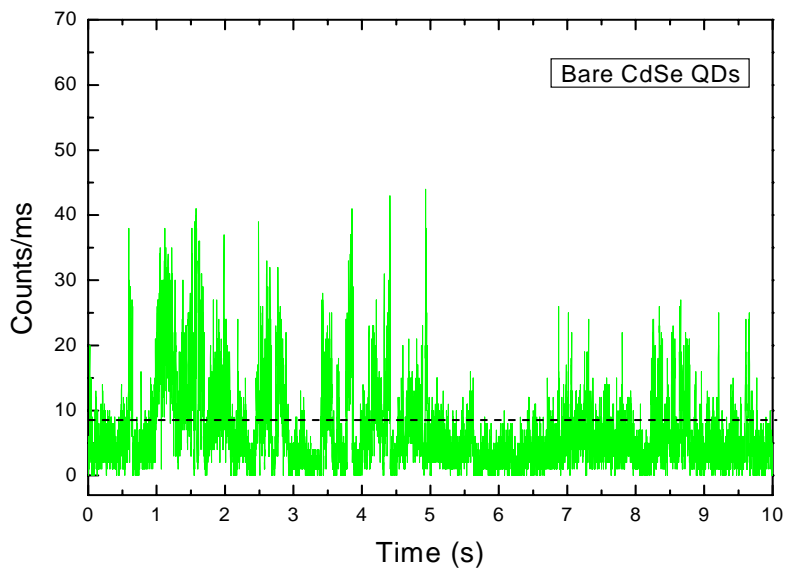


Figure 3. (b) The fluorescence time traces with time window of 10 seconds for ZnS capped QDs..

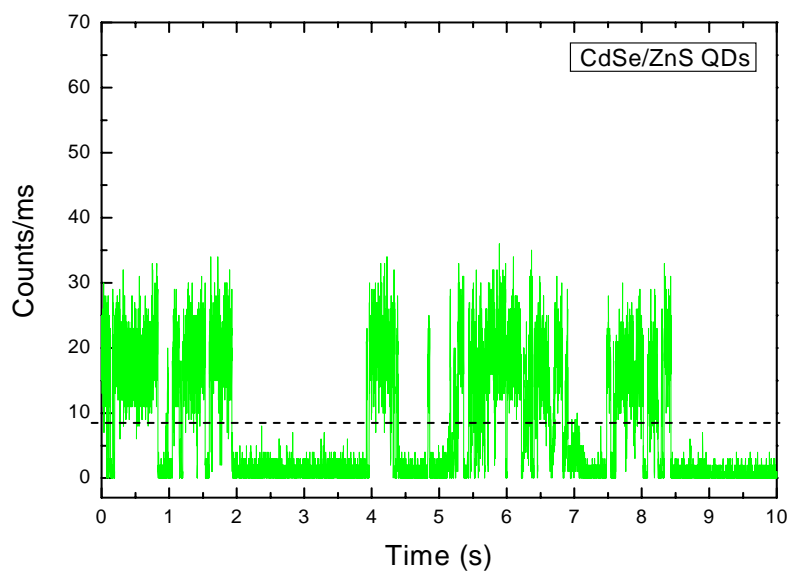


Figure 3. (C) The fluorescence time traces with time window of 10 seconds for ZnS/HDA capped QDs.

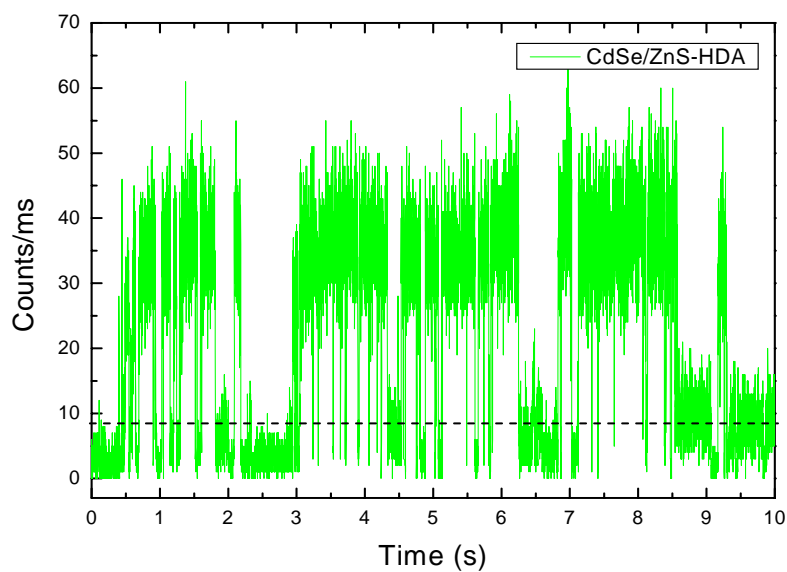
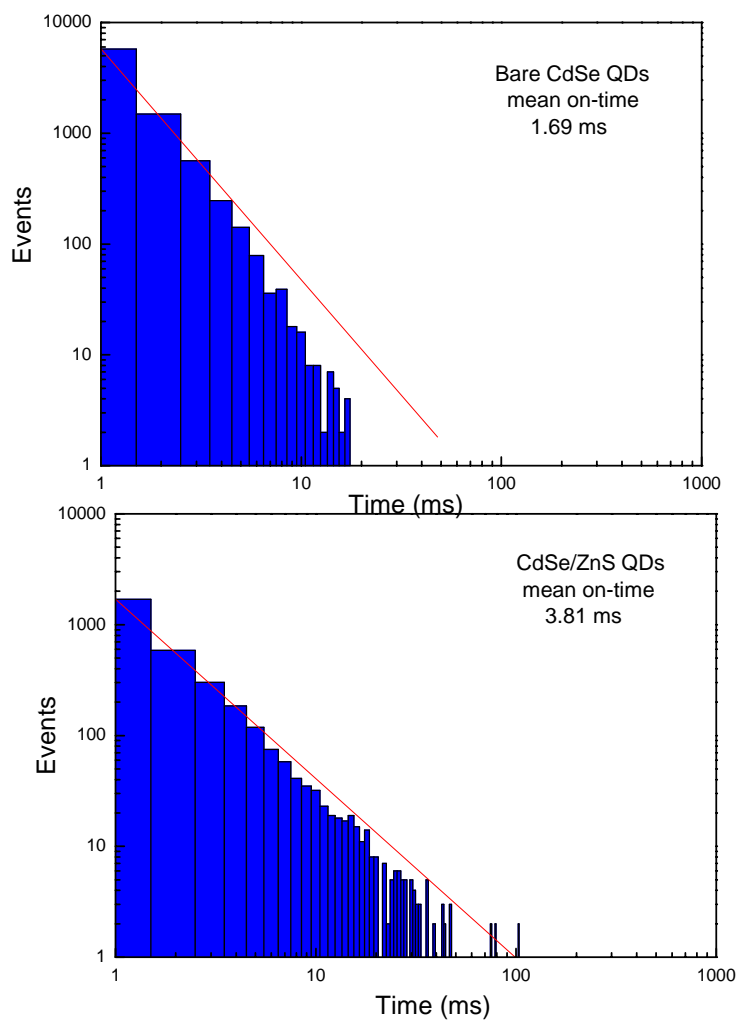


Figure 4. (a), (b), (c). A histogram of on-time duration plotted by log-log scale for TOPO (a), ZnS (b), ZnS/HDA (c) capped QDs.



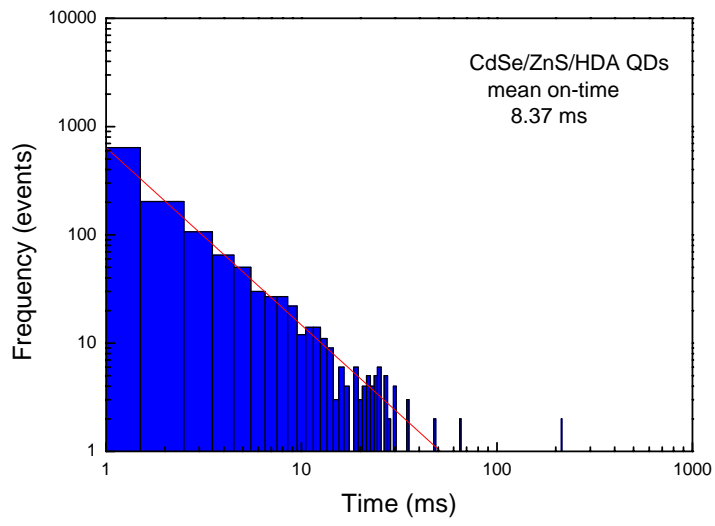


Figure 5. (a), (b), (c). The histogram of the burst sizes for TOPO (a), ZnS (b), and ZnS/HDA (c) coated QDs.

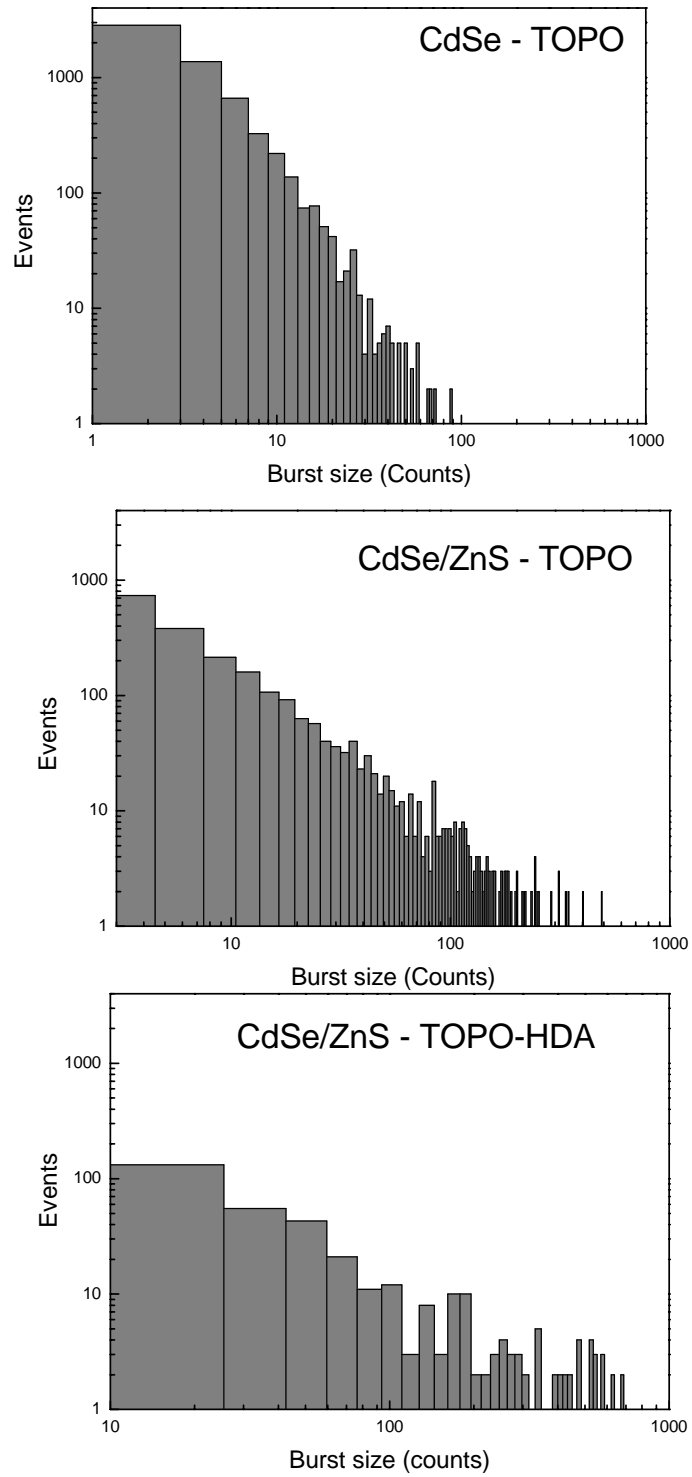
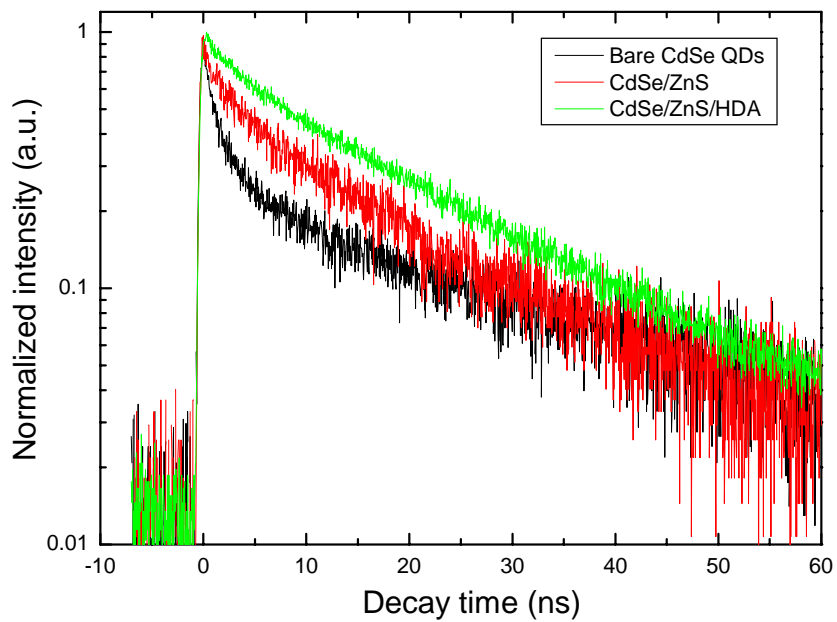


Figure 6. The fluorescence decay curves for bare TOPO (a), ZnS (b), ZnS/HDA (c) capped QDs.



可供推廣之研發成果資料表

 可申請專利 可技術移轉

日期：__年__月__日

國科會補助計畫	計畫名稱： 計畫主持人： 計畫編號： 學門領域：
技術/創作名稱	
發明人/創作人	
技術說明	中文： (100~500 字)
	英文：
可利用之產業 及 可開發之產品	
技術特點	
推廣及運用的價值	

※ 1. 每項研發成果請填寫一式二份，一份隨成果報告送繳本會，一份送 貴單位研發成果推廣單位（如技術移轉中心）。

- ※ 2. 本項研發成果若尚未申請專利，請勿揭露可申請專利之主要內容。
- ※ 3. 本表若不敷使用，請自行影印使用。